Multilayer Active Shell Mirrors

Thesis by

John Steeves

In Partial Fulfillment of the Requirements

for the Degree of

Doctor of Philosophy

California Institute of Technology

Pasadena, California

2015

(Defended May 8, 2015)

Acknowledgements

First and foremost I would like to thank my advisor, Professor Sergio Pellegrino, for providing me with the opportunity to work in this exciting field of research. Your willingness to spend time with students, encouragement to keep pushing forward when challenges arise, and excitement for all things mechanics is unparalleled. My time as a graduate student has been extremely enjoyable and I attribute it to this wonderful environment that you provide. I would also like to thank Professor Guruswami Ravichandran, Professor Dennis Kochmann, and Professor Joel Burdick for their time and willingness to serve on my committee.

I would like to acknowledge the many current and former members of the Space Structures Laboratory who have been wonderful research partners throughout the past 4 years. I especially want to thank Dr. Keith Patterson who provided invaluable mentorship, particularly in the early years, as well as Dr. Marie Laslandes who was patient enough to introduce me to optics. It has been a pleasure working with you both. I would also like to thank my office mate, Dr. Xin Ning, for many in-depth and often late night discussions on mechanics which seemed to increase in frequency during the days leading up to my defense.

I have had the pleasure of collaborating with many people throughout my graduate career. A special acknowledgment is required for Dr. David Redding, Dr. Samuel Case Bradford, James Kent Wallace, Dr. Scott Basinger, and Dr. Troy Barbee for the direct collaboration on this project. I have enjoyed our interactions immensely and look forward to working with you all further. I would also like to thank Dr. Andrew Shapiro, Dr. Harish Manohara, Dr. Risaku Toda, Dr. Greg Davis, John Baker, and Mark Thomson for the continual support of our research efforts.

I thank the staff at GALCIT, specifically Petros Arakelian, Joe Haggerty, Kathleen Jackson, Dimity Nelson and Christine Ramirez. I would especially like to thank Petros Arakelian for the many hours spent troubleshooting in lab.

I would like to acknowledge the Natural Sciences and Engineering Research Council of Canada (NSERC), NASA JPL, and the Keck Institute for Space Studies (KISS) at Caltech for funding our research. I would especially like to thank Michelle Judd from KISS who provides unparalleled student support at Caltech.

Finally, I would like to thank my family and friends from all over the world who have provided the "sideline support" often required when research becomes tedious. I want to especially thank my parents for their support and encouragement in all aspects of my life.

Abstract

This thesis presents a novel active mirror technology based on carbon fiber composites and replication manufacturing processes. Multiple additional layers are implemented into the structure in order to provide the reflective layer, actuation capabilities and electrode routing. The mirror is thin (< 1.0 mm), lightweight (2.7 kg/m^2) and has large actuation capabilities. These features, along with the associated manufacturing processes, represent a significant change in design compared to traditional optics. Structural redundancy in the form of added material or support structures is replaced by thin, unsupported lightweight substrates with large actuation capabilities.

Several studies motivated by the desire to improve as-manufactured figure quality are performed. Firstly, imperfections in thin CFRP laminates and their effect on post-cure shape errors are studied. Numerical models are developed and compared to experimental measurements on flat laminates. Techniques to mitigate figure errors for thicker laminates are also identified. A method of properly integrating the reflective facesheet onto the front surface of the CFRP substrate is also presented. Finally, the effect of bonding multiple initially flat active plates to the backside of a curved CFRP substrate is studied. Figure deformations along with local surface defects are predicted and characterized experimentally. By understanding the mechanics behind these processes, significant improvements to the overall figure quality have been made.

Studies related to the actuation response of the mirror are also performed. The active properties of two materials are characterized and compared. Optimal active layer thicknesses for thin surface-parallel schemes are determined. Finite element simulations are used to make predictions on shape correction capabilities, demonstrating high correctabiliity and stroke over low-order modes. The effect of actuator saturation is studied and shown to significantly degrade shape correction performance.

The initial figure as well as actuation capabilities of a fully-integrated active mirror prototype are characterized experimentally using a Projected Hartmann test. A description of the test apparatus is presented along with two verification measurements. The apparatus is shown to accurately capture both high-amplitude low spatial-frequency figure errors as well as those at lower amplitudes but higher spatial frequencies. A closed-loop figure correction is performed, reducing figure errors by 94% from 8.12 μm to 0.52 μm RMS.

Contents

List of Figures

List of Tables

Chapter 1

Introduction

1.1 Background and Motivation

Increasingly demanding science goals from the astrophysics, astronomy, and earth sciences communities necessitate the development of large aperture telescopes. Two possible concepts for the next-generation space-based observatories are presented in Figure 1.1. The first, shown in Figure 1.1(a), is from the Advanced Technology Large Aperture Space Telescope (ATLAST) study [1]. The ATLAST concept is a monolithic telescope constructed on Earth and placed in orbit using a single launch vehicle. The envisioned 16.5 m dia. primary mirror represents a near upper-bound on achievable aperture sizes for telescopes of this design due to volume and mass constraints set by the launch vehicle. In contrast, the concept shown in Figure 1.1(b) stemming from the Large Aperture Study at the Keck Institute for Space Studies (KISS) at Caltech implements on-orbit self-assembly techniques. Multiple launches can be used to synthesize the entire telescope and therefore limitations imposed by the launch vehicle are no longer of concern.

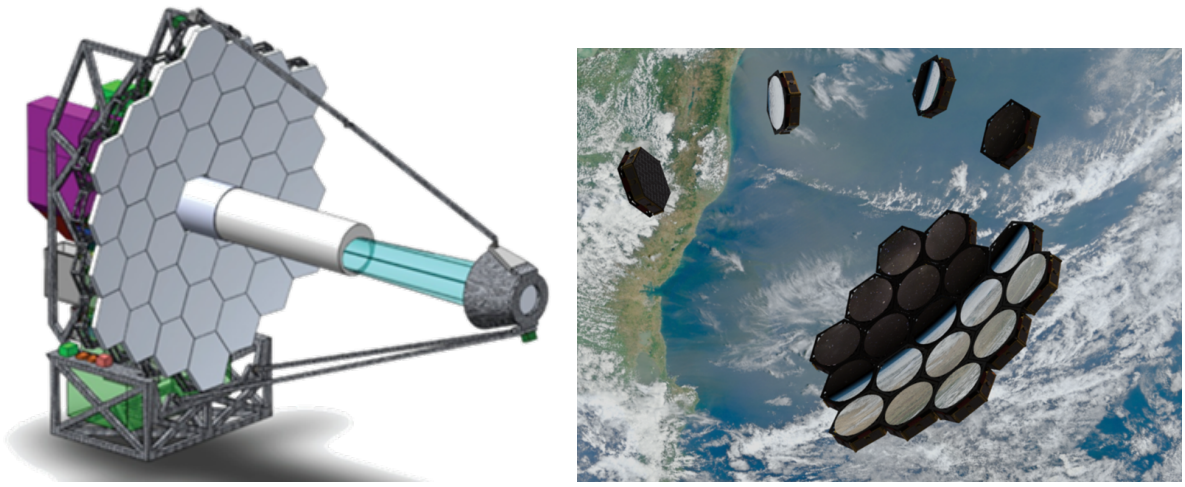

(a) (b)

Figure 1.1: a) Advanced Technology Large Aperture Space Telescope (ATLAST) concept. b) Autonomous Assembly of a Reconfigurable Space Telescope (AAReST) concept.

Both of these concepts envision segmentation of the primary aperture. This scheme is currently under implementation with the James Webb Space Telescope (JWST), using 18 hexagonal segments to construct the 6.5 m dia. primary aperture. However, with segmentation and aspheric primaries, identical segments cannot be used as varying prescriptions are required depending on the radial position of each segment with respect to the optical axis. For JWST 3 unique segments are required. However, this number grows rapidly as the diameter of the primary aperture increases. This is currently a problem experienced by large ground-based telescopes such as the Thirty Meter Telescope (TMT) where a 30 m dia. primary mirror is composed of 492 total segments with 82 unique prescriptions. Therefore, a substantial manufacturing effort is required in order to construct such an aperture.

Existing mirror technologies are insufficient in order to realize concepts such as these. Traditional methods of grinding and polishing a slab of low-CTE glass result in costly, complex, and timely efforts. Furthermore, the areal density of such mirrors is prohibitively high. For example, the primary mirror of the Hubble Space Telescope (HST) has an areal density of $\sim$ 183 kg/m^2 at a 2.4 m diameter [2]. Advancements in lightweight materials have lowered this number substantially to $\sim$ 20 kg/m^2 for JSWT implementing Beryllium mirrors [3]. However, the cost and manufacturing complexity remain as the mirrors must still be polished down to optical-quality tolerances.

Incorporation of active elements into the mirror structure allows manufacturing tolerances to be relaxed as subsequent figure correction procedures can be performed. This scheme not only allows for the correction of initial manufacturing errors but in-situ changes to the mirror figure can be made. Therefore, deformations due to thermal variations and material creep can be accommodated. Furthermore, with large actuation strokes bulk changes to the optical prescription of each segment can be realized, potentially enabling 1) identical segments to be used in a large aperture telescope and/or 2) reconfiguration of the aperture geometry in order to change the resolution of the telescope as whole [4, 5].

1.1.1 Replicated Mirror Technologies

A method of producing lightweight mirrors while reducing manufacturing complexity is to implement replication techniques. In this process a convex mandrel is used to define the optical figure. The material to be used for mirror construction is then placed upon the surface of this mandrel and a curing process is initiated, often under the application of high temperature and pressure. Upon cure and removal from the mandrel, a concave mirror is produced. Multiple mirror segments can be made from a single mandrel, resulting in a high through-put manufacturing process.

A significant amount of work has been performed in an attempt to produce replicated optics [8, 9, 10, 7, 11]. Carbon fiber reinforced polymers (CFRPs) are ideal candidate materials for replication as they can be formed in their pre-preg state. They also exhibit tailorable mechanical and thermal properties depending on the chosen fibers and defined laminate orientation. However, efforts to create CFRP-based mirrors often suffer from a lack of surface accuracy as the thermal stresses developed during cure tend to cause distortions. Stiff

(a) (b)

Figure 1.2: a) 1.0 m dia. parabolic composite mirror from Composite Mirror Applications [6]. b) 150 mm. dia. CFRP mirror with a reflective nanolaminate facesheet [7].

backing structures are often incorporated into the mirror design in order to reduce these errors. Figure 1.2(a) is a picture of a 1.0 m dia. parabolic CFRP mirror from Composite Mirror Applications[6] produced using replication techniques with a carbon foam support on its back surface.

Obtaining a high-quality front surface is also a challenge in the fabrication of CFRP-based optics due to print-through of the carbon fibers onto the front imaging surface [12, 13]. A method to mitigate these effects is the incorporation of a high-quality metal foil known as a nanolaminate. By bonding the nanolaminate to the front surface of the mirror a significant improvement in surface quality can be obtained. Figure 1.2(b) is a picture of a 150 mm dia. flat CFRP mirror implementing a nanolaminate facesheet showing a high-quality imaging surface [7].

1.1.2 Active Mirror Technologies

Active mirrors can be classified broadly into two categories according to their actuation mechanisms: 1) surface-normal and 2) surface-parallel. In the surface-normal actuation scheme actuators, often in the form of rods or columns, "push" or "pull" the surface of the mirror in the normal direction. In doing so local hills or valleys are created at the location of each actuator. Multiple actuators can be arranged in a continuous fashion, allowing for deformations to be imposed across the entire mirror surface. In contrast, mirrors implementing surface-parallel actuation schemes have actuators bonded to the surface of the mirror. Upon actuation, local out-of-plane deformations are produced through bending. This method lends itself well to the actuation of large mirrors as a reduced amount of active material is required.

Arguably the most advanced active mirror implementing surface-parallel actuation schemes is the Actuated Hybrid Mirror (AHM), depicted in Figure 1.3 and developed under a joint effort between NASA's Jet Propulsion Laboratory (JPL), Lawrence Livermore National Laboratories (LLNL), and AOA Xinetics Inc. The AHMs integrate a lightweight silicon carbide (SiC) structure with a nanolaminate facesheet. Stack ac-

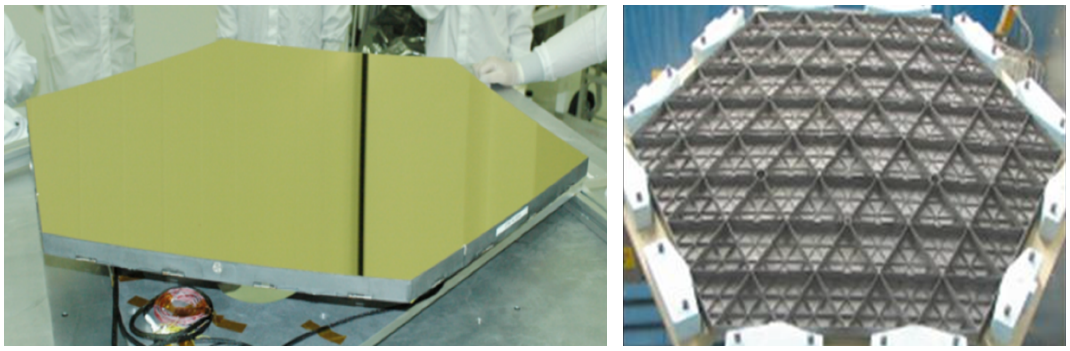

(a) (b)

Figure 1.3: Front and back surfaces of the Actuated Hybrid Mirror (AHM) [14].

tuators are embedded into the ribs of the mirror providing high actuation authority across the entire mirror structure. The SiC substrate is produced using quasi-replication techniques where the initial figure of the mirror is produced through replication but subsequent polishing steps are required. The AHMs have been demonstrated at an areal density of 10 - 15 kg/m^2, 20 nm RMS post-corrected figure accuracy and at scales $>$ 1.0 m in diameter [14, 15].

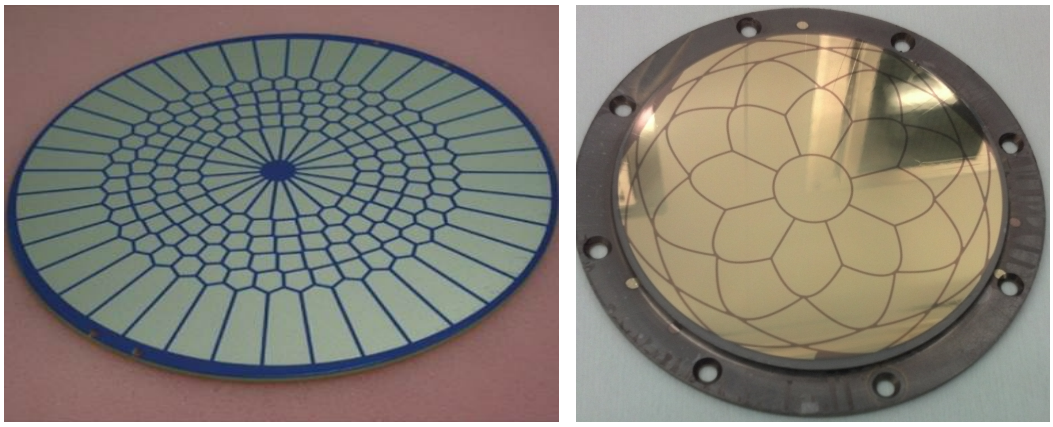

(a) (b)

Figure 1.4: Backside of thin 100 mm dia. mirrors from a) Cilas [16]. and b) Patterson, K. [17].

Extremely lightweight surface-parallel designs have also been developed based on thin glass substrates. Figure 1.4 displays the backside of two similar designs, one from Cilas Inc. [16] implemented on the adaptive-optics system for the Subaru Telescope and one developed at Caltech [17] for the Autonomous Assembly of a Reconfigurable Space Telescope (AAReST) technology demonstration mission [18, 19]. Both of these mirror designs have demonstrated large actuation capabilities ($\pm$ 40 μm bulk curvature change) due to their low thickness.

1.2 Active Mirror Concept

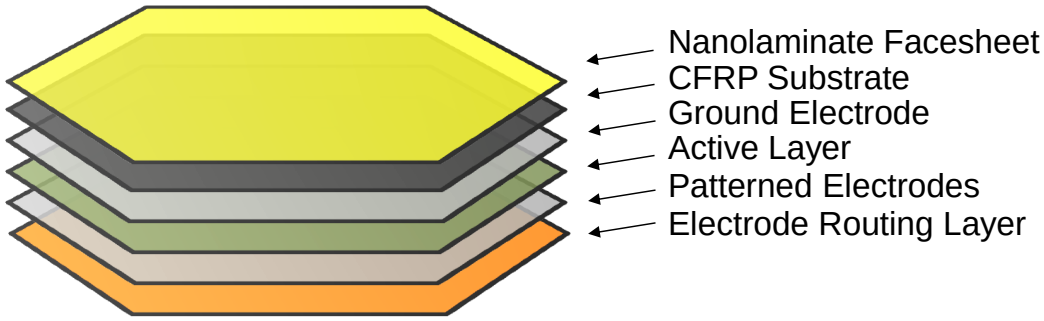

Figure 1.5: Exploded view of active mirror concept.

An overview of the multilayer active mirror concept proposed for this study is presented in Figure 1.5. The concept utilizes a CFRP substrate in order to provide the overall shape and structure of the mirror. A reflective nanolaminate facesheet is integrated onto the front of the substrate providing the high-quality surface required for imaging. A layer of active material with a ground plane and patterned electrodes is incorporated onto the backside of the substrate providing the surface-parallel actuation capabilities. Finally, a flexible electrode routing layer is used to access each electrode. The entire mirror is kept extremely thin ($<$ 1.0 mm) and thus lightweight ($\sim$ 2.5 kg/m^2). The mirror is free-standing, requiring no backing structure for support, and therefore large actuation capabilities can be achieved. Surface replication along with subsequent bonding/transfer techniques are implemented throughout the fabrication process, eliminating the need for grinding/polishing steps.

There are a number of challenges in the realization of such a concept. First, constructing thin CFRP shell structures with highly-accurate shapes in the absence of a backing structure is extremely difficult. CFRP materials are highly orthotropic, manufactured at elevated temperatures, and often exhibit variations in material properties throughout the laminate. Therefore large thermal stresses and thus shape errors have the potential to develop. For mirror applications it is desired to minimize these shape errors as much as possible. Second, the integration of additional material layers onto the CFRP substrate through subsequent bonding processes can introduce further shape errors into the structure. Mismatching initial geometry, differing coefficient of thermal expansions (CTEs), and variations in the bond-line between the substrates prove to be important in these steps. Third, the active layer must be designed carefully with respect to the CFRP substrate in order to provide adequate actuation characteristics. The relative thickness ratio between the two layers as well as optimal electrode patterns must be taken into consideration. Non-linear actuation properties of the active material are also of concern. Finally, traditional optical measurement techniques can prove inadequate in their ability to capture 1) the initial figure and 2) the large actuation capabilities

associated with mirrors of this design. Therefore, custom techniques are required in order to perform shape correction experiments.

The overall objective of this research is to address the challenges above by understanding the deformation mechanics behind thin, multi-layer shell structures. Using this knowledge, progress has been made in the realization of a new active mirror technology of high-quality figure. The specific objectives are as follows: 1) Study the imperfections associated with ultra-thin CFRP materials and their effect on post-cure figure errors. With this understanding it is intended to develop methods of manufacturing highly-accurate, thin, free-standing CFRP shell substrates. 2) Understand the mechanics associated with integrating additional material layers into the CFRP substrate without distorting the overall figure. 3) Characterize the actuation response of thin active materials and their ability to make corrections to the as-manufactured figure of the mirror. Finally, 4) characterize the ability to correct for manufacturing-induced errors in an experimental setting.

1.3 Outline of Thesis

The thesis is structured as follows: Chapter 2 provides an overview of the design decisions made throughout the development of the active mirror prototype. Details of each functional layer in the mirror are provided along with challenges associated in implementing them into the design.

Chapter 3 is a study characterizing the imperfections associated with thin CFRP materials. The study is focused on ultra-thin nominally symmetric laminates of reduced ply-count. The relevant imperfections are identified and characterized in an experimental setting. Two classifications of imperfections are considered: those that are spatially uniform with respect to the in-plane dimension of the laminates and those that vary spatially within each ply. The corresponding post-cure shape errors produced as a result of these imperfections are studied. Predictions made through numerical models are compared to experimental measurements.

Chapter 4 considers more practical laminates consisting of thicker plies and higher ply-counts. The mechanical response of various laminate orientations is analyzed. 8, 16, and 32-ply laminates are considered and their post-cure shape errors are characterized. Two methods of reducing the magnitude of these shape errors are outlined. The first implements a change to the nominal cure cycle where a long-duration low-temperature autoclave cure is performed in order to reduce the overall level of thermal stresses developed within the laminate. The second utilizes an adjustable mandrel such that systematic shape errors can be corrected for by changing the shape of the mandrel prior to cure.

Chapter 5 details the challenges associated with incorporating the nanolaminate facesheet into the design of the mirror. A successful bonding process is identified in order to obtain the necessary surface quality without introducing figure errors.

Chapter 6 studies the effect of bonding multiple initially flat active plates to the backside of a spherical CFRP mirror substrate. The non-linear stress distributions within the plates are studied prior to bonding

as well as the figure changes produced subsequent to the bonding process. Comparisons are made between bonding a continuous plate vs. discontinuous plates through numerical models. The models are then adapted to study the highly-localized deformation produced at the discontinuities between each plate. The effect of transverse shear is also considered through the implementation of continuum shell elements that are able to capture highly-localized shear deformations. Comparisons to a limited set of experimental measurements are made for both cases.

Chapter 7 provides an overview of the actuation procedure used to perform shape-correction. An overview of the materials used for actuation is presented along with an experimental characterization of their actuation capabilities. A brief study is performed in order to size the thickness of the active layer with respect to the CFRP substrate for three laminate configurations. An overview of the shape correction procedure is presented and numerical simulations on the performance of an optimized electrode pattern are performed. The correctability and stroke associated with this design are presented across several modes of deformation.

Chapter 8 details the experimental characterization of an active mirror prototype. Two methods of wavefront characterization are outlined leading to the design of a custom dual-stage metrology system implemented in the lab. An overview of the system along with a verification of its ability to reconstruct surface figures is presented. The actuation capabilities of a fully-integrated mirror prototype are characterized along with results pertaining to a shape-correction experiment.

Finally, conclusions, along with areas of future research are presented in Chapter 8.

Chapter 2

Active Mirror Design

This chapter outlines the basic optical requirements and design considerations made for the active mirror concept. Specifically, details on the mirror substrate, reflective front surface, and active layer are presented. Considerations related to electrode wiring and mounting are also described. An overview of the final manufacturing process is presented at the end of the chapter.

2.1 Requirements on Mirror

2.1.1 Figure Accuracy

Diffraction dictates the maximum angular resolution achievable by an optical system [20]. For a telescope, this is defined by

$$\theta = 1.22\lambda/D \tag{2.1}$$

where θ is the angular separation of two point sources, D is the diameter of the telescope, and λ is the wavelength of light under study. For a telescope to be considered "diffraction limited", all optical elements must be of high-enough quality in order for this resolution to remain. Alternatively, this can be stated that the diameter of the telescope is the only physically limiting parameter in the design (for a given wavelength of light). From the Rayleigh Criterion [21], it was determined that this is indeed the case if the final wavefront at the focal plane is accurate to within $\lambda/4$ RMS. Due to reflection, this translates into a requirement on mirror figure accuracy of $\lambda/8$ RMS. To accommodate imperfections in additional optical elements, often more stringent requirements of $\lambda/10$ - $\lambda/20$ are placed on the accuracy of the primary mirror.

Table 2.1 lists several wavelength regimes within the electromagnetic spectrum, their associated wavelength values, along with the $\lambda/10$ requirement on figure accuracy. For visible-wavelength observations, an accuracy of 40 - 70 nm RMS is required on the mirrors. This is used as the baseline requirement for the active mirror concept in this study.

Table 2.1: Requirements on mirror figure at various wavelengths

Class	**λ**	**λ/10**
Ultraviolet	10 nm - 400 nm	1 nm - 40 nm
Visible	400 nm - 700 nm	40 nm - 70 nm
Infrared	700 nm - 1 mm	70 nm - 100 μm
Microwave	1 mm - 1 m	100 μm - 100 mm

2.1.2 Surface Roughness

Surface roughness inherently decreases the reflectively of a mirror due to light scattering. From [22, 23] this effect can be described in terms of the ratio of reflected radiant power to total incoming radiant power for a given material, as follows:

$$\frac{R_s}{R_t} = exp\Big[- (4\pi cos\phi_i \sigma/\lambda)^2 \Big] \tag{2.2}$$

where R_s is the specular reflectance, R_t is the total reflectance (ie. from a perfect surface), ϕ_i is the angle of incidence, σ is the RMS roughness of the surface and λ is the wavelength of light under study. Figure 2.1 displays the results of this relation at normal incidence ($\phi_i = 0°$) for UV, visible and Mid-IR wavelengths. Due to their short wavelengths, the specular reflectance in the UV and visible regimes are observed to be highly sensitive to surface roughness issues. This plot can be used to define the maximum surface roughness based on the desired reflectivity. For example, if a specular reflectance of 98 % is desired for visible wavelength observations, an RMS surface roughness of < 6 nm is required.

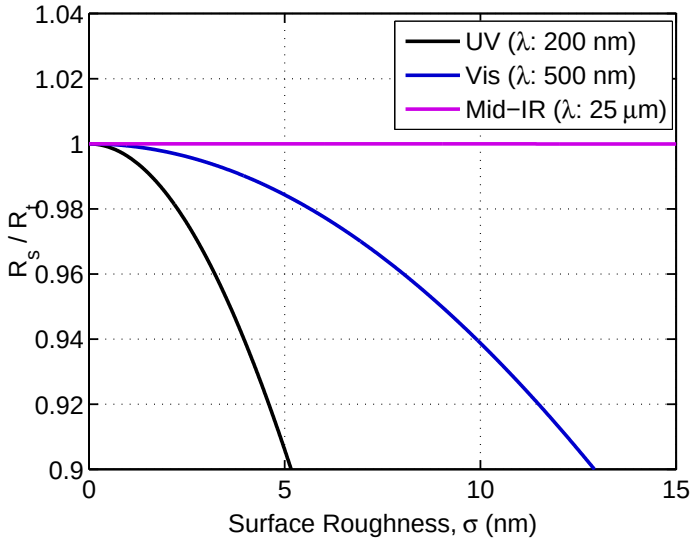

Figure 2.1: Ratio of specular reflectance, R_s, to total reflectance, R_t, at normal incidence.

2.2 Mirror Substrate

Replication techniques were chosen as the manufacturing process for the mirror substrate due to its simplicity and high manufacturing throughput. This imposes limitations on the types of materials to be used as they must be capable of being formed by molding techniques. Polymers are obvious candidate materials due to their ability to flow and conform to an underlying surface before curing. However, polymers exhibit low-stiffness and dimensional stability. A method to alleviate these issues is to implement reinforcing materials. These reinforcements can be of the particulate or fiber variety. Particulate reinforcements, such as ceramic beads or carbon nano-tubes [24], reinforce the polymer material isotropically while fibers increase stiffness primarily in one direction. However, the continuous nature of the fibers allow for a much higher increase in stiffness in comparison to dispersed particles. Multiple layers at differing fiber orientations can be used to produce a substrate with quasi-isotropic properties.

For the purposes of this study carbon-fiber reinforced polymer (CFRP) materials were implemented. Specifically, multiple plies of pre-impregnated unidirectional carbon fibers and epoxy resin are used. Thin-ply materials were selected in order to keep the substrate thin while allowing for increased design variability in laminate orientation. Two types of of carbon fibers were used for this study; T800 and M55J. A mechanical characterization of the orthotropic properties in the unidirectional state was performed for each material. The results of these studies are presented in Table 2.2. A fiber areal weight (FAW) of 17 g/m^2 (gsm) corresponding to a ply thickness of $\sim$ 20 μm was achievable for the T800 material. This represents a reduction of 4 - 10 in the thickness of each ply in comparison to traditional CFRP materials. The M55J material had a FAW of 30 gsm and was used for the remainder of the studies as well as mirror fabrication.

Table 2.2: Material properties of unidirectional T800 and M55J carbon fibers embedded in ThinPreg^{TM}120EPHTg-1 epoxy ($V_f \approx 50\%$).

Property	T800	M55J*
E_1 (GPa)	128	340
E_2 (GPa)	6.5	6.0
G_{12} (GPa)	7.5	4.2
ν_{12}	0.35	0.35

*M55J characterization courtesy of Yuchen Wei.

Several laminate orientations were considered, however a 16-ply $[0°/+45°/\text{-}45°/90°]_s + [90°/\text{-}45°/+45°/0°]_s$ orientation was used extensively in experimental settings (a more detailed analysis of laminate orientation is presented in Chapter 4). This laminate has a total thickness of 480 μm and an areal density of 0.90 kg/m^2. 150 mm diameter octagonal substrates were used for this effort. The octagonal shape was chosen due to symmetry about orthogonal axes as well as practical considerations during manufacturing (alignment of edges with fiber directions). However, as octagons cannot be tessellated, a change to hexagons may be

desired for future efforts.

To construct the mirror substrate, the laminate is laid-up initially flat and then placed atop the mandrel used for cure. The mandrel is spherical with a nominal 2.0 m ROC, thus producing nominally spherical mirror substrates. It is first treated with a release agent (Frekote 770NC) in order to prevent the part from curing to the surface. A 1/4" thick soft silicone pad is placed directly onto the backside of the laminate. This allows for an even pressure distribution to be obtained for subsequent vacuum-bagging and autoclave cure. Details of the curing process as well as process alterations implemented to mitigate post-cure shape errors are presented in Chapter 4.

2.3 Reflective Front Surface

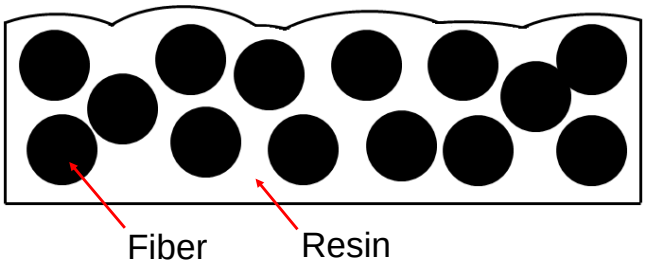

Figure 2.2: Schematic of fiber print-through.

Surface roughness issues due to fiber print-through are prevalent for CFRP-based optics. The effect of fiber print-through is depicted schematically in Figure 2.2 where thermal contraction of the resin causes the fibers to protrude through the terminal surface of the laminate, ultimately producing roughness. Two methods of mitigating these effects were considered and summarized here. The first method implements a secondary replication process where a resin-rich layer is added to the front surface of the mirror. This is performed by placing a central pool of epoxy onto the surface of a glass mandrel (ie. the mandrel used for the initial replication process) and then placing the cured CFRP substrate onto this assembly as shown in Figure 2.3. A room-temperature cure is then performed under atmospheric pressure. The added thickness of the resin-layer attenuates the surface roughness producing a smooth surface. However, with this method, moisture absorption issues are of concern due to the high surface area of the resin-rich layer. This can potentially cause significant distortions to the mirror figure over time. In addition, improper release from the mandrel was also found to be an issue causing small "lift-off" errors throughout the surface.

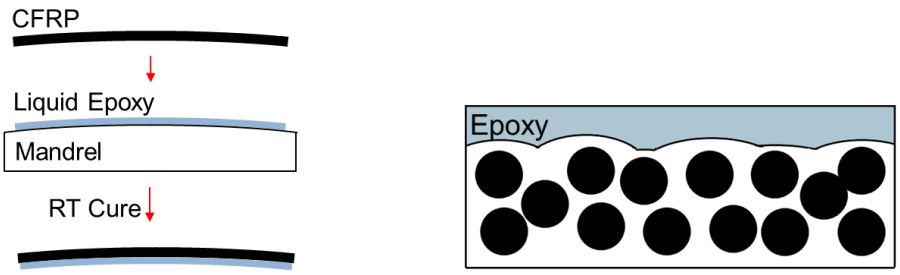

Figure 2.3: Schematic of resin-rich cure process used to mitigate fiber print-through.

The second method was the incorporation of a nanolaminate facesheet onto the front of the CFRP substrate. Nanolaminates are multilayer metal foils formed by sputter deposition on a precision glass mandrel [25, 26]. The surface quality of the nanolaminate is dependent entirely on the roughness of the deposition mandrel and has been demonstrated down to < 1 nm RMS. The bonding process is very similar to that of the resin-rich layer and is depicted in Figure 2.4. A detailed overview of the nanolaminate bonding process is presented in Chapter 5. While this method still incorporates a layer of resin, the nanolaminate acts to seal the surface and therefore moisture absorption issues are not of great concern. Ultimately, this was chosen as the optimal route for mirror development due to the increase in potential surface quality. For the current effort 50 μm thick nanolaminates composed of Cu and Zr layers were used. A terminal Au layer is implemented for the reflective front surface. Nanolaminates have been demonstrated on meter-scale parts and are thus scalable technologies.

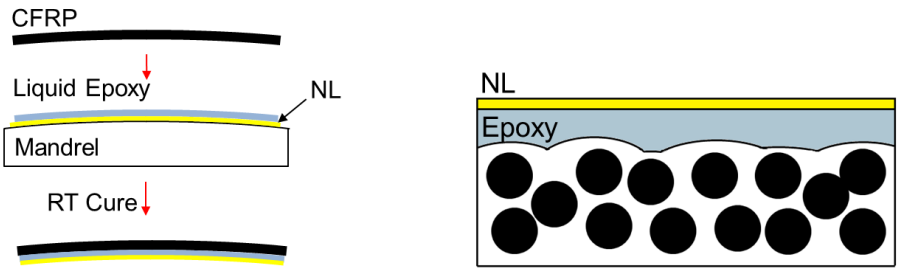

Figure 2.4: Schematic of nanolaminate bonding process used to mitigate fiber print-through.

2.4 Active Layer

Several materials were considered for the active layer. Previous efforts have incorporated thin films of piezoelectric polymers [17, 27] in order to provide the actuation capabilities. However, due to the low modulus of these polymers their associated actuation stroke is insufficient in order to impose meaningful deformations onto the stiff CFRP substrate. Piezoelectric and electrostrictive ceramics are more suitable materials due to their high stiffness and actuation capabilities. They have also been implemented extensively

in various active structures. Therefore, these materials were implemented for the present study with a focus on piezoelectric ceramics. Specifically, Lead-Zirconate-Titanate (PZT) was used. The properties of this material can be found in Table 2.3.

Table 2.3: Material properties for PZT-5A.

Property	Value
Modulus, E (GPa)	66.0
Poisson's Ratio, ν	0.35
Piezoelectric Constant*, d31 (pC/N)	-375
Maximum Electric Field*, E_{max} (MV/m)	0.8

*Measured value

125 μm thick flat PZT plates were used as the active elements for the mirror substrate. The plates are initially 72.5 x 72.5 mm square but trimmed to a section of an octagon using a high-speed cutting disk. The octagonal shape of the mirror also has the added benefit of accommodating identically sized plates here. The material is initially poled with continuous nickel electrodes on either side. In order to apply the custom electrode pattern, these electrodes were removed using a wet nickel-stripping agent (Caswell B-9). A materials printer (Dimatix 2800) and silver nano-particle ink (Methode 9104) was used to reprint the continuous ground plane on one side as well as the optimized pattern on the other (the pattern details can be found in Chapter 7). For optimal conductivity, the ink must be sintered at 200 °C for 2 hrs. The plates are bonded to the CFRP substrate using room-temperature cure epoxy and vacuum-bagging techniques. Figure 2.5 displays the active layer with the custom electrode pattern on the backside of the mirror. Details of the custom electrode pattern can be found in [17, 28].

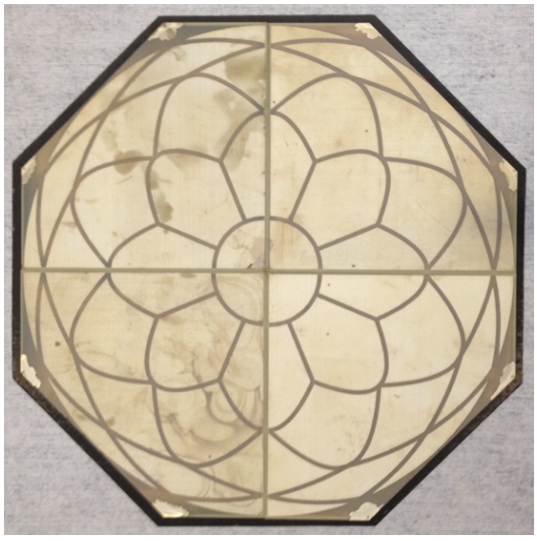

Figure 2.5: Backside of a 150 mm dia. active mirror prototype containing four PZT-5A plates with a custom electrode pattern.

2.5 Electrode Routing Layer

Due to the relatively large number of actuation channels, active mirrors often contain cluttered, bulky and massive connecting wires that can impart shape errors onto the mirror surface. This is a particular problem for the current design as the mirrors are extremely thin and thus susceptible to the mechanical constraints imposed by such wires. To alleviate this problem, conductive electrode traces are printed on a 25 μm thick Kapton routing layer using the materials printer and conductive ink. Connections to the underlying electrode pads are then made using through-thickness vias and conductive epoxy. The pattern is designed to route the traces away from the active surface of the mirror to a flex-cable connector where connections to the control electronics can be made using more standard cabling techniques. The low modulus and thickness of the Kapton layer allows the mirror to remain highly flexible during actuation. Figure 2.6 displays the backside of a mirror after integration of the electrode routing layer.

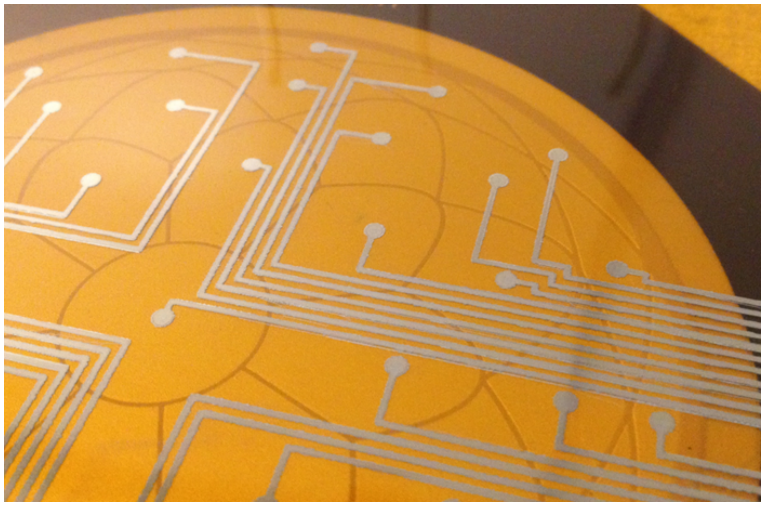

Figure 2.6: Backside of an active CFRP mirror after electrode routing layer integration.

2.6 Mounting

Figure 2.7 displays the mounting scheme used to hold the active mirrors. Spherical magnets placed at three locations on the mirror surface are used to provide a quasi-kinematic mount. Two magnets are placed at each location on the top and bottom surfaces of the mirror. The magnetic flux lines run perpendicular to the mirror surface, ensuring that the magnets are self-aligned. This prevents unwanted distortions from occurring while allowing the mirror to deform freely upon actuation. This concept is adapted from that presented in [17].

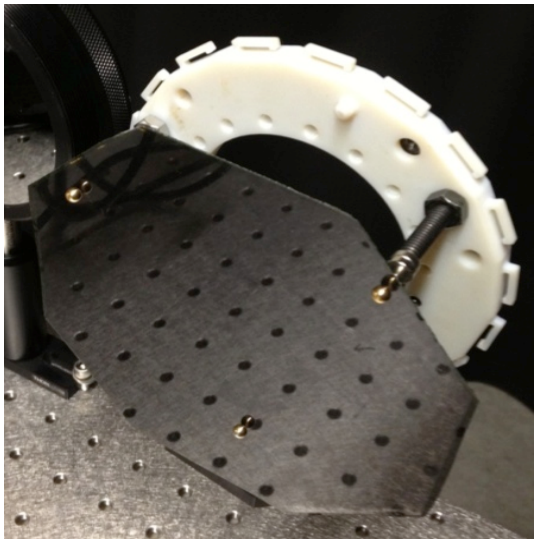

Figure 2.7: Bare CFRP substrate mounted using spherical magnets.

2.7 Overview of Fabrication Process

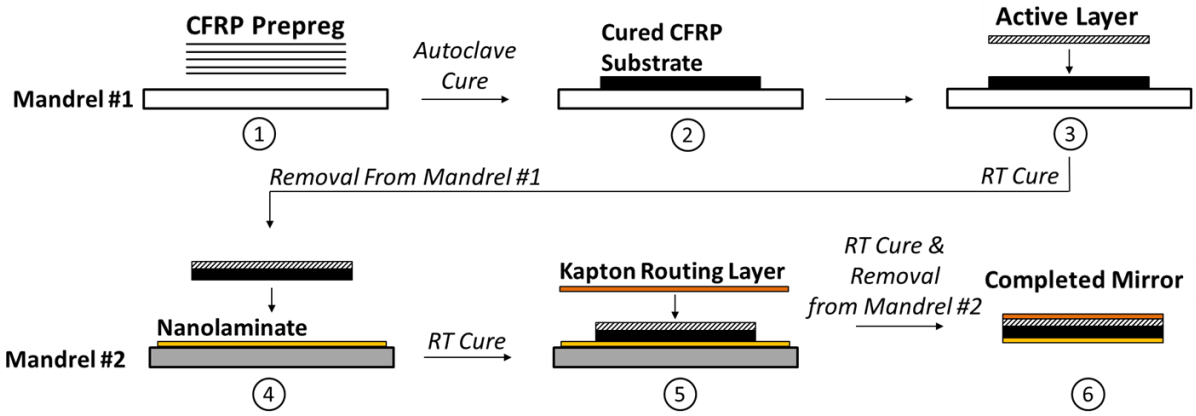

Figure 2.8: Overview of fabrication process.

Figure 2.8 is a schematic of the overall fabrication process for the mirror prototypes. First, a lay-up of unidirectional carbon fiber prepreg is placed on top of a mandrel. The laminate is vacuum bagged and autoclave cured at elevated temperature and pressure to provide consolidation of the plies. During this process the CFRP material replicates the surface of the underlying mandrel, providing the overall figure of the mirror. Upon cure, the active layer layer is bonded to the backside of the CFRP substrate with the mandrel underneath to provide support. A common ground plane and patterned electrodes are printed on the bottom/top of the active layer before the bonding process takes place. Once cured, the assembly is removed from the underlying mandrel and bonded to a nanolaminate facesheet. The nanolaminate is deposited

on a separate mandrel with the same figure as that used for the CFRP replication process, producing a matching part. Care must be taken in order to ensure a uniform thickness distribution of epoxy between the CFRP substrate and nanolaminate during this bonding process. The Kapton electrode routing layer is then incorporated onto the backside of the mirror using conductive epoxy, providing a method to route the actuation channels to the supporting electronics. Lastly, the completed active mirror is parted from the secondary mandrel.

Chapter 3

Imperfections in Symmetric Thin-Ply Composites

3.1 Introduction

Advancements in tow-spreading techniques [29, 30] have allowed for the production of extremely thin carbon fiber composite materials. The benefits of using such material have been widely studied, demonstrating an increase in mechanical performance [29, 31, 32]. The thin nature of this material also allows for the construction of extremely thin structures. Symmetric, multi-ply laminates with quasi-isotropic properties can be constructed while keeping the overall laminate thickness extremely low (< 200 μm). These thin laminates are attractive when considering lightweight shell structures for aerospace applications. In the context of replicated composite optics, this potentially enables mirror designs that can be folded into a compact initial state and then deployed upon orbit. An example of this concept is shown in Figure 3.1. However, the stringent requirements on surface accuracy remain. Therefore, it is desired to study here the post-cure shape accuracy of ultra-thin composite laminates.

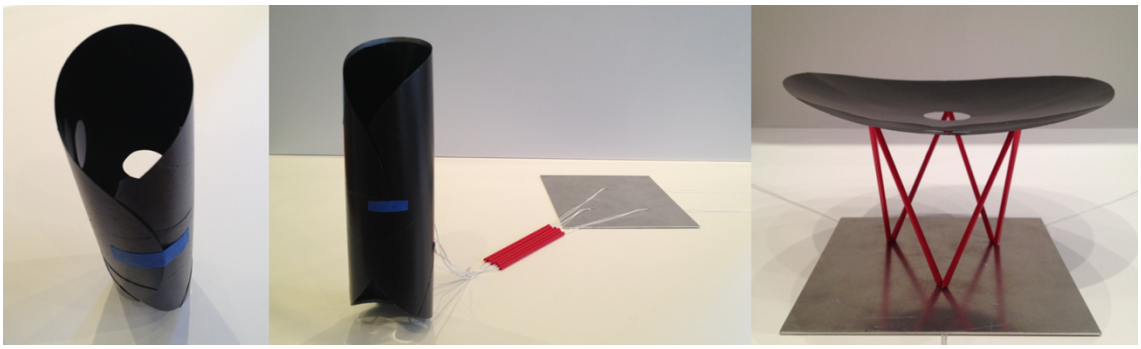

Figure 3.1: Folding concept envisioned for extremely thin lightweight mirrors.

3.1.1 Background

Achieving highly-accurate shapes in laminated structures is a difficult process. Significant internal stresses develop during thermal curing due to the highly orthotropic nature of the individual plies. Under uniform curing conditions and with symmetric laminates, it is predicted that the stresses will be balanced through the thickness and therefore zero out-of-plane deformations will occur. If cured on a flat surface under these ideal conditions, the laminate is expected to remain flat. However, deviations from this ideal case break the laminate symmetry, creating an imbalance in thermal stresses, ultimately resulting in post-cure shape errors.

These symmetry-breaking variations can occur due to a number of factors. The first is related to variations in the homogenized properties of the plies. Several studies have been performed in order to characterize the magnitude of fiber misalignment within a ply [33, 34] and assess its effect on mechanical and thermal properties [35, 36, 37, 38, 39]. Errors in the through-thickness distribution of fibers within a ply have also been shown to be a factor [40]. Finally, simple variations in thickness will change the overall stiffness of each ply. These factors have the potential to produce variations within a single ply as well as between successive plies within a laminate.

Errors in the relative orientation of successive plies can also break the intended symmetry of a laminate. Hinckley [41] performed Monte Carlo analyses to assess the effect of ply misalignment on mechanical and thermal properties for various laminate orientations. Arao [42] performed a study to assess the effect of ply misalignment on the post-cured shape error of symmetric laminates. Significant twisting deformations were predicted in these studies in spite of the nominally symmetric laminate orientation. However, both of these studies were conducted for laminates constructed from relatively thick materials.

Finally, variations in the curing conditions during processing can also result in the development of shape errors. It has been shown that thermal gradients during curing can produce large out-of-plane deformations [43, 44].

3.1.2 Objective and Scope

The present study attempts to 1) identify the relevant imperfections associated with thin-ply fiber reinforced composites, 2) experimentally quantify the magnitude of these imperfections, and 3) assess their effect on post-cure shape errors for flat laminates.

4-ply symmetric laminates constructed from ultra-thin materials are considered. Each ply has a nominal thickness of 20 μm and therefore the total thickness of the laminate is only 80 μm. This represents a factor of 5-10 reduction in thickness than traditional composite parts. The study is separated into two parts based on the nature of the imperfections. In the first section, imperfections that vary uniformly across a single ply or between plies are considered. Specifically, misalignments in the orientation of each ply, uniform variations in the mean thickness of each ply and through-thickness thermal gradients during the curing process are studied. In the second section, imperfections that vary *within* each ply are studied. Spatial variations in ply

thickness and fiber orientation are considered.

3.2 Spatially-Uniform Imperfections

3.2.1 Problem Formulation

In order to identify the spatially-uniform imperfections, a study was performed using Classical Lamination Theory (CLT)[45]. CLT assumes geometric and material linearity and is used to predict the mid-plane strains and out-of-plane curvature changes of a laminate under load. The problem can be structured as follows: given a laminate constructed from n separate plies, the 6x6 **ABD** stiffness matrix can be assembled relating mid-plane strains and out-of-plane curvatures, $\boldsymbol{\epsilon}$ and $\boldsymbol{\kappa}$, to resultant forces and moments, $\mathbf{N}$ and $\mathbf{M}$, respectively, as follows:

$$\begin{bmatrix} \boldsymbol{\epsilon} \\ \boldsymbol{\kappa} \end{bmatrix} = \begin{bmatrix} \mathbf{A} & \mathbf{B} \\ \mathbf{B} & \mathbf{D} \end{bmatrix}^{-1} \begin{bmatrix} \mathbf{N} \\ \mathbf{M} \end{bmatrix} \tag{3.1}$$

where

$$\mathbf{A} = \sum_{k=1}^{n} \mathbf{Q_k}(z_k - z_{k-1}), \tag{3.2}$$

$$\mathbf{B} = 1/2 \sum_{k=1}^{n} \mathbf{Q_k}(z_k^2 - z_{k-1}^2), \tag{3.3}$$

$$\mathbf{D} = 1/3 \sum_{k=1}^{n} \mathbf{Q_k}(z_k^3 - z_{k-1}^3). \tag{3.4}$$

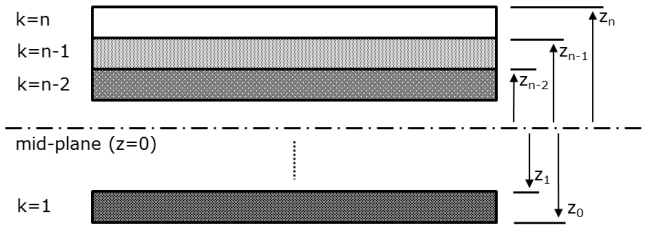

Figure 3.2: Through-thickness coordinate definition for Classical Lamination Theory.

$\mathbf{Q_k}$ is the orthotropic stiffness matrix of the k^{th} ply in the laminate coordinate system (x/y) and z_k is the through-thickness interface coordinate of that ply and its neighbor, as shown in Figure 3.2. $\mathbf{Q_k}$ is dependent on the material properties of the k^{th} ply, as well as the orientation of the ply with respect to the global coordinate system. For each ply it is defined as

$$\mathbf{Q_k} = [T]_k^{-1}[\mathbf{Q_k^{PMC}}][T]_k^{-T}, \tag{3.5}$$

where $\mathbf{Q_k^{PMC}}$ is the stiffness matrix of the k^{th} ply in the prime material coordinate (PMC) system. The PMC system is aligned parallel and perpendicular to the nominal fiber direction for this study. $[T]_k$ is a rotation matrix dependent on the ply orientation and is defined as

$$[T]_k = \begin{bmatrix} c^2 & s^2 & 2cs \\ s^2 & c^2 & -2cs \\ -cs & cs & c^2 - s^2 \end{bmatrix} \tag{3.6}$$

with

$$s = sin(\theta_k), \tag{3.7}$$

$$c = cos(\theta_k), \tag{3.8}$$

where θ_k is the orientation of the kth ply with respect to the global reference frame (about the z-axis).

For the present study the mid-plane strains and out-of-plane curvatures produced after the laminate has been cured and returned to room-temperature are of interest. These are produced as a result of the internal thermal stresses developed during cure. These stresses can be expressed as resultant thermal forces and moments, $\mathbf{N_{Thermal}}$ and $\mathbf{M_{Thermal}}$, respectively, as follows:

$$\mathbf{N_{Thermal}} = \sum_{k=1}^{n} \int_{z_{k-1}}^{z_k} \mathbf{Q_k} \boldsymbol{\alpha}_k \Delta T dz, \tag{3.9}$$

$$\mathbf{M_{Thermal}} = \sum_{k=1}^{n} \int_{z_{k-1}}^{z_k} \mathbf{Q_k} \boldsymbol{\alpha}_k \Delta T z dz, \tag{3.10}$$

where $\alpha_\mathbf{k}$ is an array of in-plane thermal expansion coefficients for the k^{th} material and ΔT is the temperature change experienced during cooling. $\alpha_\mathbf{k}$ also depends on the orientation of the fibers within a ply and is defined as

$$\alpha_\mathbf{k} = [R][T]^{-1}[R]^{-1}[\alpha_\mathbf{k}^{\mathbf{PMC}}], \tag{3.11}$$

where $\alpha_\mathbf{k}^{\mathbf{PMC}}$ is the array of thermal expansion coefficients for the k^{th} layer in the PMC system and $\mathbf{R} = \text{diag}\{1, 1, 2\}$.

Therefore, Equation 3.1 becomes

$$\begin{bmatrix} \boldsymbol{\epsilon} \\ \boldsymbol{\kappa} \end{bmatrix} = \begin{bmatrix} \mathbf{A} & \mathbf{B} \\ \mathbf{B} & \mathbf{D} \end{bmatrix}^{-1} \begin{bmatrix} \mathbf{N_{Thermal}} \\ \mathbf{M_{Thermal}} \end{bmatrix} \tag{3.12}$$

and the out-of-plane curvatures produced during cure can be predicted.

In this formulation, several assumptions are made. Firstly, it is assumed that the laminate is in an

unstressed state after the completion of the cure. Second, after this process the material is linear elastic with properties independent of temperature. Third, the laminate is unconstrained and therefore free to deform during cooling. These assumptions are known to be partially invalid in a practical setting. However, they allow for an initial investigation into the thermal deformations produced during cure.

3.2.1.1 Identification of Relevant Parameters

Using the formulation above, the conditions required to ensure out-of-plane curvature changes do not arise during cooling can be identified. Firstly, it is observed through Equation 3.9 that upon integration, the resultant thermal forces are always non-zero during cool-down. Therefore, from Equation 3.1 the **B** matrix must be null and thus no coupling between out-of-plane curvatures, $\boldsymbol{\kappa}$, and resultant thermal forces, $\mathbf{N_{thermal}}$, must exist. The first condition required for this to be satisfied is that plies opposite one another from the neutral axis must have identical thicknesses, t_k. This can be expressed as

$$t_k = t_{[n-(k-1)]}, \tag{3.13}$$

with k=1, 2, ..., n/2 for a laminate with an even ply count. The second condition is that opposing plies must possess identical stiffness matrices, $\mathbf{Q_k}$. From Equations 3.5 and 3.6, this requirement reduces to a constraint on the ply orientation, θ_k (assuming identical properties in the PMC reference frame). Therefore

$$\theta_k = \theta_{[n-(k-1)]}. \tag{3.14}$$

.

Additionally, as **D** is never null for practical laminates there must be zero thermal moments, $\mathbf{M_{thermal}}$, developed during cure. From Equation 3.10 it can be deduced that this condition is satisfied if perfectly symmetric lamination conditions exist and the laminate undergoes a uniform temperature change during cooling. Namely, opposing plies must have identical mechanical and thermal properties ($\mathbf{Q_k^{PMC}}$, $\alpha_\mathbf{k}^{\mathbf{PMC}}$), fiber orientation, θ_k, equal thicknesses, t_k, and ΔT must not be a function of the through-thickness coordinate. Therefore,

$$\Delta T \neq \Delta T(z). \tag{3.15}$$

.

From Equations 3.13, 3.14, and 3.15 three relevant factors can be identified: 1) variations in ply thickness, 2) variations in ply orientation and 3) through-thickness thermal-gradients during cure, all of which can result in the formation of out-of-plane deformations upon cooling.

Table 3.1: Orthotropic properties of unidirectional T800 carbon fibers embedded in ThinPreg^{TM}120EPHTg-1 epoxy ($V_f \approx 60\%$).

Property	Value
E_1 (GPa)	127.9
E_2 (GPa)	6.5
G_{12} (GPa)	7.5
ν_{12}	0.35
α_1 (ppm/°C)	0.0
α_2 (ppm/°C)	20.0

3.2.2 Characterization of Spatially-Invariant Imperfections

This section outlines the procedures used to experimentally characterize the imperfections mentioned above. To do so, 100 mm square laminate coupons were constructed. Symmetric 4-ply, $[0°/90°]_s$ flat laminates were used for this study as they are the thinnest symmetric laminates possible. The coupons were constructed from material comprised of T800 fibers embedded in an epoxy matrix. The material was in an initial prepreg form with a resin content of 38% by weight and each ply had a fiber areal weight (FAW) of 17gsm. The coupons were laminated and cured atop a flat glass plate. A compliant silicone backing pad was used to provide an even pressure distribution during cure. The laminates were vacuum bagged and autoclave cured at a temperature of 120°C for 2 hours and under an external pressure of 80 psi. The rate of loading and unloading were 2 °C/min and 3 psi/min for the temperature and pressure profiles, respectively. The mechanical and thermal (CTE) properties of the T800 material were measured experimentally prior to the study and are listed in Table 3.1.

3.2.2.1 Thickness Variations

Ply thickness measurements were made using micrographs of the laminate cross-section and calibrated objective lenses. Images were captured using a Nikon LV-150 microscope. Specimens were first cross-sected and potted in clear casting epoxy. Once cured, the specimens were lapped down using a series of grinding wheels and polished to the desired surface finish for imaging. This allowed the plies as well as individual fibers to be imaged.

Figure 3.3 is a micrograph of a 4-ply specimen oriented with the 0° fiber direction out of the plane. From the optical measurements, it can be seen that the top and bottom plies do not possess the same thickness values at this location within the laminate. The bottom ply (Ply 4), corresponding to the ply that was directly on the glass plate during cure, is thinner than the top ply (Ply 1). A series of thickness measurements were performed at 2 mm intervals along the 40 mm wide specimen. Table 3.2 summarizes these measurements in terms of the mean and standard deviation in thickness measurements. It is apparent that there is a variation in mean thickness between the plies, ranging from 17.8 μm for the inner plies to 21.1 μm for Ply 1. On average, the bottom ply is thinner than the top-ply.

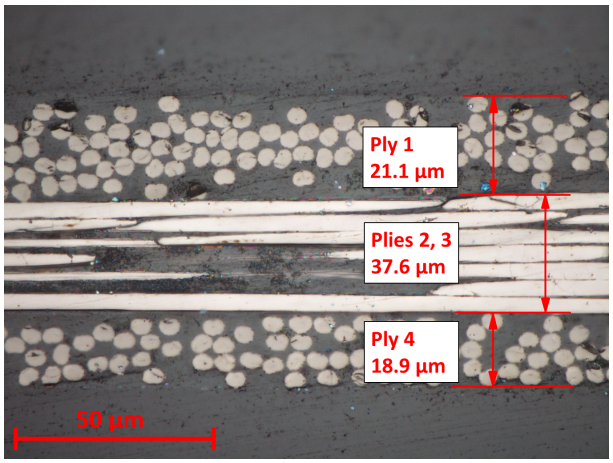

Figure 3.3: Micrograph of laminate cross-section displaying ply thickness measurements.

Table 3.2: Ply thickness measurements.

Ply	Mean Thickness (μm)	Std. Dev. Thickness (μm)
1	21.1	2.6
2/3	17.8	2.0
4	19.8	2.2
Avg	**19.6**	**2.3**

3.2.2.2 Ply Misalignments

Measurements of the ply orientations were performed using optical techniques as well. An existing 8-ply $[0°/45°/\text{-}45°/90°]_s$ laminate was used for this study as the higher number of plies allowed for increased measurements. In order to measure the relative angle of the successive plies it was necessary to expose the inner plies for imaging. To do so, sections of the laminate were polished down in the through-thickness direction at depths corresponding to the various ply interfaces, as shown in Figure 3.4. Multiple images of the now exposed plies, and fibers within, were captured while keeping the specimen fixed to the translation stage.

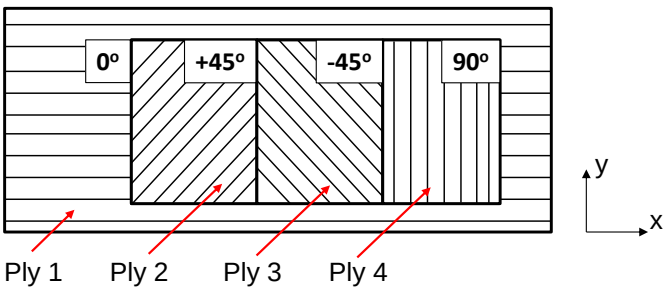

Figure 3.4: Schematic of ply grinding process used to image internal plies.

A Nikon ShuttlePix P-400R digital microscope at 400x total magnification (800 μm field of view) was used to capture images of the plies. The larger field of view was necessary to take fiber angle measurements over longer length scales. The specimen was fixed to a precision XY translation stage, allowing images to be captured at various in-plane locations while maintaining a common reference frame. The orientation of individual fibers within each image were measured using a line-detecting algorithm and custom Matlab script. The algorithm used was a Hough Transform [46], a classic method of detecting features within an image. A total of 250 - 270 fiber angle measurements were performed from 15 images captured at each ply depth. Figure 3.5 displays an image of the fibers along with the line-detection produced using the Hough Transform.

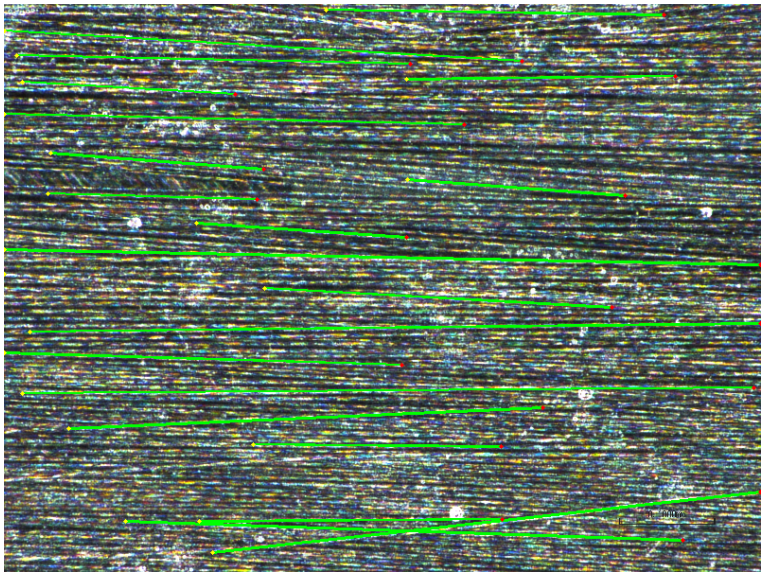

Figure 3.5: Image of line detection algorithm used to perform fiber measurements.

Figure 3.6 displays the measured fiber distributions for each ply along with the mean and standard deviations in fiber angle. It can be seen that the measured fiber angles follow an approximate normal distribution for each ply. As the global reference frame was kept fixed during imaging, the mean fiber orientation of each ply can be compared to the intended laminate orientation, providing an assessment on the accuracy to which the plies have been aligned. As shown in Figure 3.6 it was found that each of the plies were oriented to an accuracy of approximately 0.3°. Therefore it is assumed that this level of misalignment is present for all plies.

3.2.2.3 Thermal Gradients During Cure

The uniformity of temperature conditions during cure was assessed by outfitting a laminate with thermocouples while in the autoclave. The thermocouples were placed on either side of the laminate at two locations, as shown in Figure 3.7(a), allowing temperature readings to be obtained during the cure cycle. Figure 3.7(b)

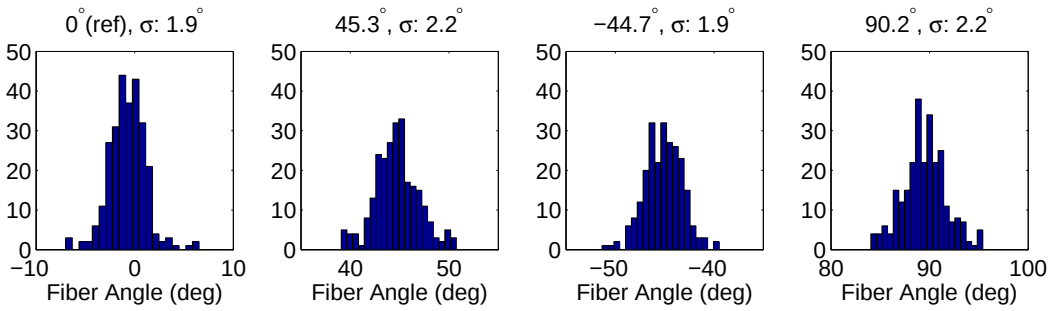

Figure 3.6: Fiber angle measurements of external and internal plies used to assess ply alignment accuracy.

displays the thermal profile during cure with a detailed view of the constant-temperature "soak" section. A maximum through-thickness temperature change of approximately 0.5 °C was measured. The temperature is kept relatively constant throughout this section, with only slight variations observed due to the autoclave control cycle (high-frequency variations are attributed to thermocouple noise). From this study it is apparent that the mandrel-side of the part is at a higher temperature for both thermocouple locations. Due to this increased cure temperature, the mandrel-side of the part will be subject to a higher degree of cooling once the part is brought back down to room temperature. An in-plane temperature variation of approximately 1°C was measured across the surface of the laminate.

3.2.3 Numerical Modeling

While the CLT analysis is useful in identifying relevant parameters causing shape errors, it is limited by the assumption of geometric linearity. This is especially true for very thin laminates, as deflections much greater than the thickness are expected. Therefore, a finite element model was developed to investigate the effect of the above imperfections on post-cure shape errors. The commercial package, Abaqus Standard/CAE 6.12 [47], was implemented with S4R elastic shell elements. The orthotropic material properties of the T800 material outlined in Table 3.1 were defined as the nominal properties of each ply. The laminate orientation was defined using the built-in composite stack lay-up feature. The laminate was modeled as a 4-ply, $[0°/90°]_s$, 250 mm square flat plate constrained at a single node in all 6 degrees of freedom at the center of the plate. Each ply was assigned a nominal thickness of 20 μm. An element size of 2.5 mm was used resulting in 10,000 total elements across the laminate.

A geometrically nonlinear, quasi-static analysis was carried out by imposing a nominal temperature change of -100°C throughout the plate, simulating the cooling process at the end of the cure cycle. This process carries with it the same assumptions mentioned in the CLT formulation; however, geometric non-linearities are handled properly by updating the tangent stiffness matrix throughout the analysis. The following sections outline the procedures used to quantify the effect of each imperfection on the resulting shape errors. Comparisons between the non-linear finite element analysis and linear CLT predictions are

(a)

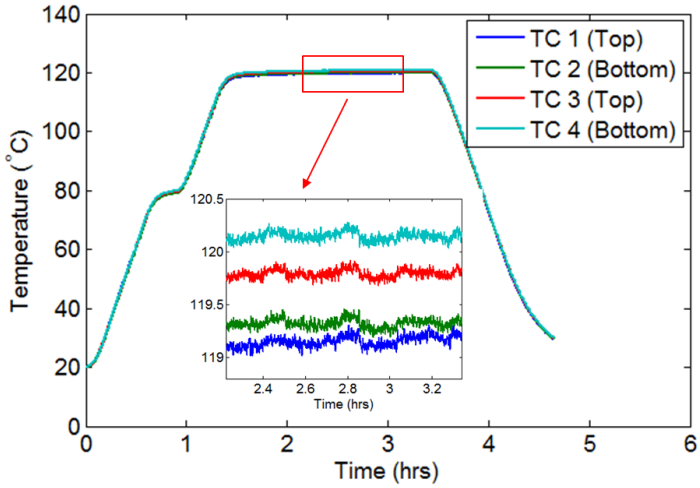

(b)

Figure 3.7: (a) Schematic of thermocouple placement on specimen. (b) Thermocouple readings during autoclave cure.

made.

3.2.3.1 Uniform Variations in Ply Thickness

Figure 3.8 displays the resulting curvature changes, κ_x, κ_y, and κ_{xy}, and RMS shape error due to uniform changes in ply thickness. This was performed by varying the thickness of the top 0° ply while keeping all others fixed. It was assumed that the material properties of that ply remained constant throughout this process.

As evident in Figure 3.8(a), extremely large curvatures arise due to small changes in ply thickness. The dominating curvature change occurs in the y-direction, resulting in the laminate taking on a cylindrical mode of deformation. The CLT prediction of κ_y agrees well with that obtained through the non-linear study. However, a small component of κ_x is predicted in addition to the dominating κ_y not found in the non-linear analysis. From Figure 3.8(b), it can be seen that extremely large shape error magnitudes form over the 250 mm square plate due to small changes in ply thickness. (Note: uniform thickness changes in the internal 90° plies do not result in curvature changes as the laminate remains balanced).

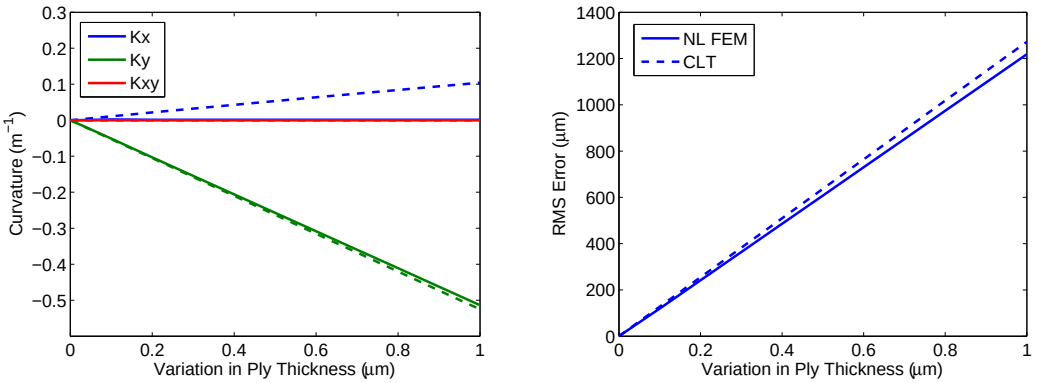

(a) (b)

Figure 3.8: Results of NL FEA (solid) and CLT prediction (dashed) for uniform variations in ply thickness. a) Laminate curvatures and b) resulting shape error magnitudes.

3.2.3.2 Variations in Ply Alignment

The effect of ply misalignments on the post-cured shape of the laminate was studied next. To model this effect, the mean orientation of a single ply was varied in the laminate orientation while keeping all others fixed. Figures 3.9(a) and 3.9(b) display the resulting curvature changes as a function of ply misalignment in the terminal 0° and internal 90° plies, respectively. Figure 3.9(c) displays the corresponding RMS shape error.

Several observations can be made from this study. Firstly, by comparing Figures 3.9(a) and 3.9(b), it is evident that the laminate is more sensitive to variations in the 0° ply orientation in comparison to those

for the 90° ply, as the resulting curvatures are of higher magnitude. This is as expected as the 0° ply is further from the neutral axis of the laminate, thus producing a larger thermally-induced moment from the imbalance. Secondly, for both the 0° and 90° plies, and at small values of ply misalignment, there is good agreement between the results of the non-linear finite element analysis and CLT prediction. At this point, both analyses predict a strong saddle/astigmatic shape, as κ_{xy} is the only non-zero curvature component. As the magnitude of ply misalignment is increased, the non-linear results deviate from the CLT prediction and the rate of growth of κ_{xy} declines. Upon further increase of the ply misalignment, the non-linear analysis captures a mode change in the deformation of the laminate as κ_x and κ_y become non-zero. This point occurs at a misalignment of approximately 0.15° for the 0° ply and 0.3° for the 90° ply. Finally, by studying Figure 3.9(c) it can be seen that significant magnitudes of shape errors arise from small ply misalignments. It is also apparent that the CLT analysis greatly over-predicts the magnitude of shape error during cooling.

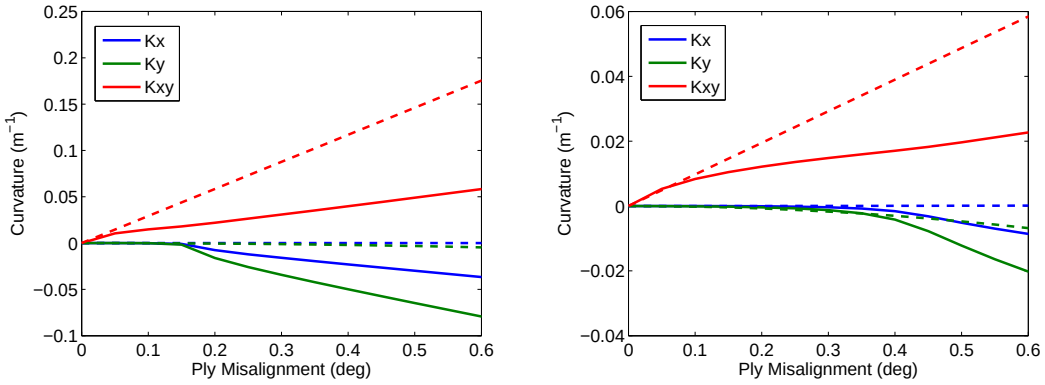

(a) (b)

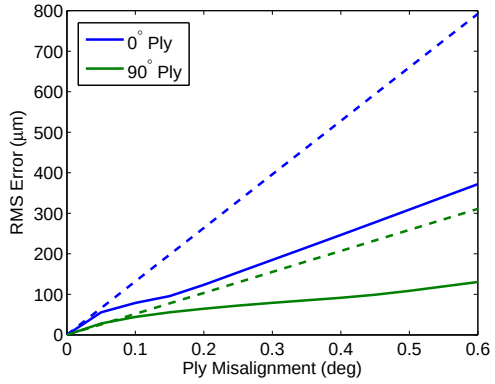

(c)

Figure 3.9: Results of NL FEA (solid) and CLT prediction (dashed) for uniform variations in ply orientation. a) Laminate curvatures and b) resulting shape error magnitudes.

3.2.3.3 Thermal Gradients

Finally, the effect of thermal gradients during cure was studied. The temperature change of the shell mid-plane was set to the nominal value of -100 °C as before; however, a linear variation through the thickness was also defined. Figure 3.10 displays the resulting deformation due to a through-thickness change in temperature. It can be seen that this produces a cylindrical deformation oriented in the y-direction as κ_y is the dominating curvature term. The results of the CLT analysis agree well with that of the non-linear study, as evident by Figure 3.10(b).

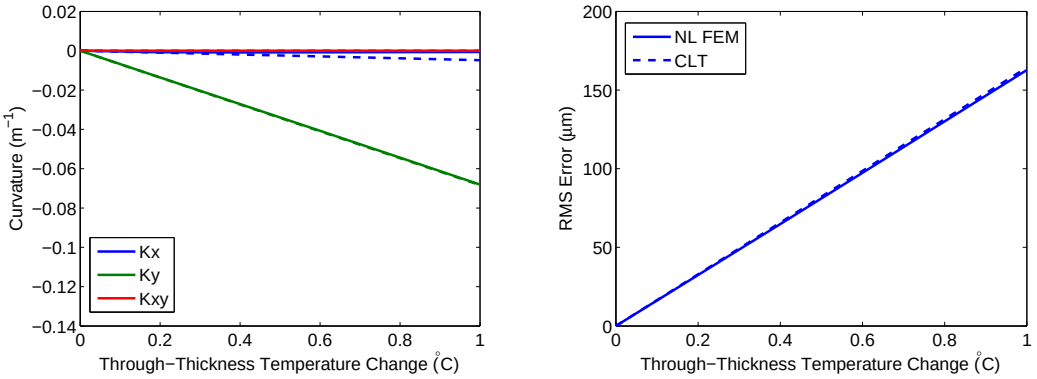

(a) (b)

Figure 3.10: Results of NL FEA (solid) and CLT prediction (dashed) for thermal gradients during cure. a) Laminate curvatures and b) resulting shape error magnitudes.

3.2.3.4 Sensitivity Analysis

In order to compare the relative effect of each imperfection, it was necessary to normalize the magnitude of each. Two methods of normalization were considered: normalization by the full-scale value of imperfection and normalization by the measured values presented in Section 3.2.2. The full-scale values were taken to be 1) the difference between the terminal/internal ply orientations, 2) the total ply thickness, and 3) the full temperature change experienced during cure. The measured values were defined as 1) the maximum deviation in measured ply orientation, 2) the difference in thickness between the top and bottom plies, and 3) the through-thickness difference in temperature measured during cure. Table 3.3 lists these values for each imperfection.

Figure 3.11(a) displays the influence of each imperfection as a fraction of their full-scale value. This method would be useful from a design standpoint if no apriori knowledge of the imperfection magnitudes was available. From this analysis it can be seen that the ply alignment in the 0° ply appears to be the dominating imperfection resulting in an RMS error of approximately 550 μm at 1% the full-scale value. The remaining imperfections have reduced sensitivity, resulting in approximately 200 μm of deformation at their respective 1% magnitudes.

Figure 3.11(b) displays the influence of each imperfection as a fraction of their measured values. This analysis provides insight into the level of shape error reduction that can be achieved if the magnitude of imperfections were to decrease from the current measured values. From this analysis it can be seen that the variation in ply thickness is clearly the dominant factor. The deformation of the laminate is extremely sensitive to variations in this parameter with out-of-plane deformations in excess of 1500 μm RMS.

Table 3.3: Full-scale and standard deviations of imperfections.

Imperfection	Full-Scale Value	Measured Value
Ply Misalignment (deg)	90.0	0.3
Ply Thickness Variation (μm)	20.0	1.3
Through-Thickness Temperature Change (°C)	100.0	0.5

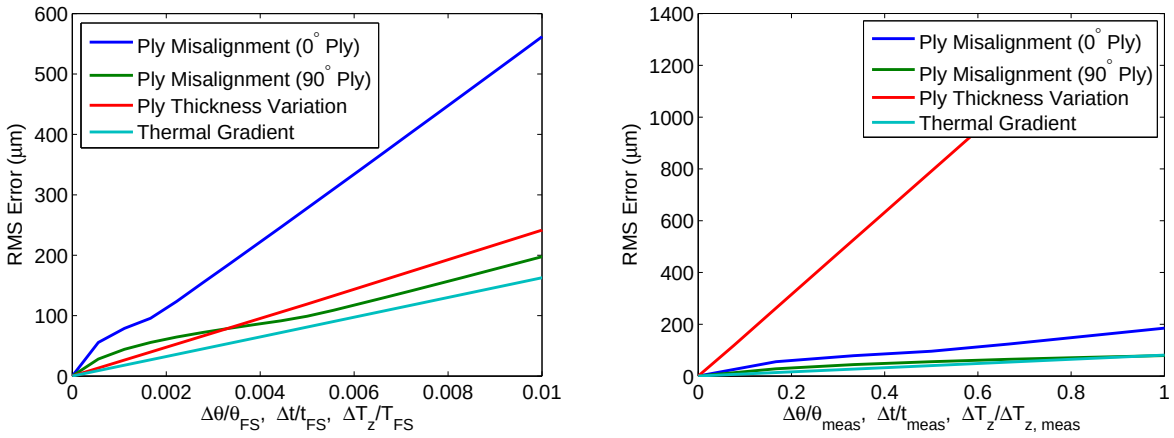

(a) (b)

Figure 3.11: RMS error as a function of imperfection magnitude. Results are normalized by a) the full-scale (FS) values and b) the measured (meas) values in Table 3.3.

3.2.4 Shape Error Measurements

Three 250 mm square samples were constructed using the same manufacturing techniques outlined previously. Upon cure, the corresponding shape of each laminate was measured using a speckle photogrammetry system from Correlated Solutions [48]. Speckle photogrammetry is a technique used to obtain full-field surface measurements of a specimen in a non-intrusive manner. A white speckle pattern is applied to the dark surface of the laminate using spray paint and a stereo-pair of calibrated cameras is used to capture images of this pattern. A full three-dimensional map of the surface is then reconstructed in software from this pattern. The out-of-plane measurement accuracy of this technique is on the order of 4 μm with the entire 250 mm square laminate in view. Measurements were conducted with the laminates lying on a flat surface, and thus

susceptible to gravity effects.

Figure 3.12 displays the measured shapes of the 4-ply laminates. It is apparent that there are significant post-cure shape errors present. The errors are dominated by cylindrical modes oriented in the y-direction and have a peak-to-valley amplitude of approximately 6.0 mm (1.07 - 1.41 mm RMS). There is also a slight twisting mode associated with each sample.

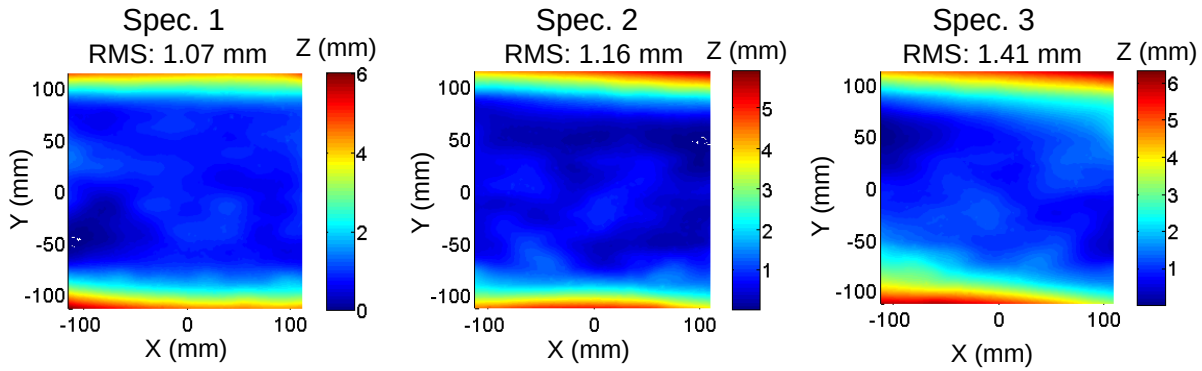

Figure 3.12: Measured shape errors of the three constructed laminates.

For comparative purposes, the level of measured imperfections were injected into the numerical model and shape error predictions were made. Table 3.4 displays the parameters used for the simulation. As the ply orientation and mean thickness variations were observed to be somewhat random, they were modeled using normal and uniform distributions, respectively.

Table 3.4: Imperfection magnitudes used for simulation comparison

Imperfection	Modeled Parameters
Ply Misalignment	$\Delta\theta_k \sim \mathbf{N}(0,\ 0.3^\circ)$
Ply Thickness Variation	$t_{top} - t_{bot} \sim \mathbf{U}(0,\ 1.3\ \mu\text{m})$
Through-Thickness Temperature Change	ΔT_z: 0.5°C

Figure 3.13 displays the calculated shape-error magnitudes resulting from the imperfections listed in Table 3.4. It is apparent that the model predicts dominating curvature terms oriented in the y-direction. A lower-magnitude twisting term is also evident for the results of Analysis 1 and 2. A higher amplitude of deformation is predicted in comparison to experiments with peak-to-valley deformations ranging from 6.8 - 8.1 mm (1.62 - 2.37 mm RMS). However, as the model did not account for gravity sag, this over-prediction is somewhat expected.

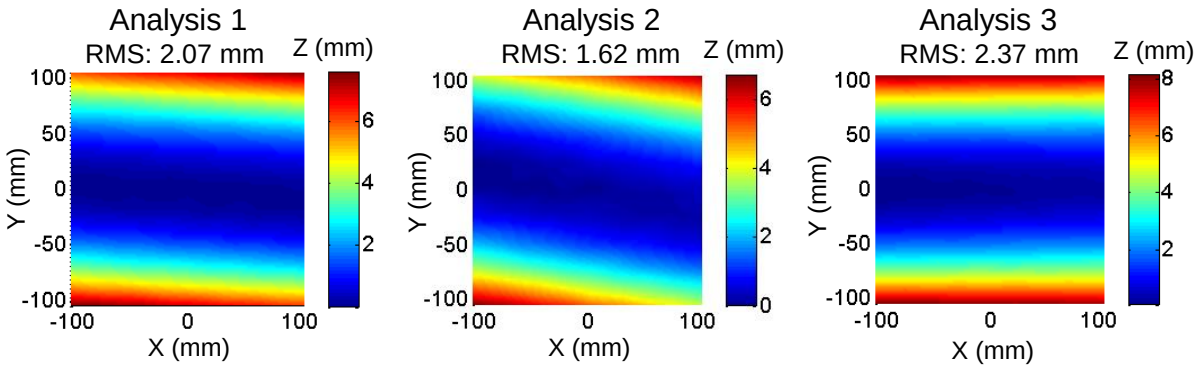

Figure 3.13: Calculated shape errors due to measured imperfection magnitudes.

3.3 Spatially-Varying Imperfections

The previous section considered imperfections that varied between plies but were constant across the entirety of a single ply. However, when visually inspecting the constructed laminates, spatially-varying shape errors are observed. Figure 3.14 is a photograph of one of the cured samples. Significant mid-spatial frequency shape errors are observed as the surface appears "rippled". Errors such as these are atypical for traditional composites and were not captured in the previous modeling efforts. Therefore, the purpose of this section is to quantify the level of mid-spatial frequency shape errors observed in the constructed laminates, identify and characterize the spatially-varying imperfections at the ply-level, and finally make predictions on their effect towards spatially-varying shape errors.

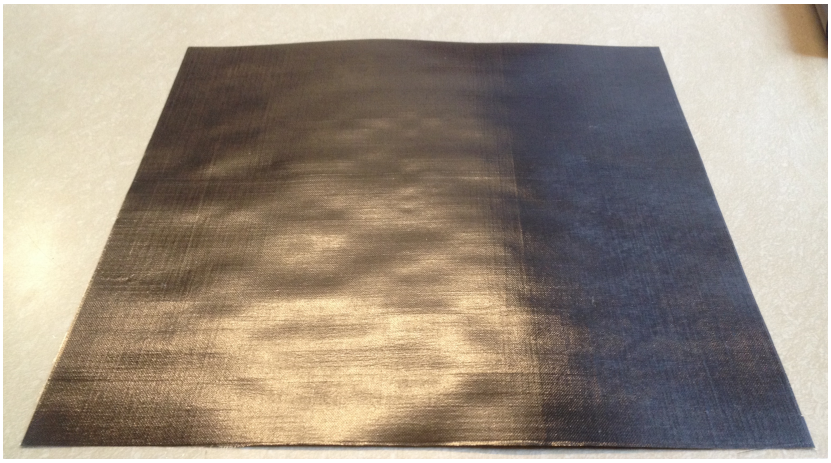

Figure 3.14: Post-cure shape error of a 4-ply $[0°/90°]_s$ laminate.

3.3.1 Shape Error Measurements (Mid Spatial Frequency)

The mid-spatial frequency errors are of much lower magnitude, and are therefore masked by the large-amplitude curvatures. In order to study these errors further, the measurements were filtered using a two-dimensional Fast-Fourier Transform (FFT) and high-pass Gaussian filter. The details of this process can be found in Appendix A. Figure 3.15 displays the filtered measurements using a pass frequency of $1/75$ mm^{-1}. This spatial frequency was chosen in order to eliminate the observed low-spatial errors. The mid-spatial rippling effect is now clearly evident for the laminates. These errors appear to exist over a number of length-scales, with wavelengths ranging from 10 - 75 mm. The mode of deformation is also observed to be slightly elongated in the x-direction.

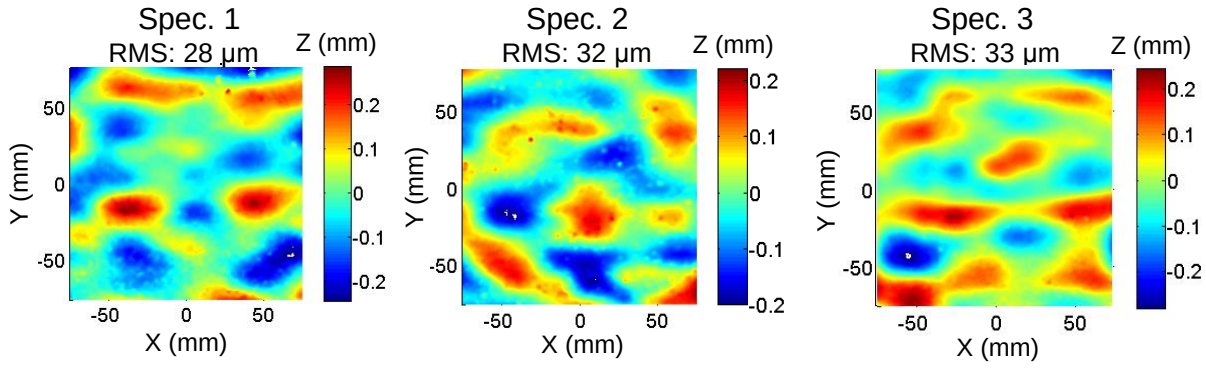

Figure 3.15: Measured mid-spatial frequency errors of the constructed laminates.

3.3.2 Sources of Imperfections

Two spatially varying imperfections are considered here: spatial variations in the thickness and spatial variations in the fiber orientation of each ply. It is believed that these imperfections arise due to the tow-spreading process required to manufacture the thin-ply material. In this process, nominally circular carbon fiber tows are spread to flat tapes and then butted together to form a prepreg tape of substantial width. The process is performed with the tows under tension in an attempt to keep them aligned. Through this process, the tows undergo a high-degree of spreading. For example, a 12K tow (12,000 fibers) containing 5 μm diameter fibers packed in a hexagonal arrangement at a volume fraction of 50% has an initial diameter of approximately 1.0 mm. Upon spreading to a 17gsm tape, and assuming no change in the packing structure or volume fraction, a 30-35 mm tape will be produced. This represents an extremely large increase in the width of each tow and therefore, deviations in this process are expected. Figure 3.16 displays two possible imperfections produced from the tow-spreading process. The first, depicted in Figure 3.16(a), is an incomplete spreading of the tows. Instead of a flat tape, a lobed structure is produced and therefore a variation in the thickness of each ply is expected. This variation is oriented perpendicular to the fiber direction only, with uniform thickness along

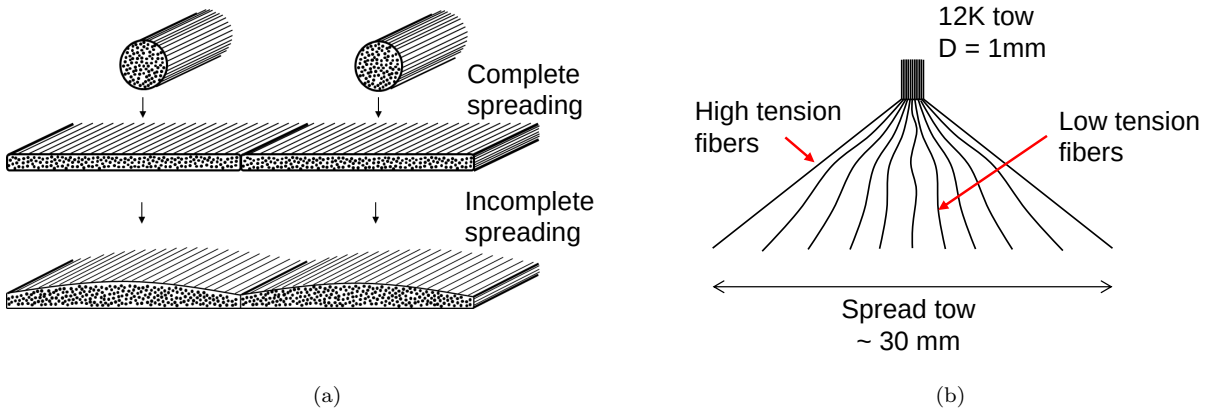

(a) (b)

Figure 3.16: Sources of spatially varying imperfections due to tow-spreading: a) thickness variations and b) fiber misalignments.

the fiber direction. The characteristic half-wavelength of this imperfection is expected to be on the order of the tow-width once spread ($\sim$ 30 mm). The second imperfection, depicted in Figure 3.16(b), is related to the directionality of the fibers. Due to the high-degree of spreading, a variation in tension is expected across the width of the tow. Fibers located at the edges of the spread tow will be subjected to higher levels of tension than fibers near the middle. If the overall level of tension is reduced the internal fibers will lose their directionality, potentially creating "fiber waviness" in the ply.

3.3.3 Imperfection Characterization

3.3.3.1 Ply Thickness

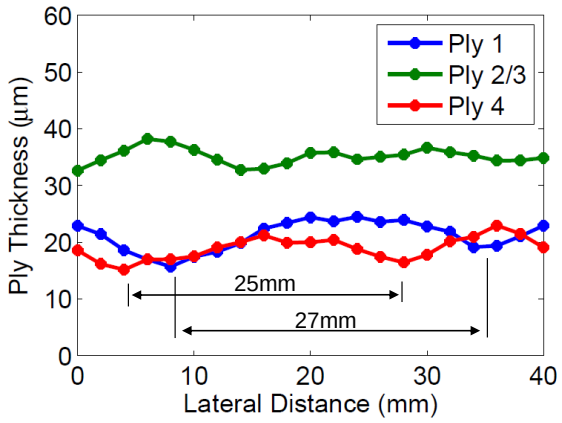

Figure 3.17: Thickness measurements performed using cross-sectional micrographs.

The variation in ply thickness was measured by studying the spatial distribution of the thickness measurements produced in Section 3.2.2.1. Figure 3.17 displays these measurements along the length of the

sample. From the measurements of Ply 1 and 4, it can be seen that there is evidence of a "lobed" variation in the ply thickness perpendicular to the fibers. The characteristic half-wavelength of this variation appears to be $\sim$ 25 - 27 mm in length. It is believed this is due to the incomplete tow-spreading mentioned above.

3.3.3.2 Fiber Misalignments

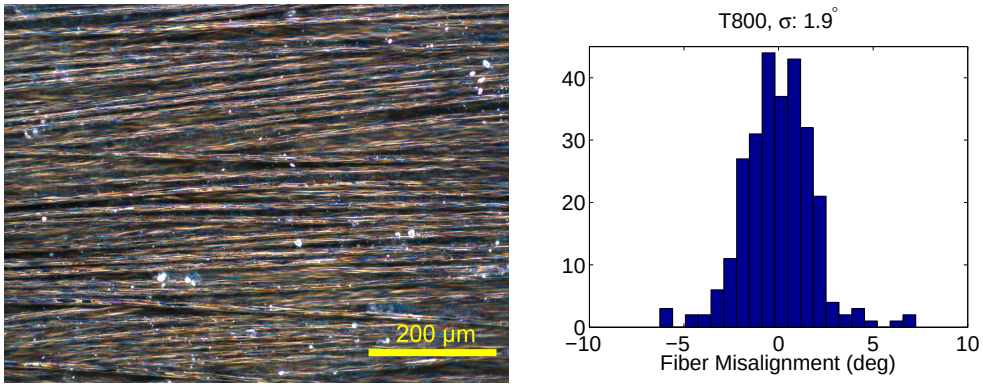

(a) (b)

Figure 3.18: a) In-plane image of terminal ply displaying significant variations in fiber direction. b) Measured fiber orientation distribution for the T800 material.

To quantify the level of fiber misalignment in the plies, the in-plane images of the fiber directions presented in Section 3.2.2.2 were used. Figure 3.18(a) displays one such image where significant variations in the direction of each fiber are observed. The distribution in measured fiber angles, shown in Figure 3.18(b), was used to quantify the level of fiber misalignment in each ply. A standard deviation of 1.9° was measured for the terminal ply and therefore significant fiber misalignments are present. The characteristic wavelength these misalignments was difficult to quantify, as it varied over many length scales. Oscillations between 2 and 50 mm were observed.

3.3.4 Numerical Modeling

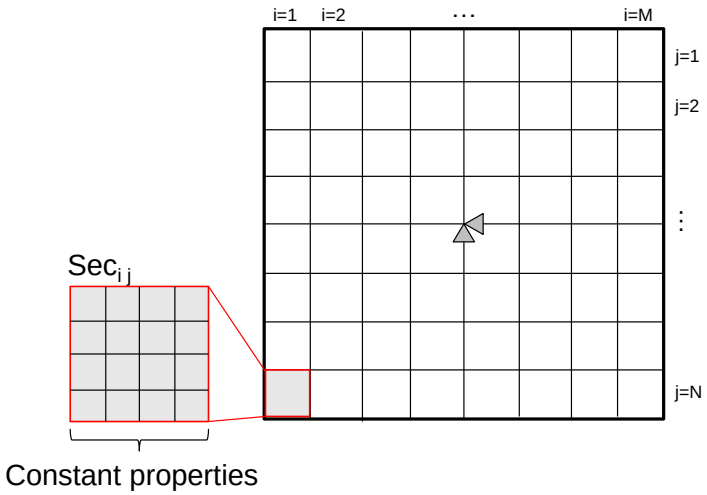

Figure 3.19: Schematic of numerical model used to model spatially-varying imperfections.

To model the spatially-varying imperfections, the numerical model presented in Section 3.2.3 was modified to allow for the definition of spatial variations in ply thickness and fiber orientation. This was performed through the definition of a regular grid across the plate, as shown in Figure 3.19. At each grid location, constant but unique section definitions are created, thus providing spatial control over the properties of each ply. For the current analysis, a grid size of 5 x 5 mm was used with 16 elements per grid. This resulted in 2,500 unique section definitions across the 250 mm square part.

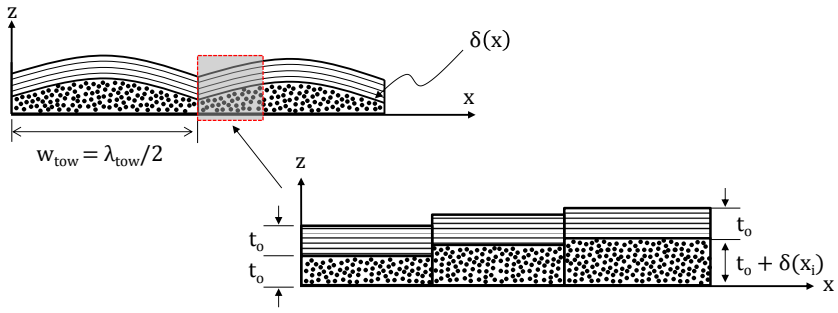

Figure 3.20: Schematic of method used to model ply thickness variation.

Figure 3.20 schematically depicts the method used to model the variation in ply thickness. To capture the lobed structure perpendicular to the fibers the variation in ply thickness, δ, was defined as an absolute value of a sinusoidal function. Therefore, for a ply with fibers oriented in the y-direction, the variation in thickness is defined as

$$\delta(x) = \delta_{max} |sin(\frac{2\pi\ x}{\lambda_{tow}})|, \tag{3.16}$$

where δ_{max} is the amplitude of thickness variation and λ_{tow} is the wavelength of variation. Using this formulation, and discretizing over the sections, the ply thickness at each ply can be defined as

$$t_{ij} = t_{ij}^{nom} + \delta_{ij}. \tag{3.17}$$

In this process it is assumed that the orthotropic material properties of the ply remain constant during the thickness change.

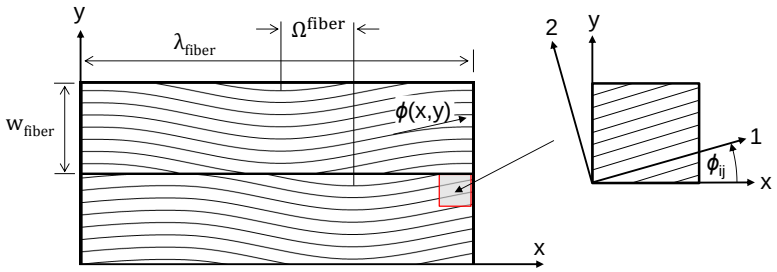

Figure 3.21: Schematic of method used to model fiber misalignment

Figure 3.21 depicts the method used to model the variation in fiber orientation within a ply. It is assumed that the fiber variation follows in a sinusoidal fashion with a wavelength λ_{fiber}. This variation is assumed to occur in discrete fiber bundles of width, w_{fiber}, phase-shifted by Ω^{fiber}. Therefore, the variation in fiber orientation of a ply with fibers nominally oriented in the x-direction can be described as

$$\phi(x) = \phi_{max} sin\big(\frac{2\pi\ x}{\lambda_{fiber}} + \Omega^{fiber}\big), \tag{3.18}$$

where Ω^{fiber} varies randomly for each bundle. Using this formulation, a unique fiber orientation can be described at each discrete section as follows:

$$\theta_{ij} = \theta_{nom} + \phi_{ij}. \tag{3.19}$$

3.3.4.1 Results

A parametric study was performed in order to assess the impact of the spatially-varying imperfections on the resulting shape deformation. For the ply thickness, variations in the terminal 0° plies and internal 90° plies were considered independently. The tow width, $w_{tow} = \lambda_{tow}/2$, was also considered. For the fiber orientation, the effect of wavelength, λ_{fiber}, and fiber bundle width, w_{fiber} were considered. The results of these studies are presented in Figures 3.22 and 3.23. The results are presented in terms of RMS surface error and are plotted for normalized RMS values of the variation. A surface plot of the resulting deformation from one trial is also shown.

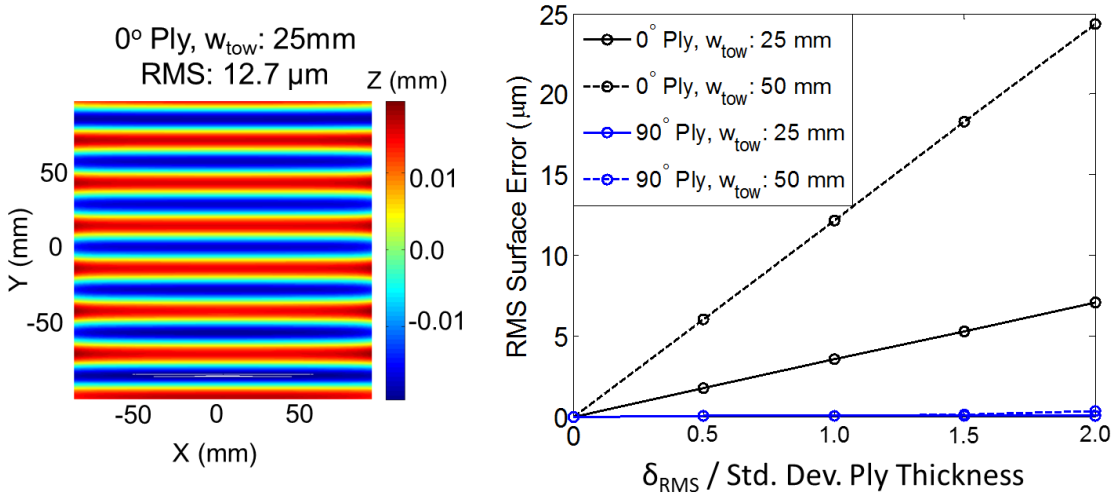

Figure 3.22: Shape error due to spatial variations in ply thickness.

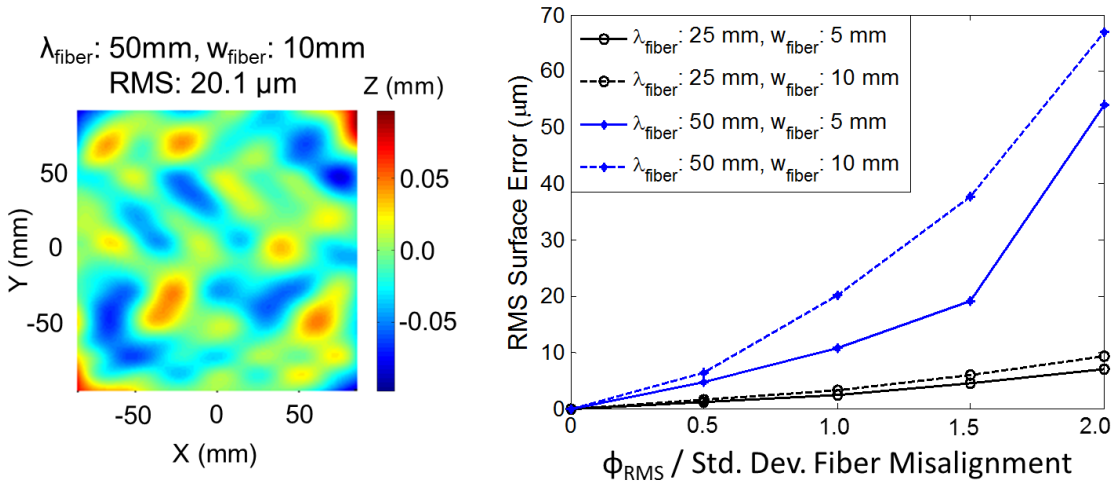

Figure 3.23: Shape error due to spatial variations in fiber orientation.

From the surface plot in Figure 3.22 it is apparent that oscillating deformations are predicted due to ply-thickness variations in the terminal 0° plies. The half-wavelength of variation corresponds directly to the tow width, w_{tow}. A strong relationship between the amplitude of shape error and tow width is also observed with a factor of ~ 3.5 increase observed between 25 mm and 50 mm wide tows. An approximate linear relationship between the amplitude of thickness variation and the corresponding shape error is predicted. Negligible deformations are associated with variations in the internal 90° plies. This is due to the fact that the laminate preserves its through-thickness symmetry in this case and therefore remains balanced with respect to the neutral axis.

From Figure 3.23 it is apparent that the shape errors due to fiber misalignments are more random in

nature. These errors exhibit a range of amplitudes and characteristic length scales. From the results of the parametric study, a strong dependence on the wavelength of variation, λ_{fiber}, and a weak dependence on bundle width, w_{fiber} is observed. Larger surface deformations are predicted for longer wavelength variations. A non-linear growth in the RMS shape error is also predicted as a function of increasing fiber variation amplitude.

3.3.4.2 Comparison to Experiments

A simulation containing the imperfection magnitudes measured in Section 3.3.3 was performed in order to compare the predicted shape errors with those measured in Section 3.3.1. Table 3.5 summarizes the model parameters used for this study. Estimates were made on the wavelength and bundle width for fiber misalignments, as these parameters were not characterized completely.

Table 3.5: Imperfection magnitudes used for experimental comparison

Imperfection	Modeled Parameters
Spatial Thickness Variation	δ_{max}: 2.3 μm, λ_{tow}: 50 mm (25 mm tow width)
Spatial Fiber Variation	ϕ_{max}: 1.9°, λ_{fiber}: 40 mm, w$_{fiber}$: 10 mm

Figure 3.24 displays the results of this study. It can be seen that the mode of predicted shape error is similar to those in the experiment. Mid-spatial frequency features with various amplitudes and wavelengths are produced. The errors appear to have a slight preferential direction oriented with the x-axis as in the experimental measurements. The predicted RMS shape error ranges from 25.5 - 27.3 μm in comparison to 26 - 33 μm experimentally. It is believed that the small discrepancies here are due to the choice of frequency for the variation in fiber orientation. However, the overall nature of the errors is comparable to those seen in practice. Table 3.6 summarizes the results obtained for this study.

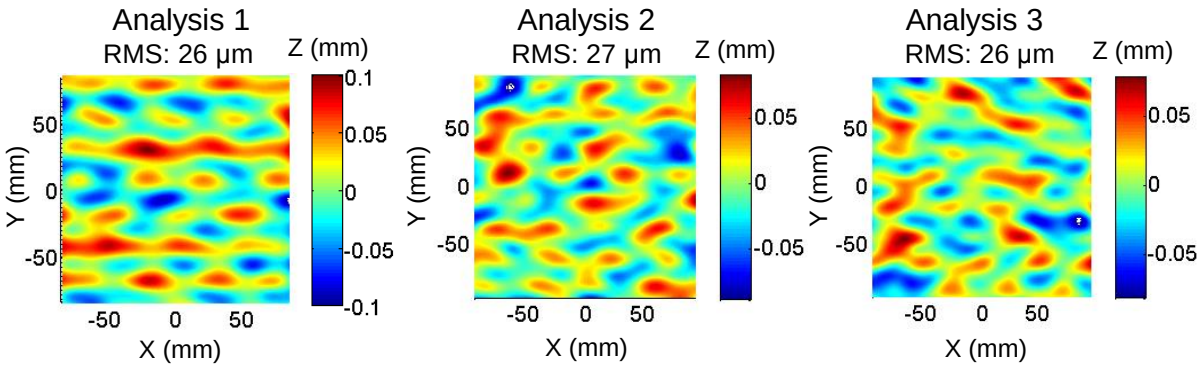

Figure 3.24: Predicted mid-spatial frequency shape errors due to measured imperfection magnitudes.

Table 3.6: Comparison of measured and calculated shape errors

	RMS (μm)
Analysis 1	25.5
Analysis 2	27.3
Analysis 3	26.3
Measurements (average)	30.3

3.3.5 Model Extensions

Using the model formulation above, several additional simulations can be performed in order to study the effect of the spatially-varying imperfections in various settings. Specifically, the effect of nominal ply thickness, curing temperature, and laminate orientation are considered here.

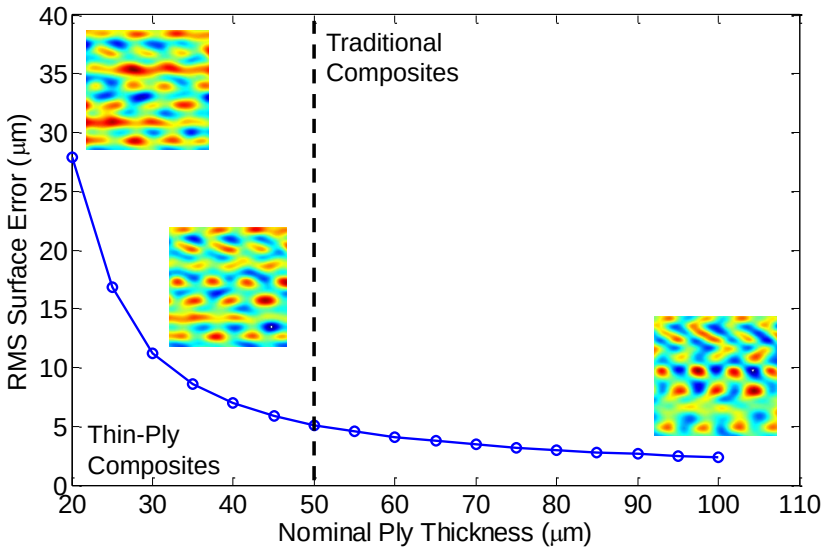

Figure 3.25: Shape error dependence on nominal ply thickness.

Figure 3.25 displays the effect of nominal ply thickness on the RMS shape error produced from spatially-varying imperfections. The level of imperfections are held fixed under the conditions presented in Table 3.5, and the nominal ply thickness is increased uniformly over each ply. From the results it is apparent that a significant reduction in RMS shape error is predicted as the ply thickness increases, particularly when considering the designated "thin-ply" regime (< 50 μm). Beyond this point, tending towards ply thicknesses associated with more traditional composite materials, very small magnitude shape errors are predicted (< 5 μm RMS). At this level, errors such as these would likely go unnoticed.

Surface plots of the shape deformations are also presented in Figure 3.25. The color-scale of these plots is scaled according to the associated RMS shape error. From these plots it is apparent that a mode change

in the shape error is also predicted. Initially elongated features appear to become more symmetric upon increase in the nominal ply thickness.

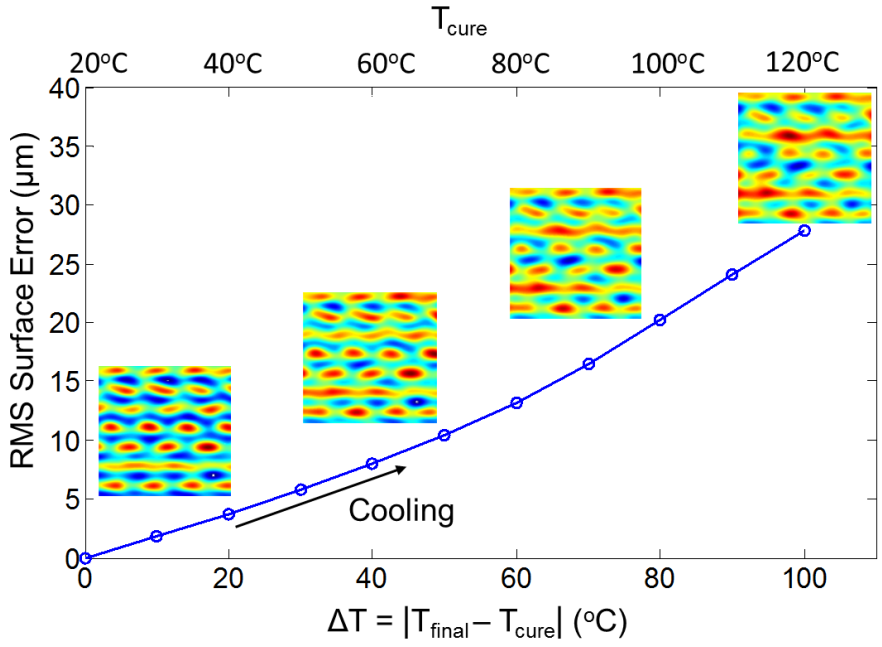

Figure 3.26: Shape error dependence on curing temperature.

Figure 3.26 studies the effect of cure temperature on the thermally-induced shape errors. This was performed by extracting results at various increments within the simulated cooling process. At increased cure temperatures, T_{cure}, the laminate will undergo a larger temperature change during cooling, ΔT. Therefore, increased magnitudes of thermal stresses will develop within the laminate, and thus larger shape errors are predicted to occur. This is evident in the trend within Figure 3.26. A slight increase in the progression of shape error is observed at a cure temperature of 80°C. From the surface plots, it appears that shape error also begins to change mode at this point. The fairly regular rippling pattern starts to become more random in nature as evident by the result obtained at $T_{cure} = 120°C$.

Finally, Figure 3.27 investigates the effect of laminate orientation on the magnitude and mode of imperfection-induced shape errors. Five different symmetric laminate orientations were considered, ranging from 4 to 8 plies in total. As expected, a significant reduction in the RMS shape error is predicted as a function of ply count. The 8-ply laminates exhibit only 3.5 μm of RMS shape error upon cure. The mode of deformation also appears to be dependent on the number of plies and laminate orientation. Characteristic features are observed parallel/normal to the direction of certain plies. For example, the $[45°/\text{-}45°]_s$ laminate has features oriented in the $\pm$ 45° directions while the $[0°/90°]_s$ contains features oriented with the laminate coordinate system (x and y). This effect is less pronounced for the higher ply-number laminates.

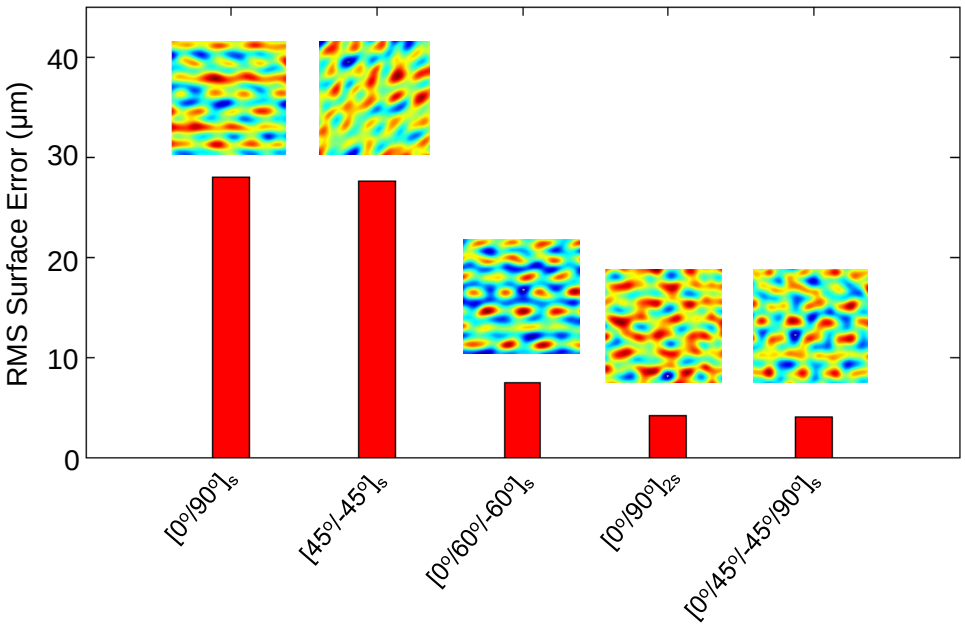

Figure 3.27: Shape error dependence on nominal laminate orientation.

3.4 Discussion of Results

Imperfections associated with nominally symmetric thin-ply composite laminates were studied. The study focused on 4-ply $[0°/90°]_s$ laminates with 20 μm thick plies. Two sets of imperfections were considered: 1) those that were constant in the plane of the laminate and 2) those that varied in the plane for each ply. For the first case, uniform variations in ply thickness, ply orientation and thermal gradients were considered. The magnitude of each imperfection was characterized in an experimental setting. The study determined that a mean thickness variation of 1.3 μm was observed between the top and bottom plies. A maximum ply misalignment of 0.3° was observed, and a 0.5°C through-thickness temperature difference was measured during cure. For many applications and for traditional composite parts, these imperfections would be considered negligible. However, due to the extremely thin nature of the material, imperfections such as these become significant as demonstrated through numerical simulations. The above imperfections were modeled independently and their effect on the post-cure shape error was determined. All imperfections resulted in constant-curvature shape errors. Through a parameter sensitivity analysis, the variation in ply thickness was found to be the dominant factor. Shape error magnitudes of $\sim$ 1.5 mm RMS were predicted for 250 mm square plates after injecting the measured imperfection value into the model. Therefore, if a reduction in global shape error is desired, the uniformity in ply thickness should be addressed.

The global shape error of three 250 mm square laminates was also measured experimentally. Consistent shape errors were observed between samples displaying dominating curvatures oriented in the y-direction. The magnitude of error ranged from 1.07 - 1.41 mm RMS. Relatively good agreement was observed between the measurements and model predictions in terms of deformation mode. However, due to the lack of gravity

effects, there was a discrepancy in magnitude with the model predicting 1.62 - 2.37 mm RMS.

Upon visual inspection of the three constructed laminates, spatially-varying shape errors were observed. To quantify these features, the shape error measurements were filtered using a high-pass Gaussian filter, revealing significant mid-spatial frequency errors on the order of 28 - 33 μm RMS. Therefore, the second study considered ply-level imperfections that varied within the plane of the material. Specifically, variations in ply thickness and fiber orientation were considered. Through optical characterization, the plies were observed to have a standard deviation of 2.3 μm in thickness perpendicular to the fiber direction. A characteristic wavelength in variation of approximately 25 - 27 mm was also observed. A 1.9° standard deviation in the fiber direction was measured optically. Large variations in the spatial frequency of this variation were observed with wavelengths on the order of 2 - 50 mm. The effect of these imperfections was also modeled numerically through unique spatially-varying section definitions. From the simulation results, ply thickness variations are predicted to cause shape errors that vary with the frequency of imperfection while misalignments in fiber orientation produced a more random pattern of shape error.

Finally, the effect of nominal ply thickness, curing temperature, and laminate orientation on post-cure shape errors was determined. A significant reduction in the magnitude of mid-spatial frequency error was predicted as a function of nominal ply thickness with near complete mitigation at ply thicknesses > 75 μm. A further reduction in shape error magnitude is also predicted for decreased curing temperatures due to the reduced level of thermal stress. Laminates of the same ply count but differing orientations saw no change in shape error; however, laminates with higher ply counts saw a large reduction. Changes in the mode of deformation were also observed for all cases, demonstrating the highly non-linear nature of the problem.

Chapter 4

Multi-Ply CFRP Laminates

4.1 Laminate Choice

The preceding chapter was concerned with shape errors inherent to laminates constructed from extremely thin material ($\sim 20\ \mu$m / ply) and reduced ply counts (i.e., 4-ply $[0°/\ 90°]_s$). It was shown that laminates such as these possess shape errors over a number of spatial-frequencies. However, for many practical applications, thicker laminates are desired as they possess a higher degree of isotropy and dimensional stability. The remainder of the thesis focuses on laminates constructed from 30 μm thick plies and higher ply-counts. Specifically, three laminates are considered consisting of 8, 16, and 32 plies. They are listed in Table 4.1.

All of the laminates are a combination of plies oriented in the 0°, 90° or ±45° directions. However, the stacking sequence determines the mechanical response of the laminates. Two variants of the 16 and 32-ply laminates are presented: a and b. For example, Laminate 2a is defined by stacking two layers of the 8-ply laminate orientation on top of each other. Laminate 2b differs from 2a in that the second 8-ply layer is rotated 90° with respect to the first. Laminates 3a and 3b are constructed in the same manner; however, four layers are implemented.

Appendix B, lists the ABD stiffness matrix of each of these laminates. It is apparent that the **B** matrix is null for all 5 orientations. Therefore, while not symmetric, Laminates 2b and 3b exhibit zero coupling between in-plane loads and out-of-plane curvatures. Figure 4.1 displays the in-plane stiffness (A11) and bending stiffness (D11) at varying orientations with respect to the laminate coordinate system. Both of the stiffness components are normalized by their maximum values. All laminates possess in-plane isotropy as A11

Table 4.1: Considered CFRP laminate orientations

Laminate ID	Ply-Count	Laminate Orientation
1	8	$[0°/+45°/\text{-}45°/90°]_s$
2a	16	$[0°/+45°/\text{-}45°/90°]_{2s}$
2b	16	$[0°/+45°/\text{-}45°/90°]_s$ + $[90°/\text{-}45°/+45°/0°]_s$
3a	32	$[0°/+45°/\text{-}45°/90°]_{4s}$
3b	32	$\left[[0°/+45°/\text{-}45°/90°]_s + [90°/\text{-}45°/+45°/0°]_s\right]_2$

Table 4.2: Reduction in laminate bending stiffness

Laminate ID	$D11_{min}$ / $D11_{max}$	Orientation (deg)
1	0.186	65.0
2a	0.687	77.5
2b	0.972	45.0
3a	0.911	77.5
3b	0.993	45.0

is independent of orientation. However, the out-of-plane properties are shown to vary significantly between laminate orientations. The magnitude and orientation of the maximum reduction in bending stiffness is summarized in Table 4.2. A large variation is observed for Laminate 1 as the bending stiffness is reduced by a factor of 0.186 at an orientation of 65.0°.

A more notable comparison is made between Laminates 2a and 2b. Although the same number of plies are contained within the laminate, Laminate 2b displays a higher degree of isotropy with respect to bending stiffness. An improvement in bending stiffness reduction from 0.687 to 0.972 is realized. The same is true when comparing the bending stiffness of Laminates 3a and 3b, where comparative reduction factors of 0.911 to 0.993 are observed. For many applications this increased level of isotropy is desired, as the response of the laminate is no longer dependent on the orientation of applied loads. Therefore, laminates 2b and 3b are implemented for the thesis and are referred to as the "16-ply" and "32-ply" laminates for simplicity. This result demonstrates the utility of using thin-ply material. 16 and 32-ply laminates can be constructed with near complete isotropy while keeping the thickness to 480 and 960 μm, respectively. This would not be achievable with conventional composites.

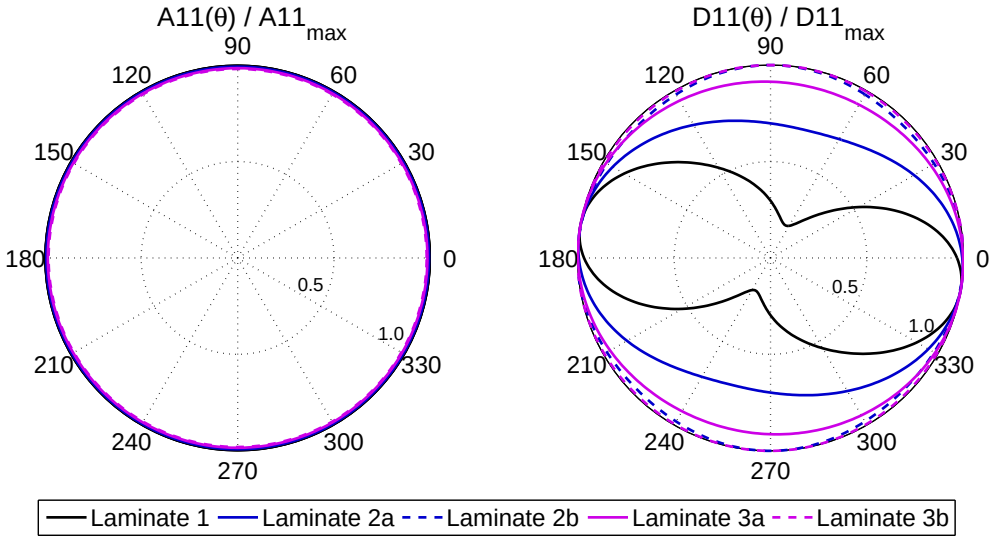

Figure 4.1: Normailized in-plane (A11) and bending (D11) stiffness at various orientations.

.

4.1.1 Measured Shape Errors

Figure 4.2 compares the measured post-cure shape errors of three substrates having 8, 16, and 32-ply laminate orientations. Nominally spherical laminates constructed on a curved mandrel with a 2.0 m radius of curvature (ROC) are considered. In this study shape error is defined as the shape of the substrate after removal of its base spherical curvature. From the measurements it is apparent that the shape error mode is a saddle shape for all three laminates. This characteristic shape is known as astigmatism and will thus be referred to as such for the remainder of the thesis. The orientation of the astigmatic error is similar for the 16 and 32-ply laminates, as they have similar laminate orientations. A large decrease in the error magnitude is observed for the thicker laminates due to the significantly increased bending stiffness.

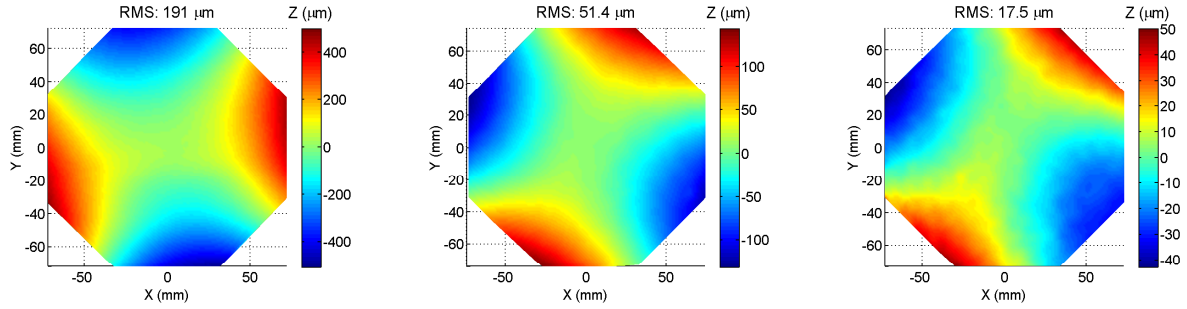

(a) (b) (c)

Figure 4.2: Measured shape errors for a) 8-ply, b) 16-ply, and c) 32-ply laminates

.

4.2 Reduction of Shape Errors

This section outlines two methods implemented in order to reduce the level of post-cure shape errors. First, a long-duration low-temperature cure cycle was implemented, leading to an overall reduction in thermal stresses within the cured parts. Second, a deformable mandrel was constructed, allowing for adjustments to be made in the shape of the curing surface. For simplicity, results are shown for 16-ply laminates only.

4.2.1 Low-Temperature Cure Cycle

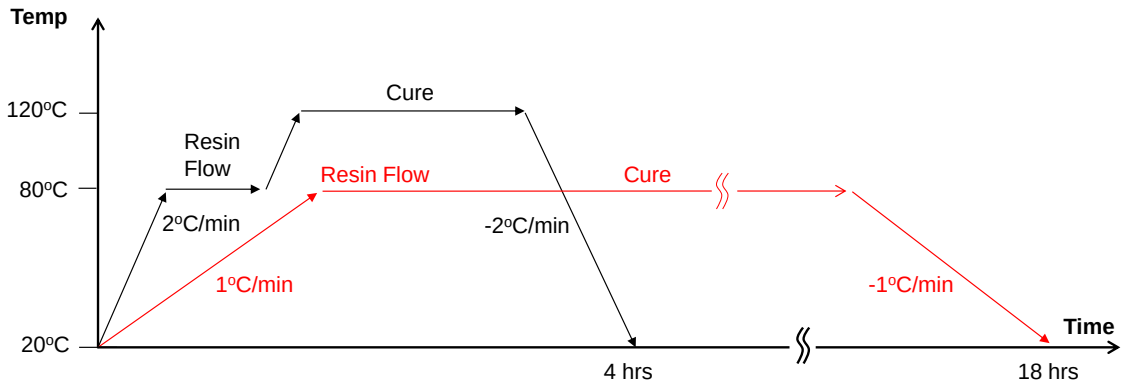

Figure 4.3: Autoclave cure cycle displaying nominal (black) and low-temperature (red) profiles.

The cure cycles implemented for the CFRP laminates are shown in Figure 4.3. Two profiles are displayed: the nominal cure cycle (black) and long-duration, low-temperature cure cycle (red). In the nominal cure cycle, the laminate is cured at a temperature of 120°C for 2 hours. An intermediate "resin-flow" step at 80°C is also implemented for 30 minutes in order to ensure the part conforms to the surface of the underlying mandrel before the curing process starts. Loading/unloading rates are performed at ±2°C/min.

In the long-duration, low-temperature profile, the part is cured at a temperature of 80°C and held for 16 hours. The longer duration is required in order to ensure a full cure of the epoxy resin. Loading/unloading rates are also lowered to ±1°C/min. By performing the cure at a lower-temperature and thus subjecting the parts to a decreased level of cooling upon cure, a reduction in thermal stresses will be realized.

Table 4.3: Measured RMS shape error for 16-ply laminates.

Cure Temperature (°C)	Spec. 1 (μm)	Spec. 2 (μm)	Spec. 3 (μm)	Average (μm)
120	49.2	51.2	49.7	**50.0**
80	30.6	32.8	38.7	**34.0**

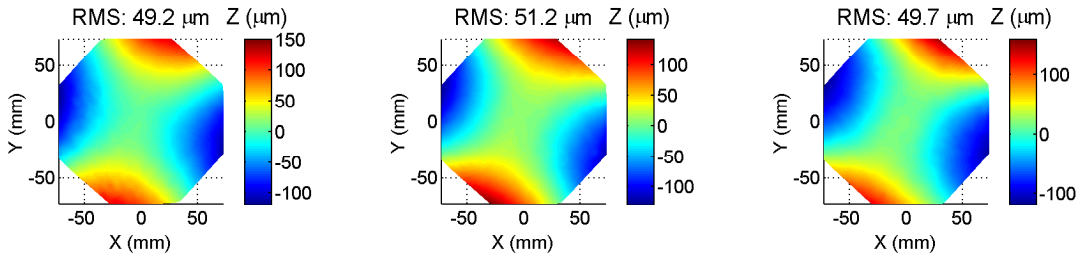

(a)

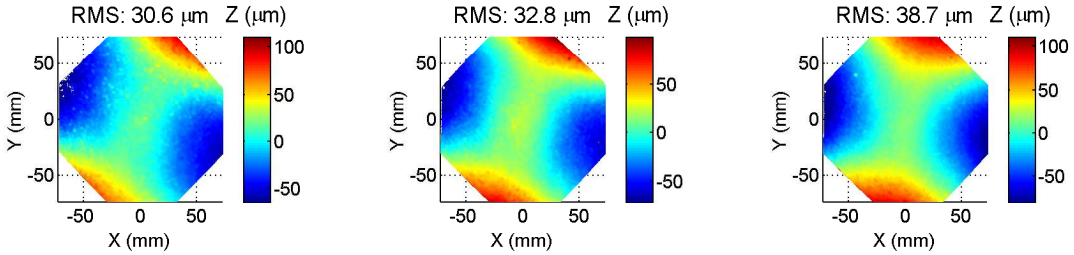

(b)

Figure 4.4: Measured shape errors for 16-ply substrates using a) the nominal and b) the low-temperature cure cycle.

Figure 4.4 compares the shape deformation of 16-ply laminates processed using the nominal and low-temperature cure cycles. It is apparent that the mode of deformation remains constant for laminates cured under both profiles. However, the magnitude of measured shape error is reduced for the laminates cured under the low-temperature cure profile. Table 4.3 summarizes the RMS shape error for the constructed laminates. An average value of 34.0 μm RMS was observed for the laminates cured at 80°C in comparison to 50 μm for those cured at 120°C. This represents a 32% reduction in post-cure shape error.

The advantages of using the low-temperature cure profile are evident from the reduction in measured shape errors. However, issues related to the thermal properties of the parts are of concern. Specifically, it is well-known that the glass-transition temperature, T_g, of epoxy is dependent on the curing temperature [49]. With a decrease in cure temperature, a proportional decrease in T_g is expected. For many applications this is of great importance as large operating temperature ranges are expected. A method to increase the T_g is to perform a post-cure thermal cycle at an elevated temperature. As the part is cured before this process, increase levels of thermal deformations should not be realized. However, for the present study all subsequent manufacturing processes and characterization experiments were performed at room-temperature. Therefore,

the thermal properties of the laminate were not of immediate concern.

4.2.2 Deformable Mandrel Surface

The second method used to reduce the magnitude of shape errors is to make changes to the shape of the mandrel and thus the surface to which the CFRP substrates are cured upon. With this technique, the shape of the substrate in the "zero" stress state will be modified. With knowledge of the expected magnitude and mode of deformation experienced by the substrates during cooling, the proper adjustment to the mandrel shape can be determined in order to uniquely define the final shape of the CFRP substrate.

4.2.2.1 Problem Definition

The problem can be defined as follows: a laminate constructed from multiple plies of UD CFRP prepreg is laid upon a mandrel. The shape of this mandrel can be parametrized by a height map over its surface, $w^o_{mandrel}(x,\ y)$. Through the curing process it is intended that the CFRP substrate replicate the shape of this mandrel, i.e.,

$$w^o_{CFRP}(x,y) = w^o_{mandrel}(x,y). \tag{4.1}$$

However, upon cure and release from the mandrel, shape errors in the CFRP substrate, defined as deviations from the spherical mandrel shape, are observed. These shape errors arise due to a number of factors associated with imperfections in the ply uniformity, lamination conditions and curing conditions, as outlined in the previous chapters. The actual shape of the substrate is therefore observed to be

$$w_{CFRP}(x,y) = w^o_{CFRP}(x,y) + w_{error}(x,y). \tag{4.2}$$

From Equation 4.1, it is apparent that modifications to the original shape of the mandrel, $w^o_{mandrel}(x,\ y)$, will result in changes to the cured substrate, $w_{CFRP}(x,\ y)$. If it is assumed that 1) the nature of the substrate shape error, $w_{error}(x,\ y)$, is inherent to the substrate alone and therefore independent of the mandrel shape, $w_{mandrel}(x,\ y)$, 2) $w_{error}(x,\ y)$ is systematic in both magnitude and mode across multiple cures of independent substrates, and 3) the entire process is geometrically linear in nature, the shape of the mandrel can be tuned to produce a desired final shape of the CFRP substrate. If the desired result is to have the shape of the CFRP substrate match that of the original mandrel surface, $w^o_{mandrel}(x,\ y)$, the optimal modification to the mandrel surface takes the form of $w_{error}(x,\ y)$ but of opposite sign. Therefore, the new mandrel shape is defined to be

$$w^{adj}_{mandrel}(x,y) = w^o_{mandrel}(x,y) - w_{error}(x,y). \tag{4.3}$$

This process is schematically depicted in Figure 4.5.

This formulation is somewhat limited by the assumptions presented above. While systematic shape errors

do exist, it has been shown that significant random variations are present as well (see Chapter 3). Through the construction of multiple nominally identical substrates, variations in the magnitude and mode of shape errors are observed. Therefore it is impossible to exactly tune the shape of the mandrel in order to fully null out the post-cure shape errors. However, if through the construction of multiple laminates predictable shape errors are observed, it stands to reason that beneficial corrections to the shape of the CFRP substrates will be made.

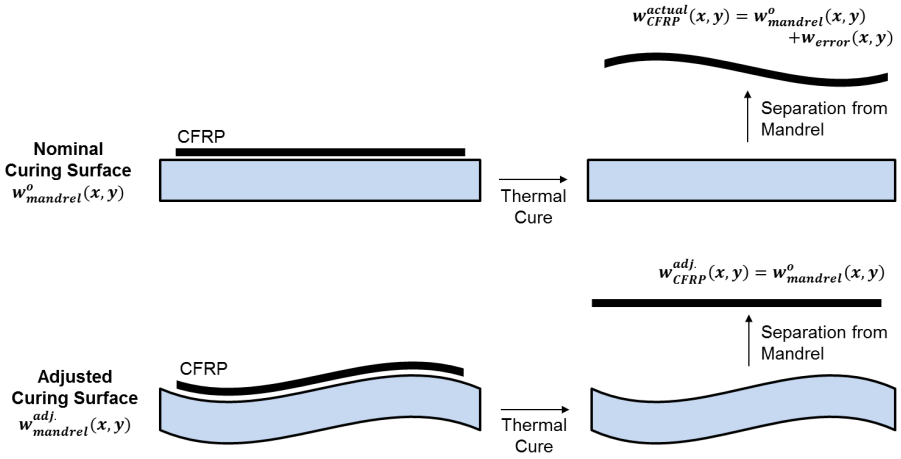

Figure 4.5: Schematic of deformable mandrel concept.

4.2.2.2 Measurements of Nominal Shape Errors

The three substrates cured using the low-temperature, long-duration cure cycle were used as a control study for this analysis. Figure 4.6 displays these measurements over a radius of 70 mm. The base shape, shape upon removal of the base sphere, and shape upon removal of the base sphere and total astigmatism is shown for each substrate. From the measurement of the base shape it is evident that the substrates replicated the base curvature of mandrel, producing a nominally spherical substrates. However, a slight increase in radius of curvature was observed for the substrates with a mean ROC of 2.08 m.

From Figure 4.6 row 2 it is apparent that the dominating form of shape error is astigmatic in nature. It is also evident that the magnitude and orientation of the astigmatic mode is relatively consistent across each substrate. A mean amplitude of 29.4 μm RMS at an orientation of -20° from the x-axis is observed. Finally, by removing both the base sphere and astigmatism terms from the measurements, it can be seen that there is a small amount of residual error present. The error appears to be dominated by a higher-order axisymmetric mode.

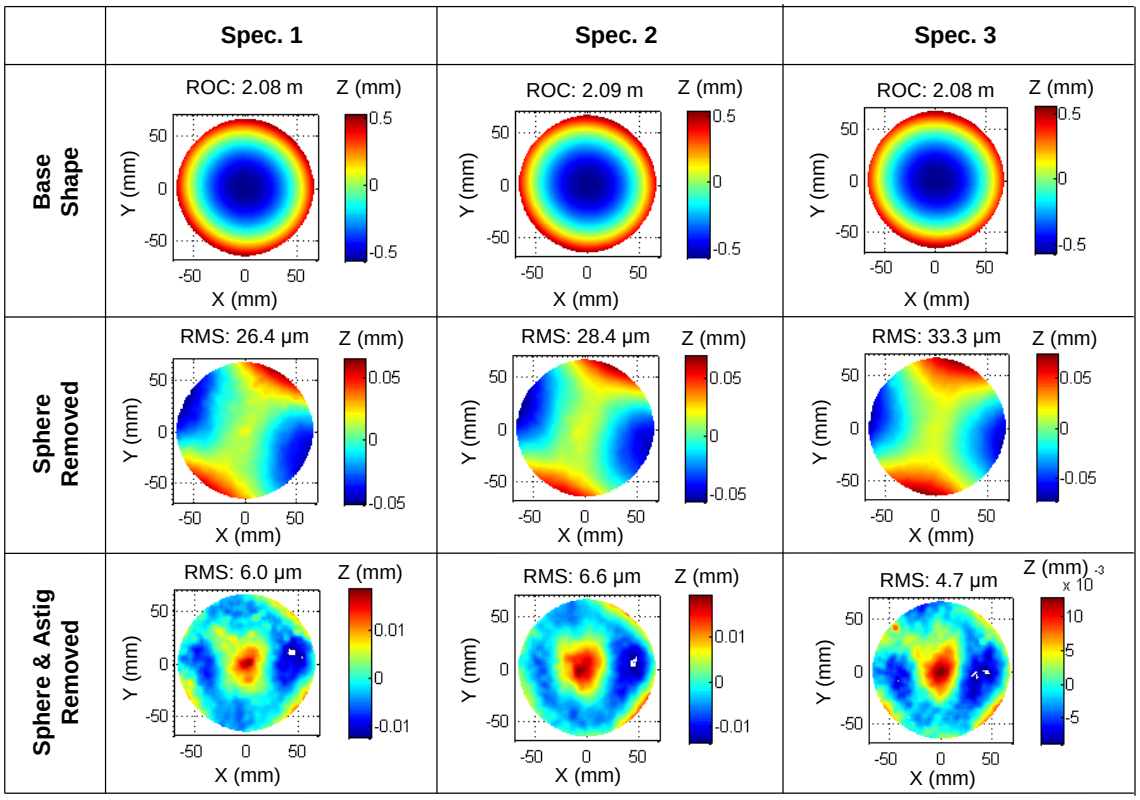

Figure 4.6: Shape measurements of CFRP substrates cured atop mandrel with zero imposed actuation.

4.2.2.3 Description of Deformable Mandrel Apparatus

As the dominating mode of shape error for the CFRP substrates was found to be astigmatic in nature, it stands to reason that the majority of shape correction can be achieved by producing a mandrel that can take on such a shape in addition to its base spherical curvature. Astigmatism-based deformations of a nominally flat plate can be introduced by prescribing normal displacements of two nodes relative to two others. Therefore, a mandrel implementing this simple design was constructed. Figure 4.7 is a CAD model of the deformable mandrel assembly with a picture of the manufactured apparatus in Figure 4.8.

The assembly consists of two main parts: the deformable plate and the base plate. The central region of the deformable plate was machined to have a convex, spherical surface with a 2.0 m nominal radius of curvature. This is the surface on which the CFRP substrate will be cured. In order to impose the intended astigmatic deformation the deformable plate is attached to the base plate at four points, two of which contain adjusting bolts while the other two contain ball joints. The adjusting bolts allow for prescribed deformations to be imposed at their respective locations. The ball joints, comprised of a steel ball bearing and four hardened cylindrical rods, provide a means to react the imposed loads from the bolts. Vacuum ports are integrated directly into the plate using cross-drilled holes. This is of utmost importance as it allows the large differential pressure associated with autoclave curing to be applied through the thickness of the deformable

plate instead of the entire assembly as a whole. If this was not the case, the pressure introduced during cure would impose further unwanted deformations to the surface of the mandrel during the cure of the CFRP substrate.

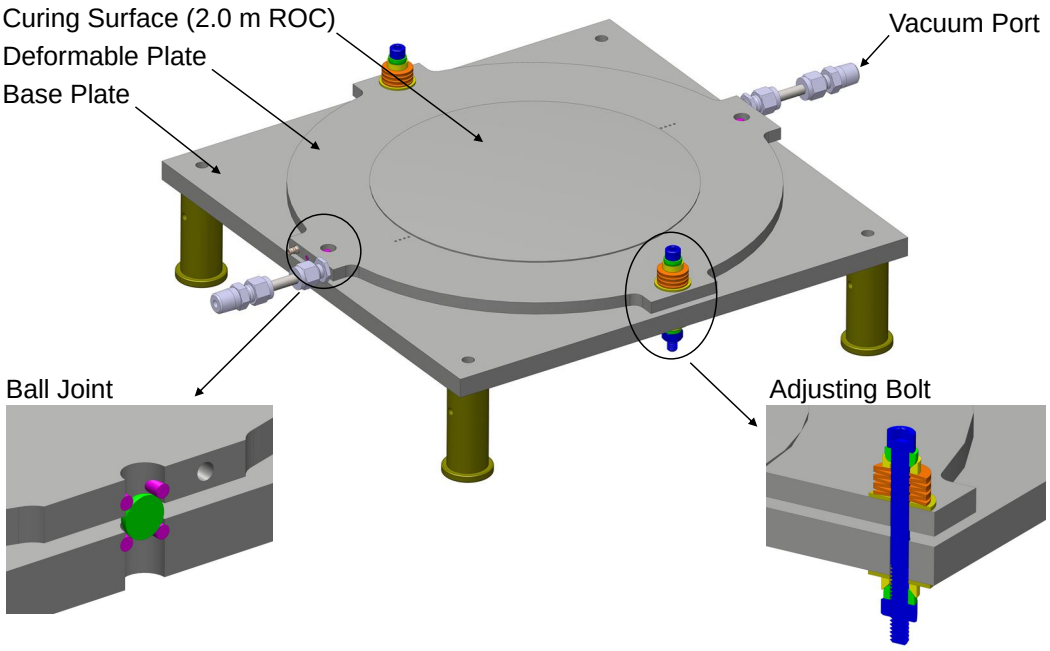

Figure 4.7: CAD schematic of deformable mandrel

4.2.2.4 Verification of Mandrel Deformation

In order to determine the accuracy to which the mandrel could take on astigmatism-based modes, the shape of the deformable mandrel was measured at various levels of deformation using speckle photogrammetry. The adjusting bolts were gradually tightened while continually monitoring the surface shape. Figure 4.9 displays the measured shapes decomposed into spherical, total astigmatism, and residual modes at three levels of actuation.

From the measurement of the base shape it is apparent that the as-manufactured shape of the mandrel is dominated by spherical curvature. However, there is a small component of initial astigmatism as well as higher order modes at 3.8 μm and 3.1 μm RMS, respectively. These are attributed to errors in the manufacturing process. Upon deformation of the plate several observations can be made. Firstly, the base curvature of the mandrel remains unchanged as evident by the fact that the magnitude of spherical curvature remains constant. This is ideal, as it is desired to keep the base curvature of the CFRP substrate constant. It is also apparent that the dominant mode of actuation is in the form of the intended astigmatism mode,

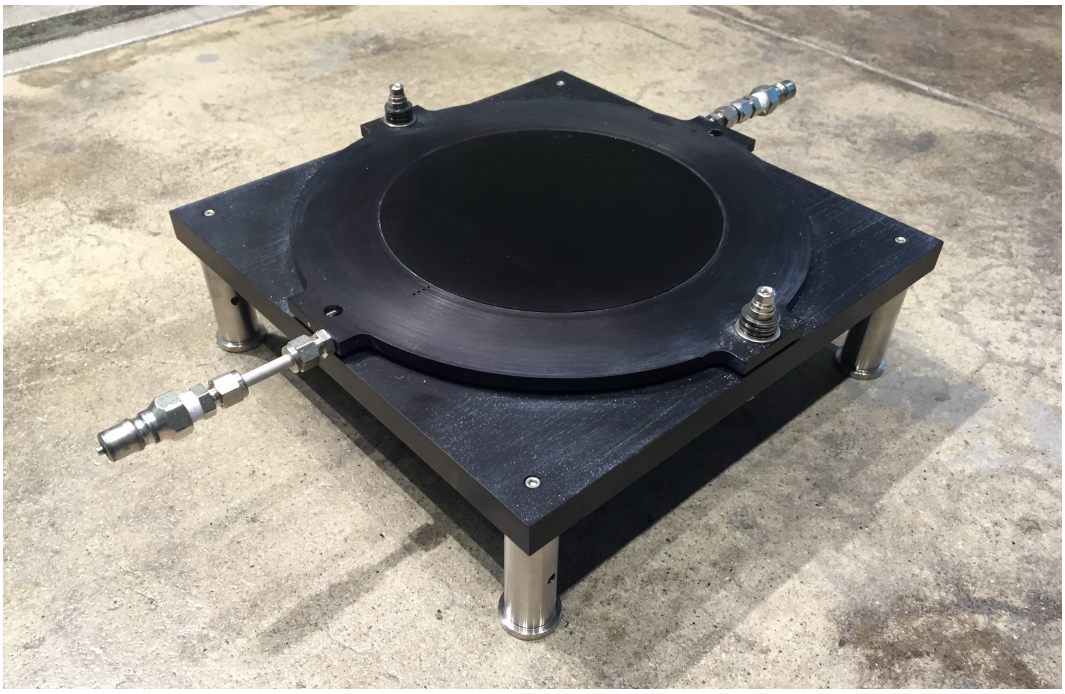

Figure 4.8: Fabricated deformable mandrel.

as the magnitude of residual shape error does not increase. This is again ideal, as higher-order modes of deformation will not be introduced during the replication process.

4.2.2.5 Shape Correction

An overview of the shape-correction procedure is as follows: using the adjusting screws, the required level of astigmatic deformation is imposed onto the surface of the mandrel. The level of deformation is verified throughout this step using the speckle photogrammetry system. An uncured laminate, nominally identical to those constructed for the control study, is then placed upon the curing surface of the mandrel. The orientation of this laminate is adjusted such that the principal axes of predicted astigmatism is aligned with that of the mandrel, but in opposite sign (i.e., matching "high" with "low" as shown in Figure 4.10). The laminate is then vacuum bagged and cured under autoclave conditions using the cure schedule outlined above.

Using the information from the three control measurements, 30 μm of astigmatism was imposed onto the mandrel surface and the laminates were oriented at -20° with respect to the principal axis of mandrel astigmatism. Two substrates were cured under these conditions and their measured shapes are presented in Figure 4.11. It is clear that while there was not complete mitigation of the astigmatism-based errors, a significant reduction in magnitude was achieved while maintaining a constant base curvature. The residual component of astigmatism is also now oriented almost completely with the laminate coordinate system (x/y) for both of the laminates. This incomplete mitigation is attributed to the non-systematic imperfections

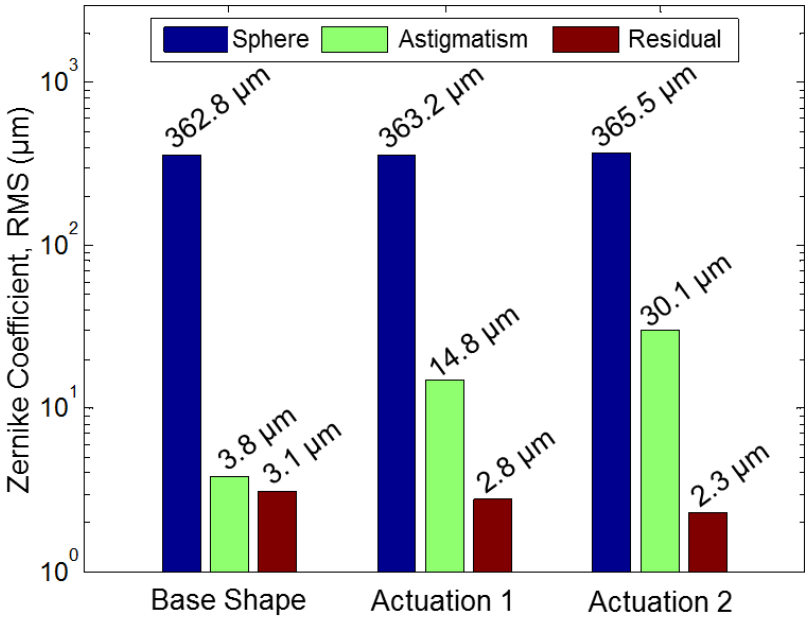

Figure 4.9: Zernike coefficients of deformable mandrel shape at various levels of actuation.

inherent to CFRP laminates. Misalignment of the laminate with respect to the principal axes of mandrel astigmatism may also be a factor. The higher-order axisymmetric mode of shape error appears to persist throughout this process, as evident by the last row in Figure 4.11.

4.3 Discussion of Results

8, 16, and 32-ply CFRP laminates were considered for the mirror substrates with two variant orientations for the 16 and 32-ply designs. All laminates possess isotropy with respect to their in-plane stiffness; however, the bending stiffness of each was determined to be highly dependent on the laminate orientation. Near complete isotropy was demonstrated for certain 16 and 32-ply laminates (2b and 3b, respectively) due slight modifications in the laminate orientations. This is highly advantageous for the current effort, as a near isotropic response will be achieved when incorporating the actuation capabilities into the mirror.

All three laminates displayed significant levels of a post-cure shape errors with a strong dependence on ply count. Two methods were implemented in order to reduce the magnitude of these errors. First, a low-temperature long-duration cure cycle was used to lower the overall level of thermal stresses within the parts. Second, a deformable mandrel was implemented in order to bias the surface to which the substrates are cured. The mandrel was able to take on astigmatic shapes on top of its base curvature. Therefore, by aligning the substrate and its expected level of astigmatic deformation with that of the imposed mandrel deformation, a reduction in the post-cure shape error was achieved. Both of these processes were performed

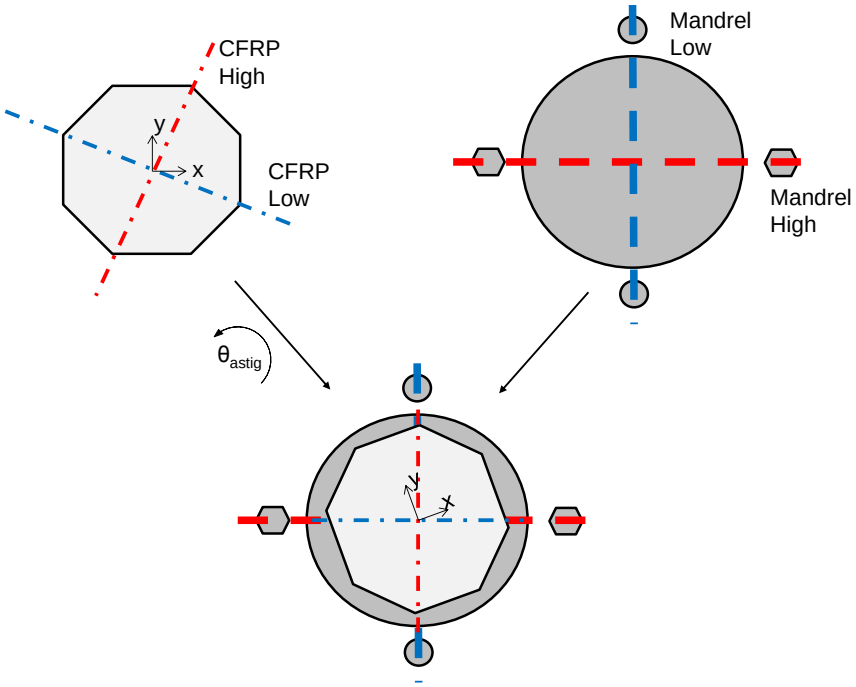

Figure 4.10: Alignment of principal axes of astigmatism between the CFRP substrate and deformable mandrel.

for 16-ply laminates, ultimately reducing the magnitude of substrate shape error from 50 μm down to 16 μm RMS.

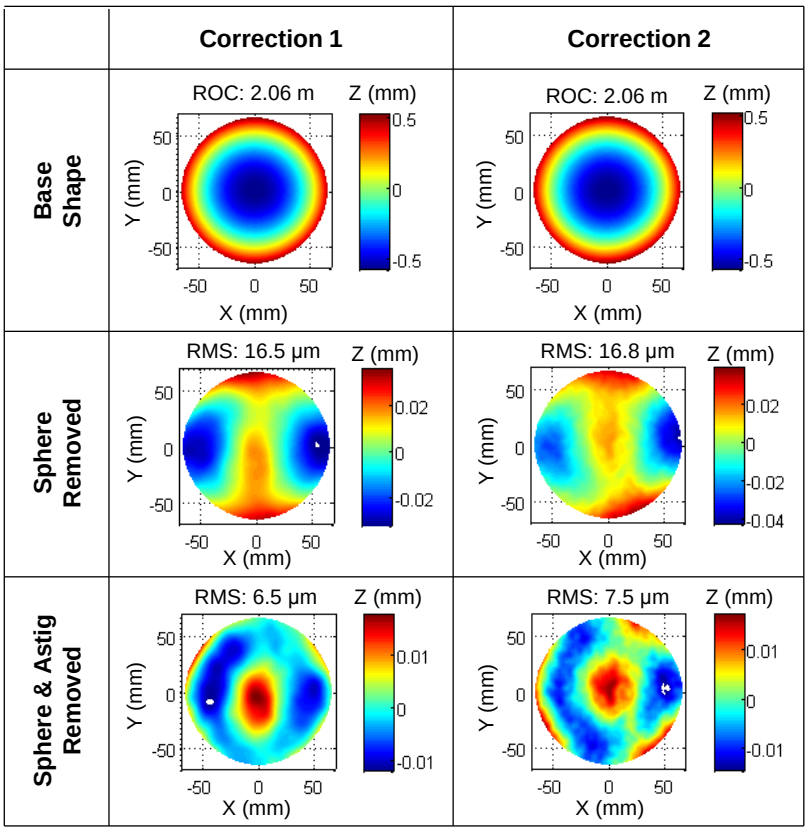

Figure 4.11: Shape measurements of CFRP substrates cured atop mandrel with deformation imposed.

Chapter 5

Nanolaminate Bonding

This chapter studies the deformation induced by bonding the nanolaminate facesheet onto the front surface of the CFRP substrate. This process proved difficult due to the relatively high flexibility of the CFRP substrate. Empirically determined methods of obtaining a uniform bond-line without distorting the CFRP substrate are outlined. A preliminary verification of the nanolaminate geometry through experimental measurements is also performed.

5.1 Overview of Nanolaminates

Nanolaminates are high-quality metal films constructed using sputter deposition techniques. The process has been developed and refined by Lawrence Livermore National Laboratories (LLNL). Multiple materials are implemented in the foil, each serving a specific function. A thin layer of gold is first deposited providing the terminal reflective surface. Subsequent layers of copper and zirconium are then sputtered in a periodic fashion providing the overall structure of the foil. For the present study these layers are repeated until a 50 μm thick film is produced. The final layer of the laminate is zirconium as it displays relatively good adhesion properties for subsequent bonding processes. Figure 5.1 is a picture of a 50 μm thick NL after deposition on a 2.0 m ROC spherical glass mandrel.

The purpose of the nanolaminate is to provide a low-roughness surface on the front of the CFRP substrate. This is performed through a bonding process where the nanolaminate is transfered from the mandrel to the CFRP substrate. However, it is important that the overall figure of the part does not degrade during this process. The post-bonded figure accuracy is dependent on two main factors: 1) the as-deposited stress state of the nanolaminate on the mandrel and 2) the stress induced during the bonding process. The following sections study these two factors in more detail.

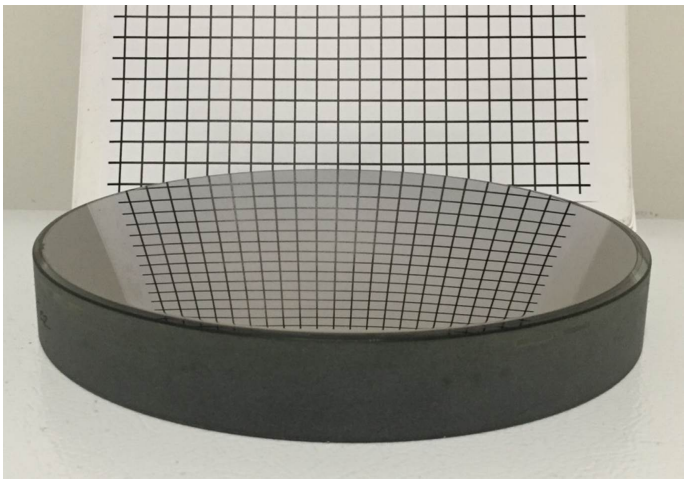

Figure 5.1: 250 mm diameter nanolaminate deposited on a polished 2.0 m ROC spherical mandrel.

5.2 Measurement of Free-Standing Nanolaminate

It is of utmost importance that the nanolaminate contain very low levels of as-deposited stresses. If such stresses are present, they will act to distort the mirror upon bonding and release from the mandrel. A traditional method of inferring stress in deposited thin-films is through curvature measurements of a carrier substrate, often a silicon wafer. By measuring the wafer curvature before and after deposition, the film stress can be determined using Stoney's formula [50]. However, in the case of nanolaminates, the deposition occurs on a thick ($\sim$ 1") glass mandrel and thus curvature changes cannot be practically measured (Note: a test wafer was incorporated into the chamber during each nanolaminate depositio;, however, possible differences in the deposition on glass vs. silicon warranted further investigations).

The method used here was to delaminate the nanolaminate from its mandrel leaving a free-standing structure and perform direct surface measurements of the film shape. Specifically, the Gaussian curvature of the free-standing film is measured. Gaussian curvature is a mathematical parameter used to describe shell structures of specific curvatures. It is defined as the product of the principal curvatures, κ_1 and κ_2:

$$\mathbf{K} = \kappa_1 \kappa_2 \tag{5.1}$$

where

$$\kappa_{1,2} = \frac{\kappa_x + \kappa_y}{2} \pm \sqrt{\frac{(\kappa_x - \kappa_y)^2}{2} + \kappa_{xy}^2} \tag{5.2}$$

and κ_x, κ_x and κ_{xy} are the second partials of a function describing the out-of-plane shape of the shell.

Figure 5.2 displays three unique classes of surfaces with distinct Gaussian curvatures. The first, depicted in Figure 5.2(a) is a cylinder. As this shape contains only one direction of curvature, the Gaussian curvature is uniquely zero. This is also the case for flat plates containing no curvature terms. The next surface, shown in Figure 5.2(b) is a hyperboloid characterized by negative Gaussian curvature. At any point on the surface

the principal curvatures are of opposite sense and thus their product is less than zero. Finally a spherical cap, characterized by positive Gaussian curvature is found in Figure 5.2(c). More generally, any surface with same sense principal curvatures (ie. ellipsoids, paraboloids) belong to this family of surfaces and thus will exhibit positive Gaussian curvature. Therefore, it is not sufficient to uniquely classify the shape of a surface based on Gaussian curvature alone. However for extremely thin-shells exhibiting negligible bending stiffness, a reconfiguration into *any* surface having the same Gaussian curvature can occur without deforming the surface mid-plane. This is known as inextensible bending [51]. For example, an initially flat thin sheet can be rolled along one axis under the application of negligible loads while still maintaining zero Gaussian curvature. Additionally, a thin spherical cap can be "pinched" in one direction, creating an ellipsoid, all while maintaining the same positive Gaussian curvature.

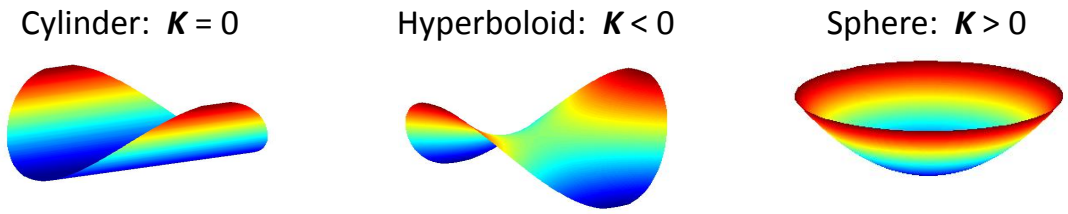

(a) (b) (c)

Figure 5.2: Gaussian curvature of a) Cylinder, b) Hyperboloid (Saddle/Astigmatism) and c) Spherical cap.

Speckle photogrammetry is used to measure the nanolaminate shape and Gaussian curvature. The experimental procedure used to perform the measurement is as follows: a nanolaminate, deposited on a mandrel with a 2.0 m spherical ROC, is carefully delaminated by freeing the edges with a razor blade. In this process, small fractures are created around the perimeter of the nanolaminate, however they do not propagate into the central portion of the film. Once the majority of the edges are free, the nanolaminate is able to be removed entirely from the mandrel with ease. The convex side of the now free-standing nanolaminate is covered with a thin, continuous layer of white paint. Care must be taken in order to ensure an even thickness distribution of paint such that local hills are not produced. A fine mist of black paint is then applied to this surface creating a speckle pattern required for speckle photogrammetry. The nanolaminate is then placed on a flat surface and the out-of-plane measurement of the surface is performed. The local Gaussian curvatures are then determined and compared to that of the mandrel.

As the nanolaminate is in an unsupported state, it is susceptible to gravity effects that will significantly change the geometry of the film. However, due its low thickness, it is assumed that these effects will have a preference to deform the nanolaminate in bending. From the statements above it is noted that appreciable changes in Gaussian curvature are only possible through extensions of the shell mid-plane (Note: the proceeding Chapter demonstrates this for the case of a flat plate under spherical deformations). Bending deformations will not change the Gaussian curvature of a surface as these are inextensible modes of defor-

Table 5.1: Mean Gaussian curvature and radius of curvature of the free-standing nanolaminate and deposition mandrel.

	Nanolaminate	Mandrel
K (m^{-1})	0.232	0.250
ROC (m)	2.04	2.00

mation and therefore it is assumed that the Gaussian curvature of the nanolaminate will remain relatively unaffected by gravity.

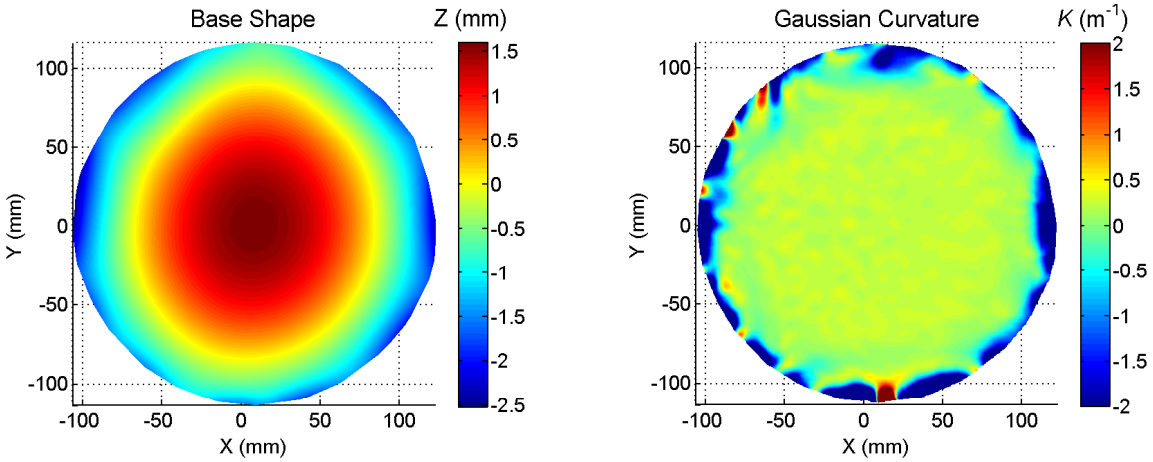

(a) (b)

Figure 5.3: a) Measured shape and b) Gaussian curvature of a free-standing nanolaminate.

Figure 5.3 displays the measured shape and Gaussian curvature of the free-standing nanolaminate. From the surface measurement, it is apparent that the nanolaminate takes on a slightly elliptical shape. It is believed this is due to gravity effects. However, when considering the Gaussian curvature it is apparent that a near-constant region is present in the central portion of the nanolaminate (edge effects from the fractures created during delamination are present around the perimeter of the nanolaminate). The average value of Gaussian curvature and mean radius of curvature in this region are listed in Table 5.1 and compared to that of the mandrel. For the nanolaminate, a mean Gaussian curvature of 0.232 m^{-1} is measured, with an average radius of curvature of 2.04 m. These measurements are in good agreement with the mandrel having a constant Gaussian curvature of 0.250 m^{-1} and 2.00 m radius of curvature.

While the shape of the free-standing nanolaminate matches that of the mandrel, definitive conclusions on the as-deposited stress-state of the nanolaminate cannot be made. While the proposition that mid-plane extensions are necessary for changes in Gaussian curvature is true, the converse statement is not necessarily true; extensible deformations do not necessarily result in Gaussian curvature changes. For example, a flat sheet of paper can be stretched in the plane without changing Gaussian curvature. Therefore, the results of this test do not indicate if the nanolaminate was under a uniform state of stress prior to delamination.

However, it is believed that the results of this study provide sufficient evidence to claim that the level of stress in the nanolaminate is relatively low as evident by the matching curvatures between the free-standing part and rigid mandrel.

5.3 Nanolaminate Bonding

Two bonding processes were attempted in order to integrate nanolaminates onto the front surface of the CFRP substrates: 1) a thermal co-cure where the CFRP substrate is cured directly on top of the nanolaminate under autoclave conditions, and 2) a room-temperature process where an already cured CFRP substrate is bonded to the backside of the nanolaminate using liquid epoxy.

5.3.1 Thermal Co-Cure

Figure 5.4: Top-view of CFRP + nanolaminate facesheet after a thermal co-cure displaying significant thermal distortions.

A thermal cure of the CFRP substrate directly onto the backside of a nanolaminate was attempted on a small free-standing sample. In this process a coupon of uncured CFRP prepreg is laid up directly on the backside of the nanolaminate. The entire assembly is then vacuum-bagged and subjected to autoclave curing conditions. In this method, the epoxy resin from the CFRP material will be used as the bonding adhesive. Figure 5.4 displays a top-view of the sample after the cure. It is apparent that significant warping of the substrate has occurred as the part displays large-magnitude curvature terms. This is due to the non-zero CTE difference between the two materials ($\sim$ 6 ppm/°C for the nanolaminate in comparison to $\sim$ 2 ppm/°C for the CFRP). Small local imperfections are also observed, however; these are attributed to small contaminate particles that were trapped between the nanolaminate surface and the underlying mandrel during cure. Therefore, from the results of this initial study, it was determined that a direct cure of the CFRP material onto the back surface of the nanolaminate was not feasible for this activity.

5.3.2 Room-Temperature Cure

In order to mitigate the thermal distortions observed above, room-temperature cures were implemented. Specifically, low-viscosity two-part epoxy (EpoTek-301) was used for bonding. However, even in the absence of elevated temperatures there are many difficulties associated with this process. Firstly, as the CFRP substrates are extremely thin, pressure-induced substrate warping can occur while the cure is performed. This warping translates directly into low to mid spatial frequency errors upon removal of the assembly from the mandrel. Second, obtaining an imperfection-free surface can prove challenging. Surface features on the CFRP substrate, particulate contaminates in the bond-line, and improper out-gassing of the epoxy can produce high-spatial frequency errors (dimples/valleys) on the mirror surface. Finally, contraction of the epoxy during cure can produce higher-order spherical aberrations in the mirrors. All of these factors must be taken into consideration during the fabrication process.

The successful process used for this effort implements a filled epoxy and a variable-pressure cure cycle. The process is as follows: glass spacer-beads (Potters EMB-10) are first mixed with Part A of the epoxy at a mass fraction of 25%. The glass spheres are used to nominally set the thickness of the bond-line between the CFRP substrate and nanolaminate. The mixture is stirred vigorously in order to avoid clumping of the glass spheres and then out-gassed in a bell jar for 1 hour. Part B is then added to the mixture, stirred for 10 minutes, and out-gassed for 15 minutes. A syringe is then used to extract the desired amount from the mixing pot and a central pool of epoxy is placed directly onto the front (concave) surface of the CFRP substrate. In doing so, the epoxy will naturally spread out under gravity over the middle portion of the surface. This is then placed back into the bell jar for further out-gassing ($\sim$ 20 minutes). The higher surface area associated with the thin pool of epoxy allows for a more complete out-gassing procedure to be performed. Once complete, the CFRP substrate is removed from the bell jar and placed on a flat surface. The nanolaminate, supported by its mandrel, is then aligned and placed down onto the central pool. A small amount of manual pressure is applied in order to ensure even flow-out of the epoxy. The assembly is carefully flipped over with the mandrel now on the bottom. The entire assembly is then vacuum-bagged for subsequent pressure application.

The details of the variable-pressure curing process were determined empirically based on the observed surface quality of the final part. The first step is to apply an initial pressure of 1 atm for 10 minutes. In this step, the epoxy flows completely throughout the interface due to its low viscosity. At this point, the thickness of the bond-line is nominally set by the diameter of the glass spacer-beads in the epoxy, approximately 10 μm. However, due to a relatively wide distribution in the bead diameter along with the fact that the surface of the CFRP laminate is not uniform, local stresses in the nanolaminate and/or CFRP substrate can occur. To relieve these stresses, the bonding pressure is slowly removed over a duration of 20 minutes. This allows a small amount of epoxy to flow back into the bond-line from the edges and redistribute throughout. The final cure between the CFRP substrate and nanolaminate occurs under zero applied pressure.

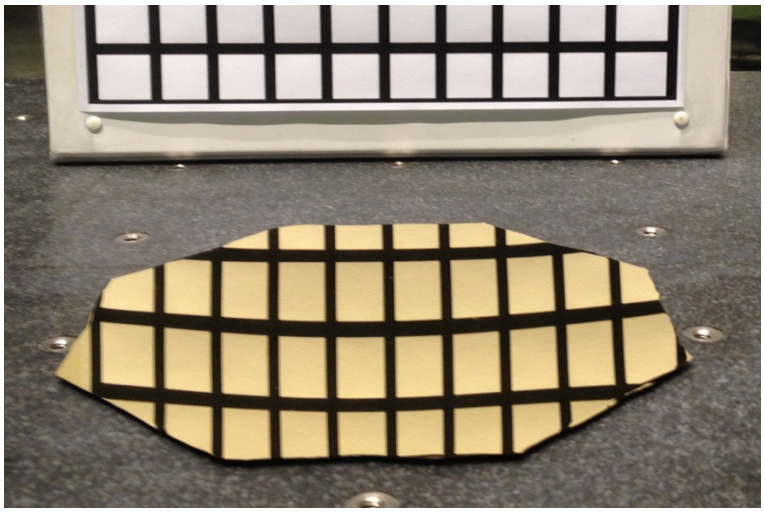

Figure 5.5: Successful integration of nanolaminate onto a 200 mm dia. CFRP substrate.

Figure 5.5 displays a picture of mirror containing a 16-ply CFRP substrate and nanolaminate facesheet displaying the highly reflective front surface. Using the refined bonding process outlined above, a figure accuracy of 2.4 μm RMS over 80% of the mirror was achieved. It is noted that a decrease in figure error is observed with the addition of the nanolaminate. This is attributed to two factors: 1) epoxy fill-in from the variable pressure cure and 2) the additional stiffness from the nanolaminate providing resistance to low-spatial frequency errors.

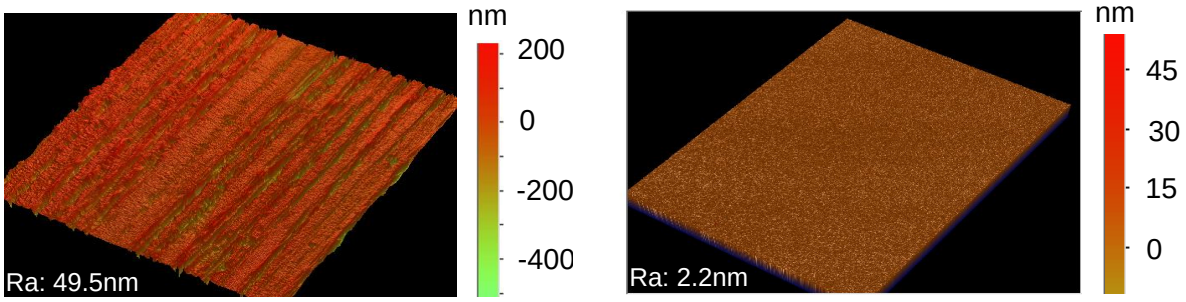

(a) (b)

Figure 5.6: White light scanning interferometer (Veeco Wyko) measurements of a) a bare CFRP substrate after replication displaying significant fiber print-throughand b) a mirror prototype after nanolaminate integration showing complete mitigation of fiber print-through (Ra: 2.2 nm).

Figure 5.6 displays a measurement of the surface roughness before and after successful integration of a nanolaminate. The bare CFRP substrate displays significant evidence of fiber print-through effects with 49.5 nm Ra roughness. After the bonding process, the the appearance of fibers is eliminated and a 2.2 nm Ra surface roughness is achieved. This represents a factor of 23 increase in surface quality and is suitable for

visible-wavelength applications, thus demonstrating the utility of integrating the nanolaminate facesheet.

Chapter 6

Figure Errors from Active Layer

This chapter provides an overview of the deformation mechanics associated with bonding multiple, initially flat PZT plates to the backside of a continuous spherically curved CFRP substrate. The change in global shape as a result of this process is studied as well as the highly localized shape imperfections due to the discontinuity between successive plates. As PZT is an active material, the effect of isotropically straining these elements simulating the actuation process, is also considered. A more detailed study of the actuation process is covered in Chapter 7. The studies are performed using Abaqus 6.12 and conventional shell elements. A higher-order model using continuum shell elements is also developed in order to study the effect of transverse shear on the localized deformation at the discontinuities.

6.1 Background and Motivation

Significant limitations exist on the in-plane dimensions of thin active ceramic plates(i.e., PZT). This is due to manufacturing constraints associated with tape-casting techniques, a process by which a slurry of "green" PZT is sintered at very high temperatures. For free-standing films, the maximum in-plane dimension of such plates is currently limited to ~ 100 mm. However, for many applications including those for active mirrors, it is desired to have continuous coverage of active material across the backside of a substrate. Methods have been developed in order to deposit active materials in continuous films using sputter-deposition techniques [52]. However, to date only very thin films (< 5 μm) have been produced and thus only small actuation stresses can be realized.

A simple method to achieve large-area coverage of active material is to bond multiple plates in a tessellation across the backside of a continuous substrate. However, with this process several concerns arise. The first is due to the fact that the PZT plates are manufactured flat. In order to conform to the doubly-curved surface of the CFRP substrate they must undergo large deformations prior to bonding. This represents a change in Gaussian curvature from zero to a positive value. Therefore, significant mid-plane extensions must occur in order for the PZT plate to take on the non-developable configuration. The magnitude of these extensions is non-constant across the surface of the plate, and therefore the stress distribution prior to

bonding will be non-uniform. It is expected that these high magnitude, non-uniform stresses will cause significant deformations subsequent to the bonding process. The second concern is related to the gaps between successive plates. These gaps can arise due to a number of sources. The first, is simply due to practical limitations associated with bonding multiple plates next to each other. Even with proper tooling alignment becomes difficult, as each plate must have precision edge profiles in order to be seated perfectly next to each other. However, more notable is the fact that it is impossible to produce a perfect tessellation of identical unit cells across a spherical surface, as shown in [53]. Therefore, if identical flat plates are to be bonded to a curved surface, gaps are inevitable. Of particular interest here is understanding the highly localized shape deformations produced during bonding as a function of gap width. Finally, as these are active materials with the capability to strain in the plane, it is desired to study how the laminate deforms when the discrete plates are actuated uniformly.

6.2 Model Overview

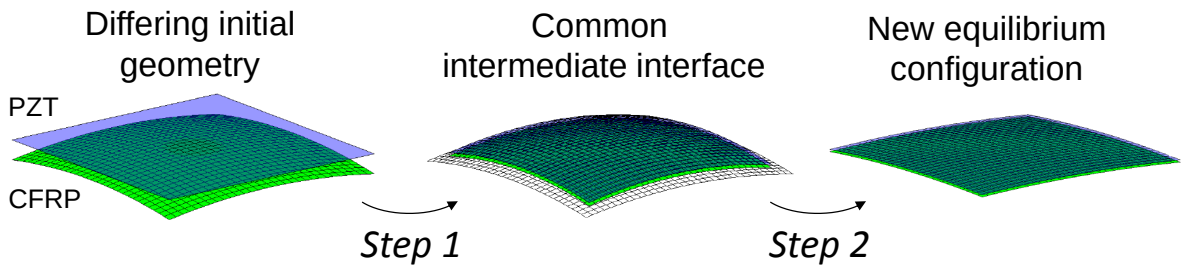

Figure 6.1: Overview of model displaying two substrates having dissimilar geometry, undergoing deformation to a common interface (Step 1) and determination of the new, post-bonded equilibrium configuration (Step 2).

A geometrically non-linear finite element model was implemented in Abaqus 6.12 in order to model the above effects. Conventional shell elastic elements with linear interpolation and reduced integration (S4R elements) are used to model both the PZT plates and CFRP substrate. The simulation is performed in two steps, depicted in Figure 6.1. In Step 1, the flat PZT plates are deformed to the surface of the spherical CFRP substrate such that they share a common interface (the details of this deformation process are outlined in the next section). The stress distribution in the PZT plates is of interest here. Specifically, the ratio of mid-plane stresses to bending stresses is studied. Analyses are performed for PZT plates that span the entire in-plane dimension of the CFRP substrate as well as for smaller discontinuous plates. In Step 2, the bonding process between the two materials is simulated through a contact formulation that allows no separation or slip between the surfaces once engaged. In doing so, surface tractions can be transferred between each substrate. Care must be taken when using conventional shell elements with contact formulations as the

physical thickness of each substrate is not modeled. Instead a reference surface containing the shell nodes is used to define the initial geometry and subsequent deformations. The thickness of each substrate is defined by specifying an offset from this surface in either the positive or negative direction. For the current model, the convex surface of the CFRP substrate was set as the reference surface and the bottom surface facing the CFRP substrate was used as the reference for the PZT plates, as shown in Figure 6.2. With this configuration the contact formulation will engage if the bottom surface of the PZT is in contact with the convex surface of the CFRP substrate, as intended. Identical meshes are not required between the two parts as interpolation between nodal coordinates is used to define the surfaces. This contact formulation is defined at the beginning of the analysis step. After doing so, all constraints on the assembly are removed except at a central node on the CFRP substrate, where all 6DOFs are constrained. This allows the now bonded CFRP substrate and PZT plates to deform and reach its final equilibrium state. The magnitude and mode of this deformation is of interest to this study.

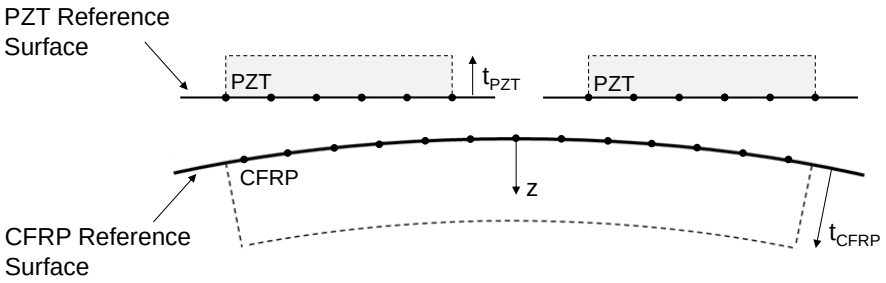

Figure 6.2: Reference surface and thickness definition of the CFRP and PZT parts.

6.2.1 Deformation Boundary Conditions

The PZT plates must undergo deformations such that their reference surface matches exactly with the reference surface of the CFRP substrate before the relaxation process. This is required in order for the contact formulation to be imposed. However, the challenge with this process is that the mid-plane of the PZT must be allowed to deform freely upon deformation in order to capture the proper stress state. Three possible boundary conditions were considered in order to impose these conditions. They are depicted in Figure 6.3.

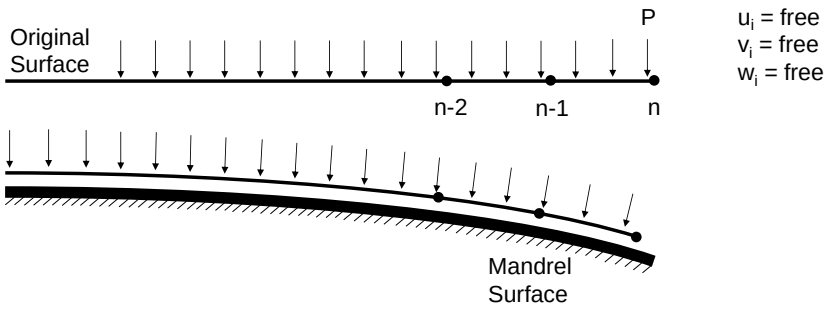

(a)

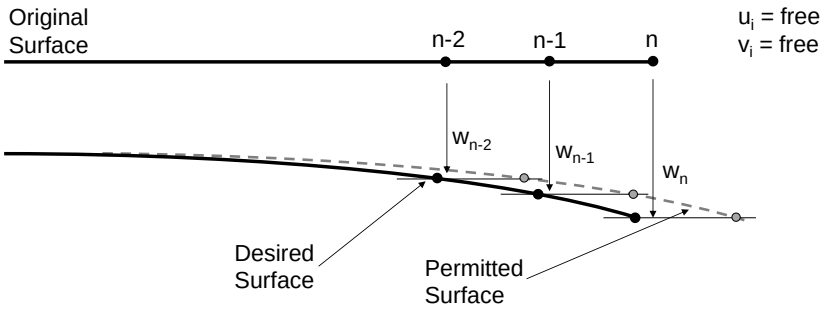

(b)

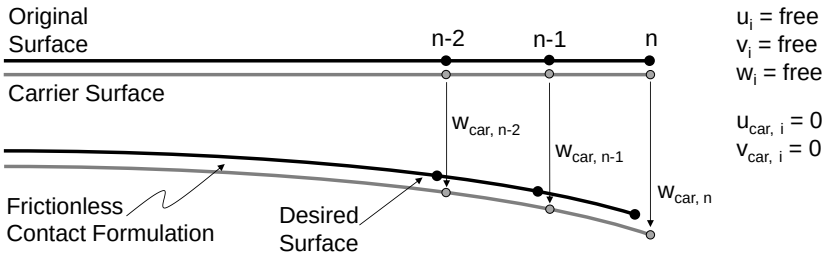

(c)

Figure 6.3: Permitted boundary conditions for non-linear finite element model.

The first, depicted in Figure 6.3(a), considers the prescription of a pressure loading condition in order to deform the substrate to a supporting mandrel. The mandrel is modeled as a discrete rigid surface and is fixed in all DOFs. A contact formulation is defined between the substrate and mandrel, preventing penetration while allowing deformation to occur freely in the tangential direction. This formulation is a physical representation of the bonding process where pressure is applied to deform the plates to the top of a mandrel. However, as the level of contact between the substrate and mandrel varies, small analysis increments are required and thus relatively long analysis times result. In addition to this, it was found to be difficult to predict the required magnitude of pressure required to deform the substrate to the exact mandrel shape.

The second, depicted in Figure 6.3(b), considered prescribing out-of-plane displacement boundary conditions while leaving in-plane DOFs free. While this allows the mid-plane of the PZT plates to stretch freely, it does not uniquely define the desired surface to which both surfaces must meet. Therefore, incomplete levels of contact were realized throughout analysis attempts.

The third, depicted in Figure 6.3(c), prescribes nodal displacement boundary conditions on a fictitious surface, defined as a "carrier" surface. The PZT plates are placed adjacent to this surface and a zero-friction contact formulation is defined between the two. This simulation technique forces the plates to lie on the exact desired surface defined by the carrier surface while allowing the mid-plane to deform freely. As the contact formulation is constant throughout the analysis step, larger analysis increments can be used, resulting in short analysis times. As such, this was chosen as the proper solution for subsequent analyses.

6.3 Step 1: Stress distribution due to Spherical Deformations

6.3.1 Circular Plates

The stress distribution due to spherically induced deformations of an initially flat plate was studied first. As a general case, a circular plate was first modeled due to its axisymmetric properties. The spherical deformation was imposed by defining the deformation boundary conditions (via the carrier surface) as follows

$$w(r) = \frac{r^2}{2R}, \tag{6.1}$$

where w is the out-of-plane deformation of the plate, r is the radial coordinate, and R is the radius of curvature to which the plate will be deformed. It is convenient to non-dimensionalize the out-of-plane deformation, w, and radial coordinate, r, by the thickness and radius of the plate, respectively. This is done as follows

$$\bar{w} = \frac{w}{t}, \tag{6.2}$$

and

$$\bar{r} = \frac{r}{r_o}, \tag{6.3}$$

where t is the thickness and r_o is the radius of the plate. In doing so, the following equation arises:

$$\bar{w}(\bar{r}) = \frac{{r_o}^2}{2Rt}\bar{r}^2. \tag{6.4}$$

Therefore, the non-dimensional amplitude of spherical deformation imposed on an initially flat plate can be generally defined through a loading parameter denoted as Γ:

$$\Gamma = \frac{{r_o}^2}{2Rt} \tag{6.5}$$

and therefore, Equation 6.4 becomes:

$$\bar{w}(\bar{r}) = \Gamma \bar{r}^2. \tag{6.6}$$

From Equation 6.5 it is apparent that Gamma is proportional to the square of the plate radius and inversely proportional to the thickness of the plate as well as the deformed radius of curvature. In physical terms, it is the ratio of maximum out-of-plane deformation relative to the thickness of the plate.

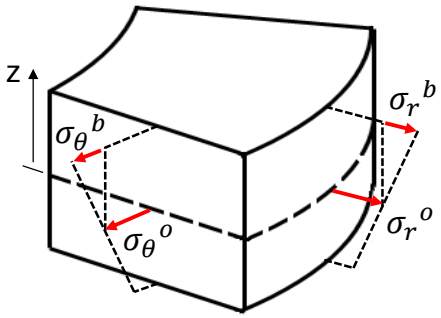

Figure 6.4: Radial element displaying mid-plane and bending stress components.

It is also convenient to decompose the resulting in-plane stress components into two components. As stress varies linearly through the thickness of the plate, this can be performed by defining the stress at the mid-plane, σ_i^o, and the difference in stress at the top of the plate compared to that at mid-plane, denoted as the bending stress, σ_i^b, for i = r, θ in polar coordinates. The bending stress is therefore defined as

$$\sigma_i^b = |\sigma_i(z = \pm t/2)| - \sigma_i^o. \tag{6.7}$$

It is denoted as the bending stress due to the fact that it is the dominant component of stress when the bending deformations are small in comparison to the thickness of the plate. It can be determined from Kirchhoff plate theory where the radial and circumferential strains are defined as

$$\epsilon_r = \frac{du}{dr} - z\frac{d^2w}{dr^2}, \tag{6.8}$$

and

$$\epsilon_\theta = \frac{u}{r} - z\frac{1}{r}\frac{dw}{dr}, \tag{6.9}$$

where u is the radial displacement of the mid-plane. By imposing a free edge boundary condition at r = a, a finite strain condition at r = 0, and using Equation 6.1, the radial and circumferential bending stress components are found to be

$$\sigma_r^b = \sigma_\theta^b = \pm\frac{Et}{2(1-\nu)R} \tag{6.10}$$

for a circular plate with isotropic modulus, E. The bending stress components are constant over the plate

when subjected to pure spherical deformations (curvature changes). Kirchhoff plate theory does not, however, account for mid-plane stretches resulting from large out-of-plane deformations. The mid-plane stress distributions were determined using the model above, accommodating large out-of-plane deformations, as well as arbitrary plate geometries.

Figure 6.5 displays the mid-plane stress distributions in the radial and circumferential directions across the surface of the plate normalized by the maximum tensile stress. This maximum is at the center of the plate where the mid-plane stress in the radial and circumferential directions are equal in magnitude and sign. Both stress components decrease in the radial direction in the same fashion; however, the circumferential stress becomes compressive at the edge while the radial component goes to zero in order to satisfy the free-edge boundary condition.

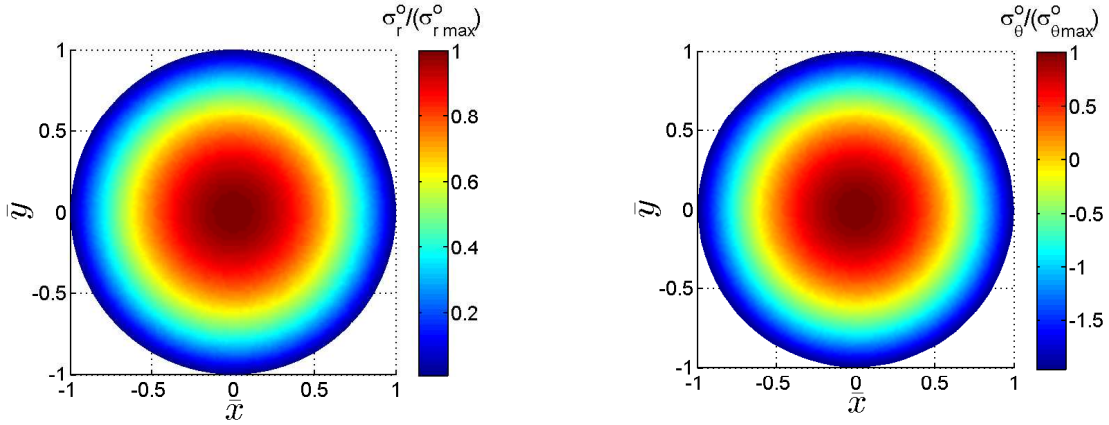

(a) (b)

Figure 6.5: Normalized mid-plane stress distribution in a) radial and b) circumferential directions due to spherical deformations of an initially flat circular plate (Note difference in colorscale).

To study the mid-plane stresses further, the ratio of mid-plane stresses to bending stresses is defined as

$$\bar{\sigma}_i = \frac{\sigma_i^o}{\sigma_i^b}. \tag{6.11}$$

Figure 6.6 displays this ratio along the radial coordinate at various levels of the loading parameter, Γ. It is apparent that at low amplitudes of deformation (low Γ), the mid-plane stresses are negligible with respect to the bending stresses. However, as Γ is increased, the mid-plane stresses become significant. At $\Gamma = 5.0$, the mid-plane stresses are nearly equal to that of the bending stresses at the center of the plate and the compressive circumferential component of stress at the edge of the plate is now > 1.5 times the bending stress.

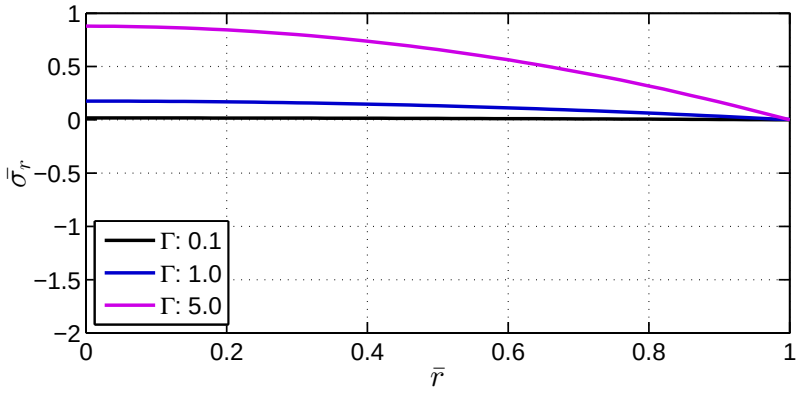

(a)

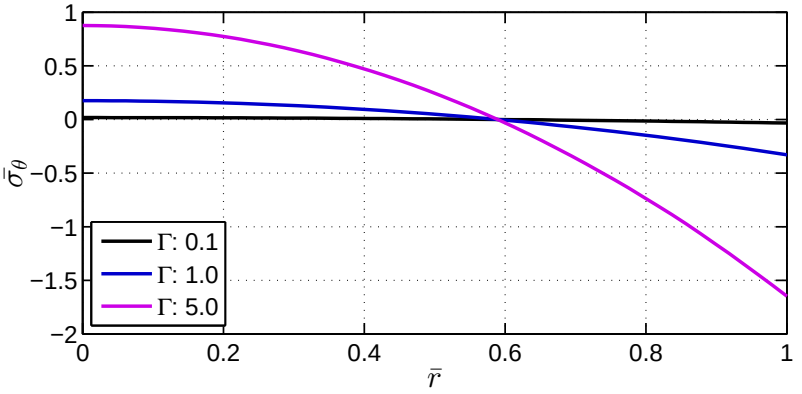

(b)

Figure 6.6: a) Radial and b) circumferential stress ratios (mid-plane / bending stress) along the radial coordinate due to spherical deformations of an initially flat circular plate.

6.3.2 Octagonal Plates

For the purposes of this study, octagonal mirrors have been implemented. Therefore, the above analysis was extended to plates of octagonal shape. The stress distribution was determined using the model outlined above. Figure 6.8 displays the normalized radial and circumferential components of stress throughout the octagonal plate. The distribution of stress is similar to that of the circular plate; however, the behavior towards the edge differs due to the non-axisymmetric shape.

Also of interest here is the effect of patterning the active layer such that smaller initially flat plates are conformed to the spherical surface. Therefore, the octagonal plate of Figure 6.8 was segmented into four quadrants along the central axes of the plate. In doing so, the mid-plane stresses change drastically in order to conform to the new free-edge boundary conditions, as shown in Figure 6.9 (origin remains at the center of the plate). In the radial direction, large compressive stresses are predicted along the x/y axes while the stresses near the edge approach zero. In the circumferential direction, large compressive stresses

are predicted at the edges for $\theta = 45°$. A tensile region is also observed in the central portion of each plate.

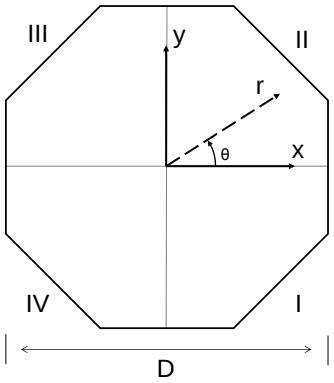

Figure 6.7: Coordinate system for octagonal plate.

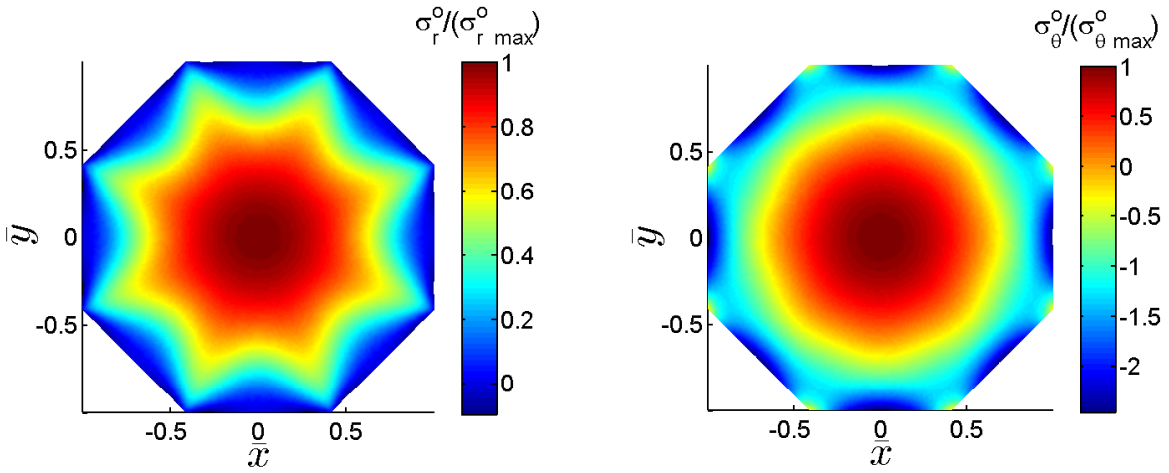

(a) (b)

Figure 6.8: Normalized mid-plane stress distribution in a) radial and b) circumferential directions due to spherical deformations of an initially flat continuous octagonal plate (Note difference in colorscale).

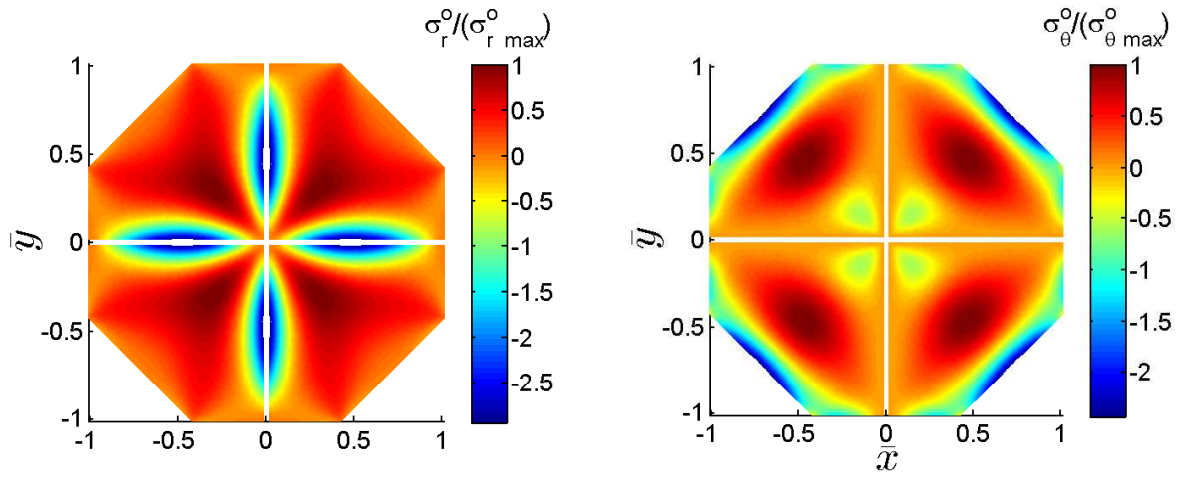

(a) (b)

Figure 6.9: Normalized mid-plane stress distribution in a) radial and b) circumferential directions due to spherical deformations of initially flat sections of an octagonal plate (Note difference in colorscale).

The ratio of mid-plane to bending stress is displayed in Figure 6.10 for the continuous and discontinuous case above. The radial and circumferential components are considered along the radius of the plate at θ = 45° (Quadrant II in Figure 6.7). The diameter of the modeled plate, D, was 150 mm and the thickness was 125 μm. The magnitude of imposed deformation was varied by changing the radius of curvature, R, subsequently varying Γ. As the plate is no longer circular, Γ was calculated by considering the flat-to-flat diameter of the octagon. Therefore, r_o = D/2 for the continuous case and r_o = D/4 for the discontinuous case. Γ is thus defined as

$$\Gamma_{continuous} = \frac{D^2}{8Rt}, \tag{6.12}$$

$$\Gamma_{discontinuous} = \frac{D^2}{32Rt}. \tag{6.13}$$

These values are summarized in Table 6.1 for the considered values of R. Significant mid-plane stresses are predicted for the continuous case, especially at R = 2.0 m. At this level of deformation the mid-plane stresses are a factor of 2 higher than the bending stresses at the surface of the plate. The compressive tangential forces at the edge of the plate are 4.3 times larger than the bending stresses. For the discontinuous case, the mid-plane stresses at r = 0 are zero in both the radial and circumferential directions due to the free-edge condition and the geometry of the plate. The radial component of stress increases towards the middle of the segment, with a maximum at $\bar{r}$ = 0.43. The circumferential component of stress oscillates in sign with a maximum tensile value at $\bar{r}$ = 0.66.

Table 6.1: Γ values for continuous and discontinuous octagonal plates (D = 150 mm, t= 125 μm).

R (m)	$\Gamma_{continuous}$	$\Gamma_{discontinuous}$
2.0	11.25	2.81
4.0	5.63	1.41
10.0	2.25	0.56

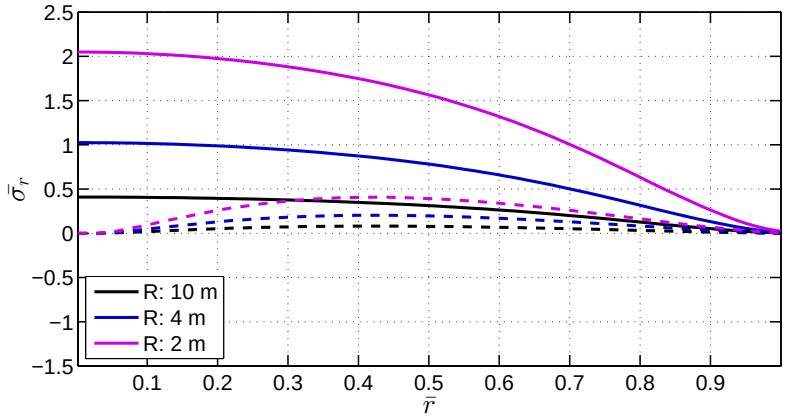

(a)

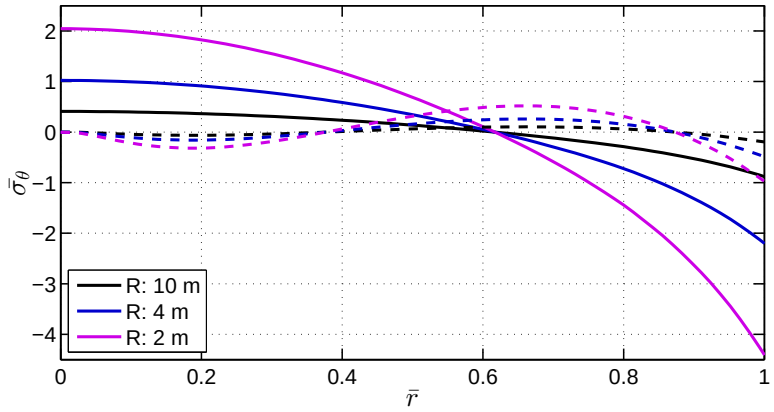

(b)

Figure 6.10: a) Radial and b) circumferential stress ratios (mid-plane / bending stress) along the radial coordinate at $\theta = 45°$ for the continuous plate (solid) and discontinuous patches (dashed).

6.4 Step 2: Deformation due to Bonding

In this step of the analysis the PZT material is bonded to the backside of the CFRP substrate by first initiating a no-slip contact formulation, and then the entire assembly is allowed to deform to its new unconstrained equilibrium condition. The CFRP substrate is modeled as a spherical surface with a 2.0 m radius of curvature. The substrate was defined as an octagon with a diameter of 150 mm flat-to-flat. The 8, 16, and 32-ply

Table 6.2: CFRP laminate orientations.

Laminate	Ply Number	Orientation
1	8	$[0°/+45°/\text{-}45°/90°]_s$
2	16	$[0°/+45°/\text{-}45°/90°]_s + [90°/\text{-}45°/+45°/0°]_s$
3	32	$\left[[0°/+45°/\text{-}45°/90°]_s + [90°/\text{-}45°/+45°/0°]_s\right]_2$

laminate orientations described in Chapter 4 were defined for this study and are summarized in Table 6.2. Each ply is 30 μm thick and therefore 240, 480, and 960 μm substrates are considered. The properties of the M55J material were used for this study. The orthotropic material properties are summarized in Table 6.3.

The continuous and discontinuous cases were modeled by defining the PZT plate as a continuous octagon or as four segments as in the previous section. The octagon is slightly undersized from the CFRP substrate here at 145 mm in diameter (this is performed in order to accommodate the gaps between discontinuous plates). A constant thickness of 125 μm was used for all analyses. The material properties of the PZT were obtained from the manufacturer and can be found in Table 6.3 as well.

Table 6.3: Material properties of 1) unidirectional M55J and epoxy resin ($V_f \approx 50\%$) and 2) PZT-5A.

Property	CFRP	PZT
E_1 (GPa)	340.0	66.0
E_2 (GPa)	6.0	66.0
G_{12} (GPa)	4.2	25.0
ν_{12}	0.35	0.30

A schematic of the model displaying the discontinuous analysis case is found in Figure 6.11. The coordinate system for the model is defined with the origin at the central node of the CFRP substrate and the x and y axes along the tangent plane at that location. The out-of-plane coordinate, z, is defined as positive down, or in the direction of the surface normal at the origin on the concave side of the CFRP substrate. The PZT plates are located directly above the surface of the substrate in the xy plane. Their relative position with respect to each other is defined depending on the desired gap width to be modeled. The central regions of both the CFRP substrate and PZT plates are sectioned off in order to refine the mesh at these locations.

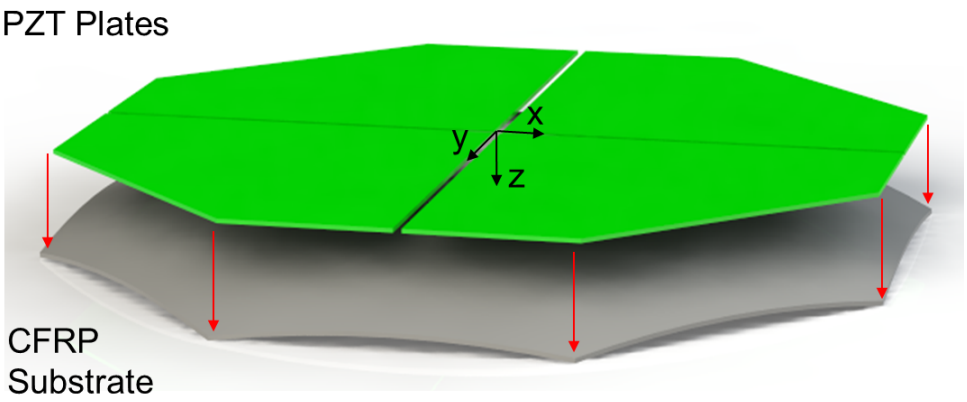

Figure 6.11: Abaqus model displaying continuous CFRP substrate and four discrete PZT patches modeled using conventional shell elements (S4R).

6.4.1 Global Deformation

The global deformation of the CFRP substrate after the bonding process was first considered. In this analysis, both the continuous and discontinuous cases were modeled. For the discontinuous case, the PZT plates are aligned such that there is a 0.25 mm gap between each other. (Note: the analysis was performed with alternate gap sizes; however, there was no significant change in the observed global deformation.) The PZT is deformed to the surface of the CFRP substrate and then "bonded" by initiating the no-slip contact formulation. The deformation upon release of the bonding constraints is then observed. Figures 6.12, 6.13, and 6.14 display the corresponding global deformations for 8, 16, and 32-ply CFRP substrates.

From the results it is apparent that there is a significant variation in deformation when considering continuous/monolithic vs. discontinuous PZT plates for all CFRP substrates. For the continuous results, depicted in Figures 6.12(a), 6.13(a), and 6.14(a), low-order global deformations are observed. However, for the discontinuous case, shown in Figures 6.12(b), 6.13(b), and 6.14(b), higher order modes of deformation are predicted, producing lobed structures at the location of the discrete plates. The amplitude of predicted deformation is also significantly lower in the discontinuous case compared to that of the continuous case. It can also be noted that the 16 and 32-ply substrates undergo deformations that have 4-fold, 90° symmetry while the deformations of the 8-ply substrate display 180° rotational symmetry. This is due to the lack of isotropy with respect to bending stiffness for the 8-ply laminate as mentioned in Chapter 4.

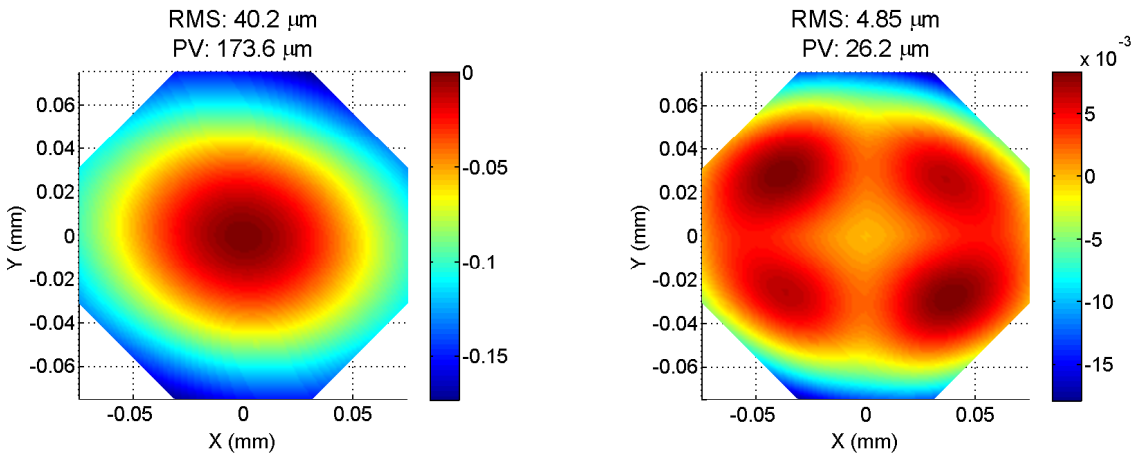

(a) (b)

Figure 6.12: 8-ply substrates: Global deformation of CFRP substrate after bonding a) a continuous plate or b) four discrete patches of PZT.

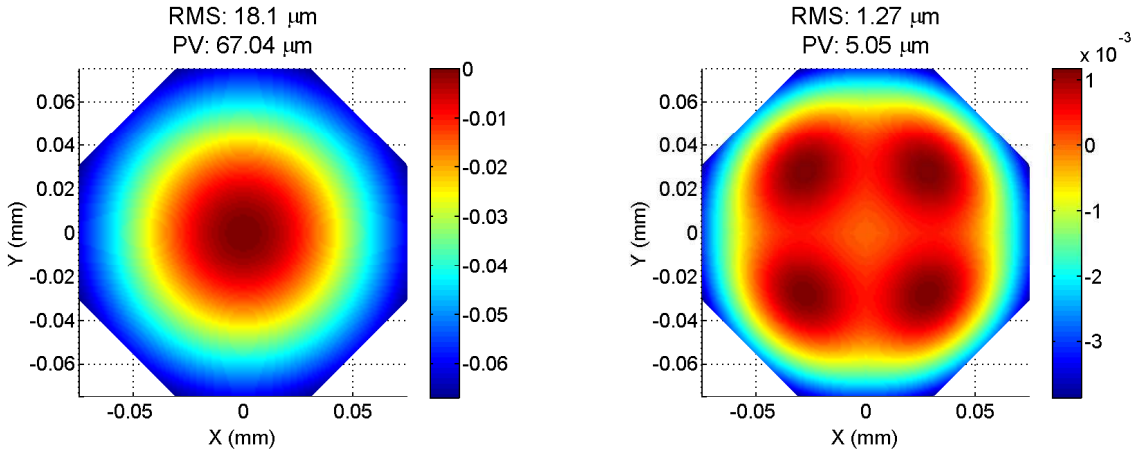

(a) (b)

Figure 6.13: 16-ply substrates: Global deformation of CFRP substrate after bonding a) a continuous plate or b) four discrete patches of PZT.

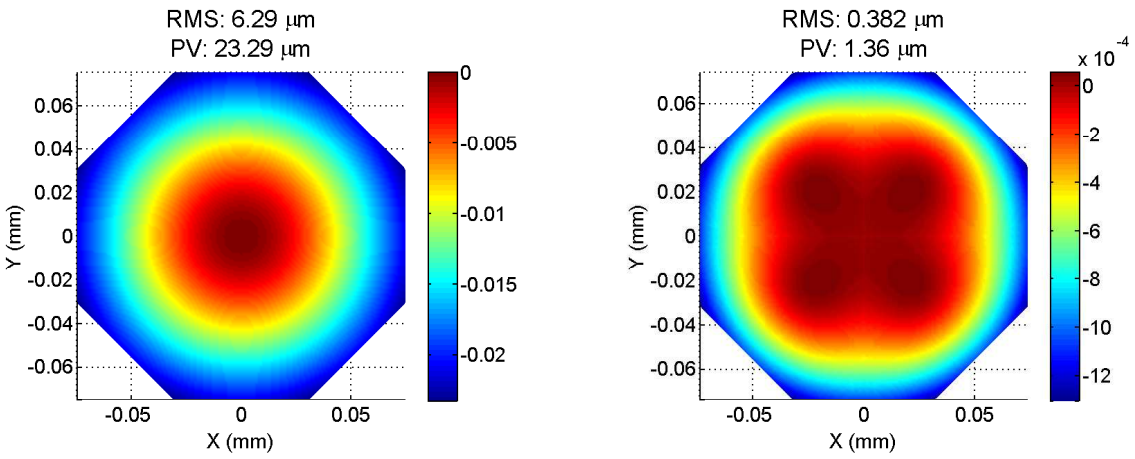

(a) (b)

Figure 6.14: 32-ply substrates: Global deformation of CFRP substrate after bonding a) a continuous plate or b) four discrete patches of PZT.

The variation in deformation between the two simulation cases is due to the variation in mid-plane stress distributions in the continuous plate vs. the discontinuous patches. At 2.0 m, the necessary curvature change is large, corresponding to Γ values of 11.25 and 2.81 for the continuous and discontinuous cases, respectively. Therefore, mid-plane stresses are significant, as shown in Figure 6.10. However they are especially dominant over the bending stresses for the continuous case due to the much greater Γ value. The variation in mid-plane stress is also monotonically decreasing in the radial direction for this case, while higher-order variations are observed for the discontinuous case. These variations in mid-plane stresses are the source of the "lobed" structures observed in Figures 6.12, 6.13, and 6.14.

To study these effects further, analyses were performed at lower values of Γ. This was performed by increasing the radius of curvature of the CFRP substrate, R, and thus lowering the required deformation of the initially flat PZT plates. The deformation after the bonding process was determined at each increment. For simplicity, 16-ply substrates are only considered here. Figure 6.15 displays the PV deformation of the substrate after bonding for increasing initial radius of curvature. A significant reduction in the predicted level of deformation is observed for the continuous case. At R = 10.0 m, the level of substrate deformation approaches that of the discontinuous case. In this situation, the bending stresses in the PZT plates begin to dominate over the mid-plane stresses. As the bending stresses are identical in magnitude for the continuous and discontinuous cases, the resulting substrate deformation after the bonding process becomes similar in nature.

Figures 6.16 and 6.17 display the mode of deformation for a select subset of these results (R = 2.0, 4.0, and 10.0 m). As the radius of curvature is increased, the appearance of the lobed-structure produced by the discontinuous plates begins to disappear. At R = 10.0 m, the mode of deformation approaches that of the continuous case. This is also due to the decreased effect of mid-plane stresses in the PZT at lower levels of

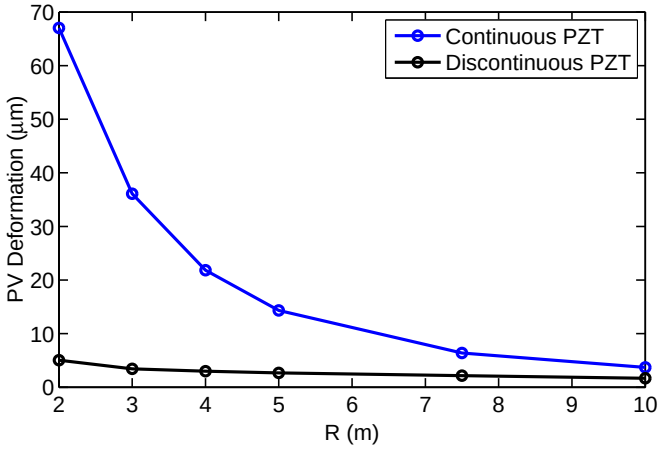

Figure 6.15: Peak-to-Valley (PV) deformation of the CFRP substrate due to the bonding process considering various initial radius of curvatures, R.

imposed spherical deformations.

For further analysis, Figure 6.18 displays the normalized curvature changes associated with the deformation. These are defined as

$$\Delta\bar{\kappa}_r = (\Delta\kappa_r)(R) \tag{6.14}$$

where

$$\Delta\kappa_r = \frac{\partial^2 w}{\partial r^2} \tag{6.15}$$

with w denoting the deformation of the substrate in the z-direction. From Figure 6.18 it is apparent that the curvature change is non-uniform across the substrate for all simulation cases. The lowest variation is predicted for the discontinuous case at R = 10.0 m. For the continuous case, the large curvature changes at $\bar{r} = 0$ correspond to the high-tensile regions at the center of the PZT plate. For the discontinuous case, this region is moved to $\bar{r} = 0.69$, which coincides with the location of maximum tensile stress in the circumferential direction for the discontinuous PZT patch. A reversal in sign of the curvature change is observed towards the edge of the mirror substrate for almost all analyses (except for R = 10.0 m in the discontinuous case). This coincides with the high magnitude compressive mid-plane stresses in the circumferential directions at the edges of the PZT (approaching $\bar{r} = 1$). This effect is not seen for R = 10.0 m for the discontinuous case as the mid-plane stresses are near negligible at this level of imposed deformation.

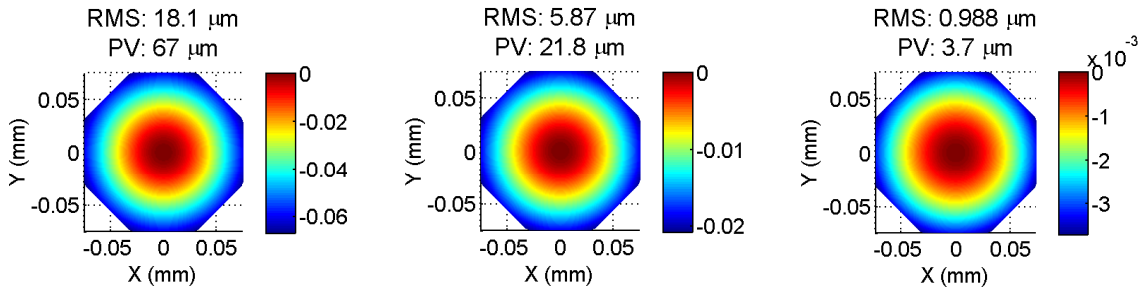

(a) (b) (c)

Figure 6.16: Deformation of a 16-ply CFRP substrate with an initial radius of curvature, R, of 2.0, 4.0 and 10.0 m (a), b), c) respectively) after bonding a continuous sheet of PZT to its backside.

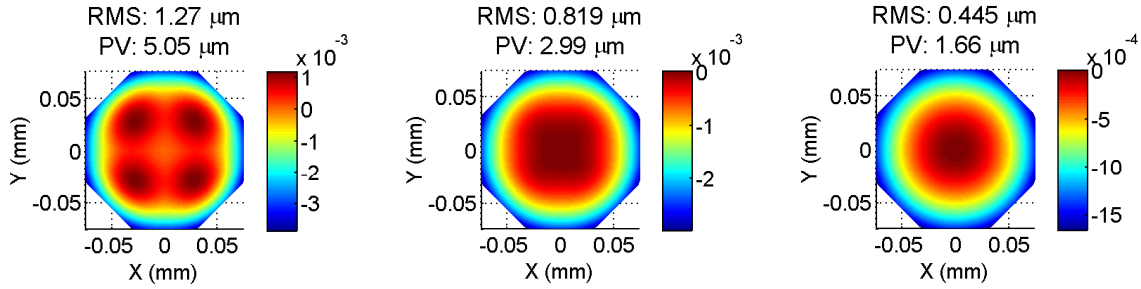

(a) (b) (c)

Figure 6.17: Deformation of a 16-ply CFRP substrate with an initial radius of curvature, R, of 2.0, 4.0 and 10.0 m (a), b), c) respectively) after bonding a four discrete patches of PZT to its backside.

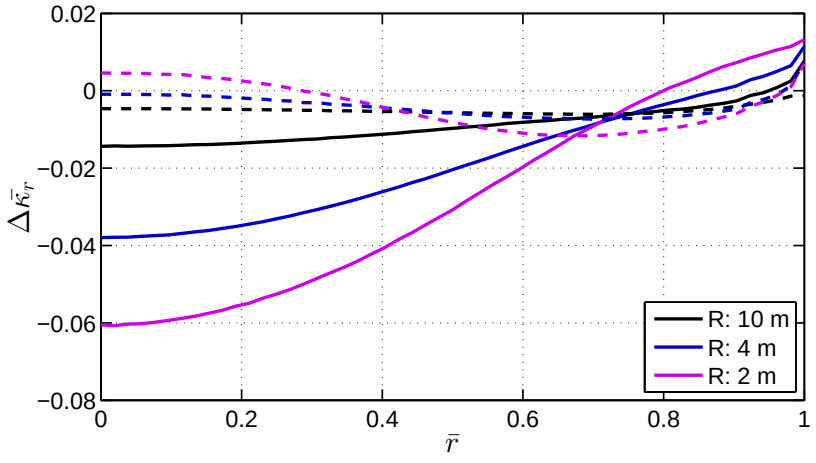

Figure 6.18: Normalized change in curvature due to the bonding process in the radial direction at $\theta = 45°$ for the continuous plate (solid) and discontinuous patches (dashed).

6.4.2 Experimental Measurements

Figure 6.19 is a speckle photogrammetry measurement of the deformation imposed on an 8-ply CFRP substrate after four initially flat PZT plates were bonded to its backside. The plates were bonded using room-temperature cure epoxy and under the application of 1 atm of pressure (via vacuum bag) with a mandrel under the CFRP substrate for support. The relative position of the plates was maintained by taping portions of the edges together using small strips of Kapton tape. The characteristic "lobed" structure is observed in the measurement at each quadrant of the octagonal substrate similar to those predicted in Figure 6.12(a). The overall magnitude of these errors is greater than that predicted by the numerical simulations at 9.7 μm RMS and 43.3 μm PV, respectively. It should be noted that measurements were also attempted for 16 and 32-ply substrates; however, the magnitude of deformation was too low in order to be captured properly by the photogrammetry system.

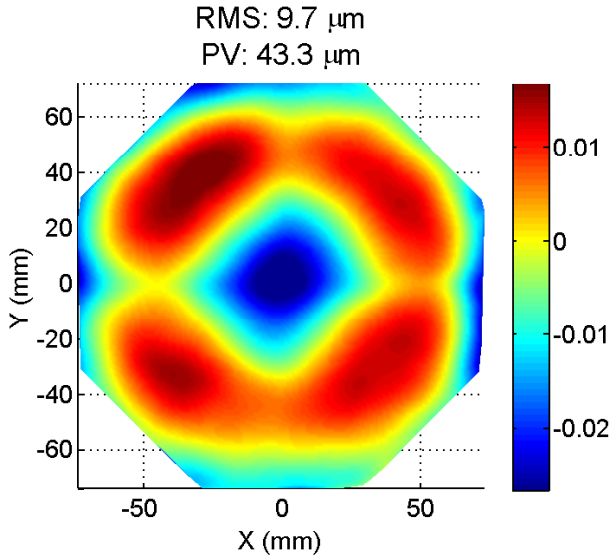

Figure 6.19: Measurement of out-of-plane deformation of an 8-ply CFRP substrate after bonding 4 PZT plates to the backside.

6.4.3 Local Deformation

Local deformations produced at the gaps between each plate were studied next. In order to properly capture these effects, the model mesh was refined significantly along the centerlines of the CFRP substrate, as shown in Figure 6.20. 100 μm elements were implemented to an offset of 2 mm from the x and y axes of the CFRP substrate in order to capture the features at the terminal edges of the PZT. 500 μm elements were implemented to an offset of 10 mm and a global mesh size of 1 mm was used for the remainder of the surface. Identical mesh refinements were implemented at the central edges of the PZT plates. This level of mesh refinement was shown to produce converged results as shown in Appendix C.

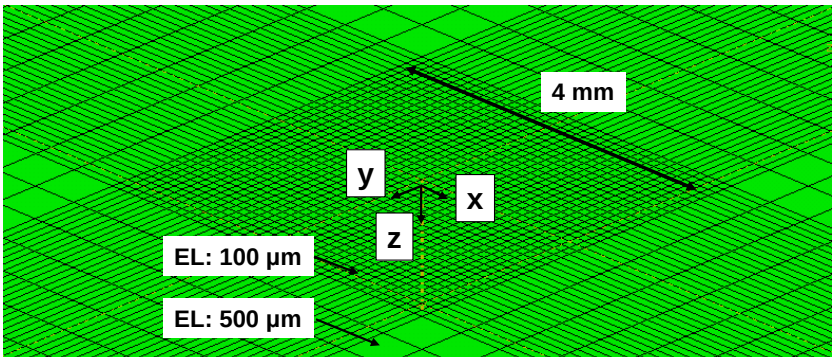

Figure 6.20: Mesh refinement for central portion of CFRP substrate.

Three gap widths were considered for this study: 0.25 mm, 1.0 mm, and 2.0 mm. The local out-of-plane deformation due to the bonding process was determined for each of the three CFRP substrates. Figures 6.21, 6.22, and 6.23 present the local deformation at the central 40 mm wide region on the front (concave) face of the CFRP substrate. A high-pass FFT-based filter and the techniques outlined in Appendix A were used in order to remove the large magnitude global deformations. For this analysis the pass frequency was set to 1/7.5 mm^{-1}, leaving features with spatial frequencies higher than that value for observation. Profiles of the deformation at a constant y-value of 10 mm are also found in Figure 6.24.

From Figures 6.21, 6.22, and 6.23 it is apparent that high spatial frequency deformations are predicted as a result of the bonding process even for small (0.25 mm) gap widths. The deformations are highly local to the gap region and are negative in sign indicating "valleys" are produced on the CFRP substrate when studying the front (concave) surface. Interestingly, the deformation amplitude is predicted to be the greatest for the smallest gap width at 0.25 mm. However, the amplitude of deformation is highly dependent on the CFRP substrate thickness with the largest amplitudes occurring for the 8-ply substrates. It is also noted that for the 16 and 32-ply substrates, equal deformation amplitudes are predicted for the gaps oriented along the x and y axes. However, significant variations are observed for the 8-ply substrates. This is again associated with the symmetry and mechanical response of the laminate orientations. For the 8-ply substrate the top/bottom plies have fibers oriented along the x-axis. As a result, the bending stiffness is much higher along this direction and lower deformations are predicted for the gap perpendicular to these fibers. A comparison between the deformation profile in the x and y directions for the 8-ply substrates is shown in Figure 6.25.

The predicted deformation amplitudes range from $\sim$ 5 nm for the 32-ply substrates to $\sim$ 100 nm (peak-to-valley) for the 8-ply substrates. While these values are small in comparison to the global deformations imposed by the bonding process ($\sim$ 20 - 170 μm), they are highly local in nature. Therefore, the corresponding slope, and thus curvature of these features, is extremely high.

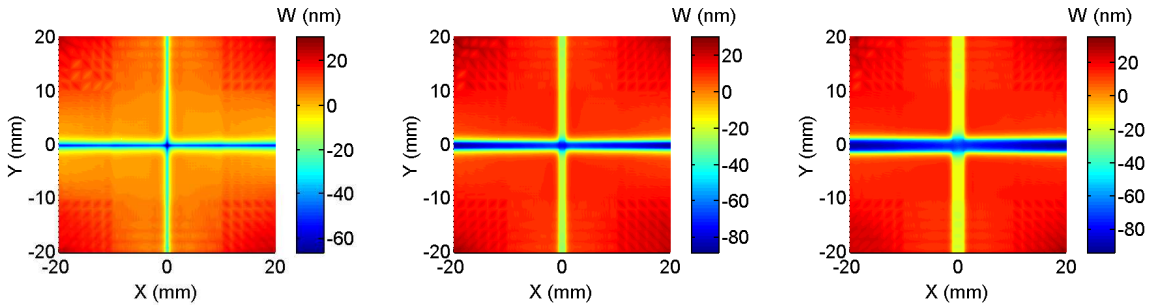

(a) (b) (c)

Figure 6.21: 8-ply substrates: Local out-of-plane deformation after bonding process for a) 0.25 mm, b) 1.0 mm, c) 2.0 mm gap widths.

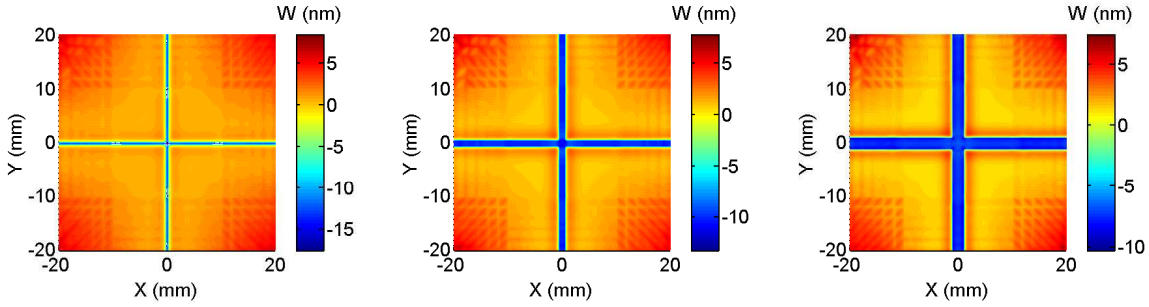

(a) (b) (c)

Figure 6.22: 16-ply substrates: Local out-of-plane deformation after bonding process for a) 0.25 mm, b) 1.0 mm, c) 2.0 mm gap widths.

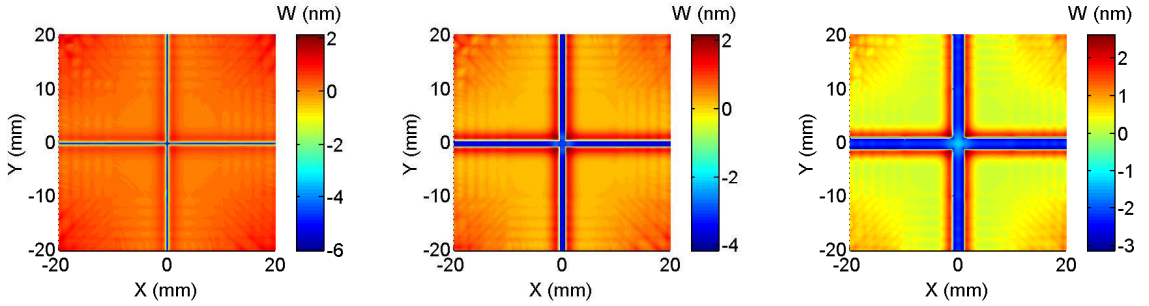

(a) (b) (c)

Figure 6.23: 32-ply substrates: Local out-of-plane deformation after bonding process for a) 0.25 mm, b) 1.0 mm, c) 2.0 mm gap widths.

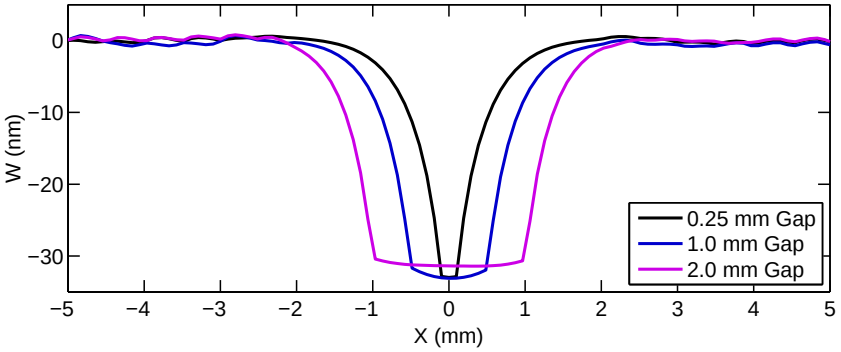

(a)

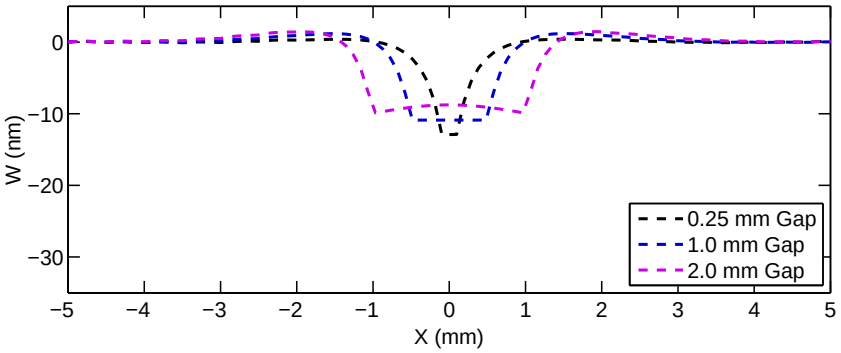

(b)

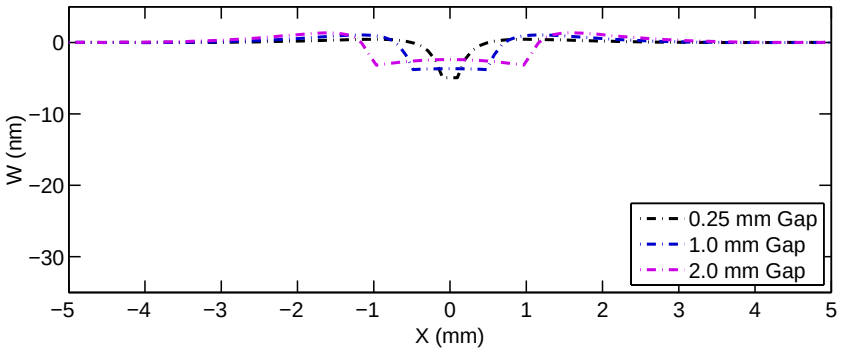

(c)

Figure 6.24: Profile of gap deformation over central portion of CFRP substrate for a) 8-ply, b) 16-ply and c) 32-ply substrates..

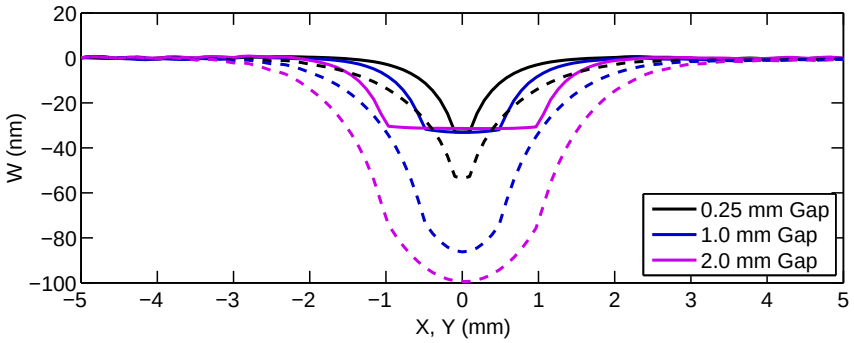

Figure 6.25: Comparison of X (solid) and Y (dashed) gap deformation profiles for 8-ply CFRP substrates.

6.5 Deformation Upon Uniform Actuation

As PZT is an active material that can exhibit in-plane strains as a function of applied electric fields, the effect of actuation on the global and local deformations is of interest to this study as well (a more detailed study on the actuation properties of the PZT material is presented in the next Chapter). To perform this study, a specific actuation example was considered where the PZT is strained uniformly in the plane. The magnitude of induced strain was chosen as 200 $\mu\epsilon$ (10^{-6} strain), roughly 2/3 of the total actuation strain for the PZT material. In the model this was imposed by assigning an "expansion" value in the material property definition of PZT and subjecting the entire assembly to a uniform temperature change. This method mimics the linear piezoelectric response of the material using a thermal expansion analog. Coupling between piezoelectric and elastic properties were not considered here.

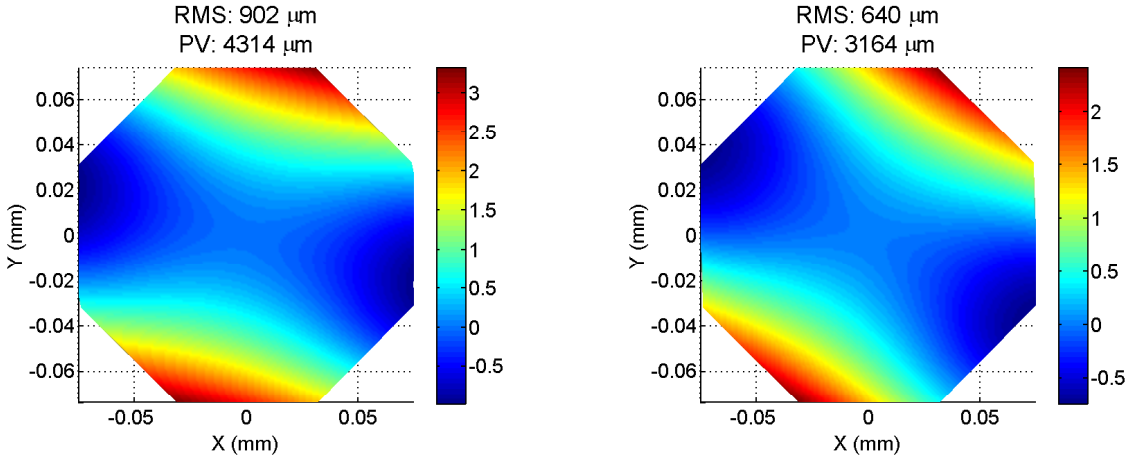

(a) (b)

Figure 6.26: 8-ply substrates: Comparison of global deformation upon actuation at 200 $\mu\epsilon$ for a) continuous PZT and b) discrete PZT patches.

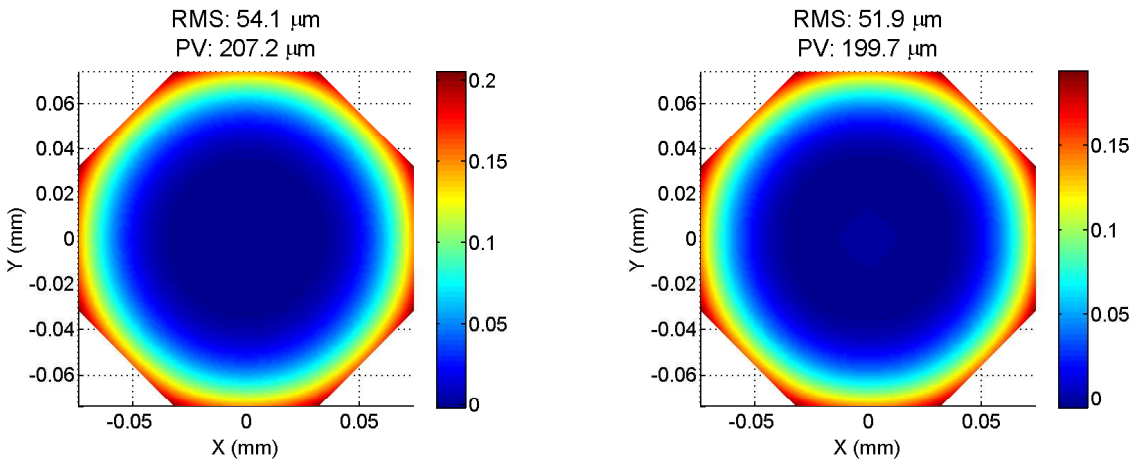

(a) (b)

Figure 6.27: 16-ply substrates: Comparison of global deformation upon actuation at 200 $\mu\epsilon$ for a) continuous PZT and b) discrete PZT patches.

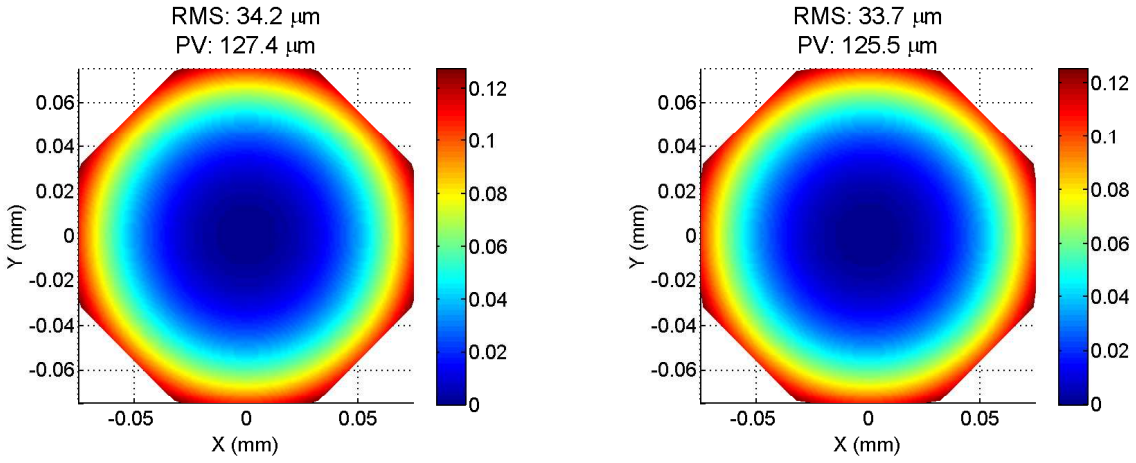

(a) (b)

Figure 6.28: 32-ply substrates: Comparison of global deformation upon actuation at 200 $\mu\epsilon$ for a) continuous PZT and b) discrete PZT patches.

Figures 6.26, 6.27, and 6.28 display the global deformation of the CFRP substrates upon actuation. It is apparent that the mode of deformation is dependent on the substrate laminate orientation. Astigmatic deformations occur for the 8-ply substrate while the 16 and 32-ply substrates exhibit spherical modes of deformation. A similar response is observed between the continuous and discontinuous cases. The sign of the spherical deformation associated with the 16 and 32-ply substrates indicates that an increase in curvature is predicted upon positive actuation.

The local deformation at the gaps after the actuation process is presented in Figures 6.29, 6.30, and 6.31

in the same manner as before. The deformation profiles at a constant y-value of 10 mm are also presented in Figure 6.32. From the results of this analysis it is apparent that with a positive actuation strain a change in sign is predicted for the local deformations at the gaps. The deformation now produces local "hills" on the front (concave) surface of the CFRP substrate. The amplitude of deformation is also significantly higher in comparison to after the bonding process. Deformations range from $\sim$ 100 nm for 32-ply substrates to $\sim$ 2100 nm for the 8-ply substrates. Symmetry between the gaps oriented in the x and y directions is predicted for the 16 and 32-ply substrates in this analysis; however, variations are again observed for the 8-ply substrates. A comparison between the deformation profiles in both directions is shown in Figure 6.33.

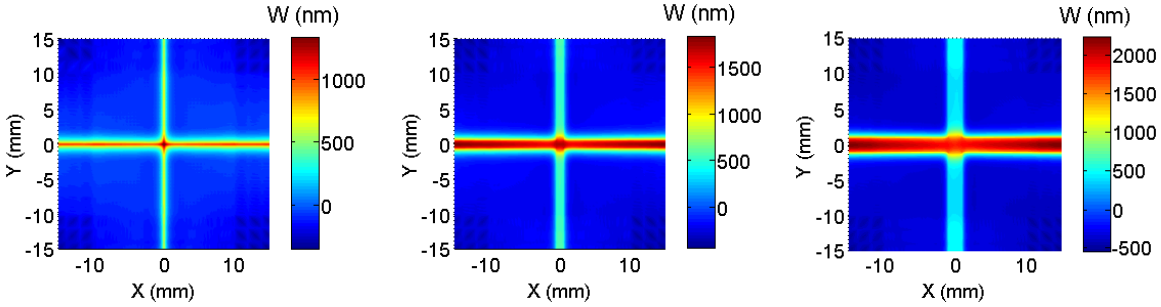

(a) (b) (c)

Figure 6.29: 8-ply substrates: Local out-of-plane deformation upon actuation at 200 $\mu\epsilon$ strain for a) 0.25 mm, b) 1.0 mm, c) 2.0 mm gap widths.

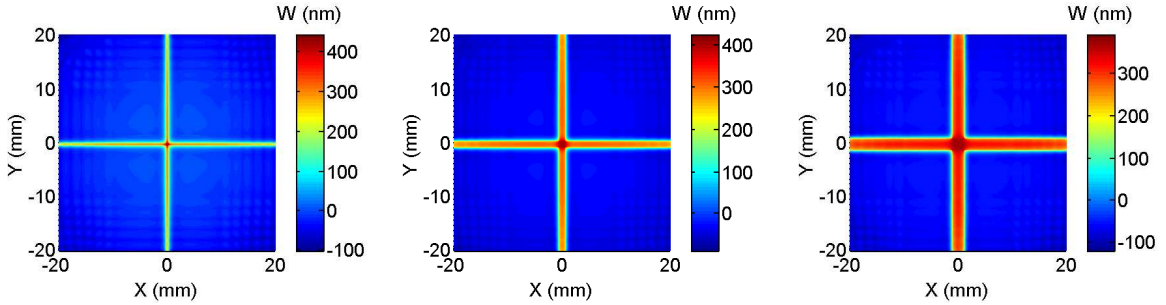

(a) (b) (c)

Figure 6.30: 16-ply substrates: Local out-of-plane deformation upon actuation at 200 $\mu\epsilon$ strain for a) 0.25 mm, b) 1.0 mm, c) 2.0 mm gap widths.

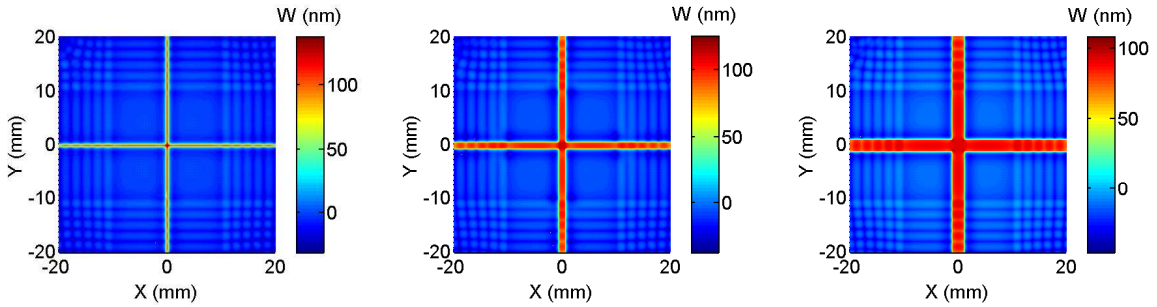

(a) (b) (c)

Figure 6.31: 32-ply substrates: Local out-of-plane deformation upon actuation at 200 $\mu\epsilon$ strain for a) 0.25 mm, b) 1.0 mm, c) 2.0 mm gap widths.

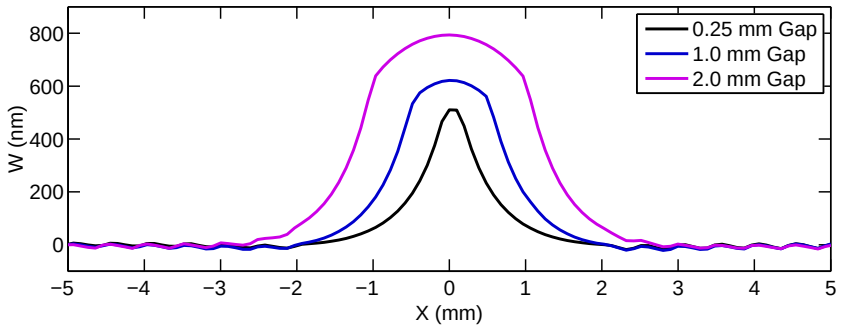

(a)

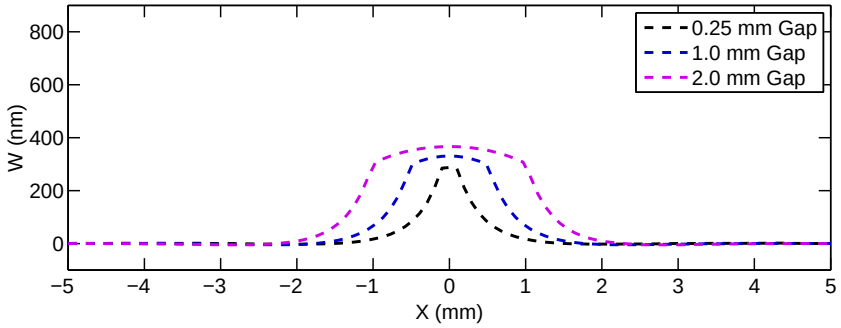

(b)

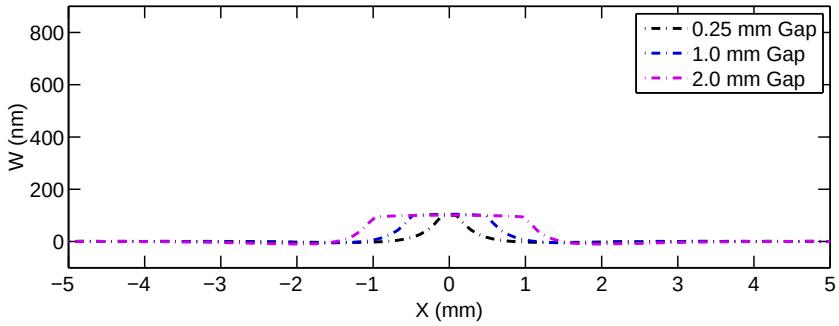

(c)

Figure 6.32: Profile of local out-of-plane deformation upon actuation at 200 $\mu\epsilon$ strain for a) 8-ply, b) 16-ply, and c) 32-ply substrates

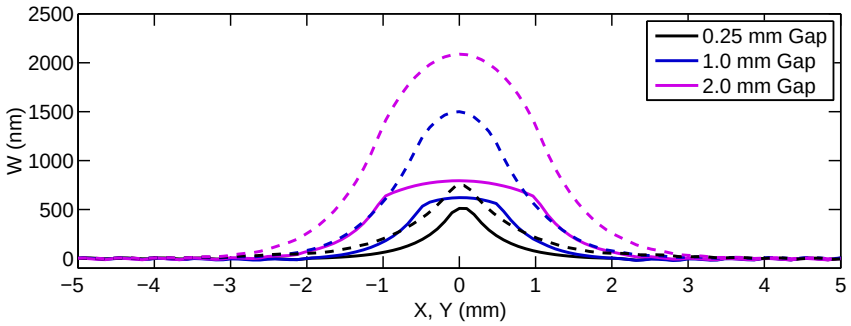

Figure 6.33: Comparison of X (solid) and Y (dashed) gap deformation profiles after actuation for 8-ply CFRP substrates.

6.6 Measurement of Cross-Pattern

Figure 6.34 is a surface measurement over the center portion of an active mirror using a white light scanning interferometer (Zygo Zemapper). The measurement was performed on an active mirror containing four PZT plates with a gap width of ~ 0.25 mm. The measurement was filtered by first removing the spherical curvature and then applying an FFT-passed high-pass Gaussian filter with a $1/10$ mm^{-1} pass frequency. A clear cross pattern is observed at the location of the PZT gaps with a large central peak in the middle. The shape of this pattern is similar to those predicted by the models above. However, positive displacements (local hills) are predicted even though the measurement was performed with no induced actuation strain in the PZT material. From the model predictions above, negative displacements (local valleys) are expected under these conditions. However, it should be noted that the measurement was performed after the mirror was subjected to several cycles of actuation. As the subsequent chapter outlines, throughout this process residual piezoelectric strains can persist in the material. Therefore, while no actuation was prescribed, the PZT may indeed be in a positive strain state with respect to its initial condition during bonding. It is believed this is the explanation for the reversal in sign.

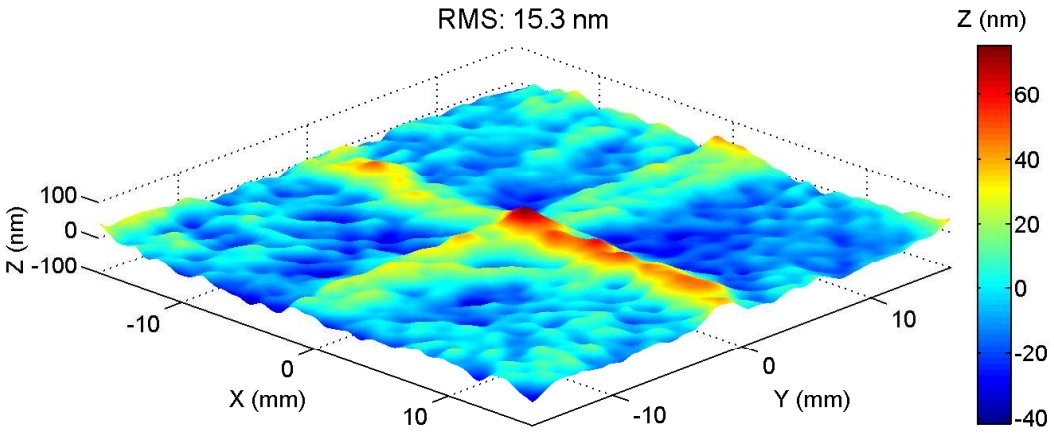

Figure 6.34: White light scanning interferometer (Zygo Zemapper) measurement of the center portion of a mirror substrate displaying evidence of the cross-pattern produced from the four discrete PZT plates.

6.7 Tessellated Active Layer

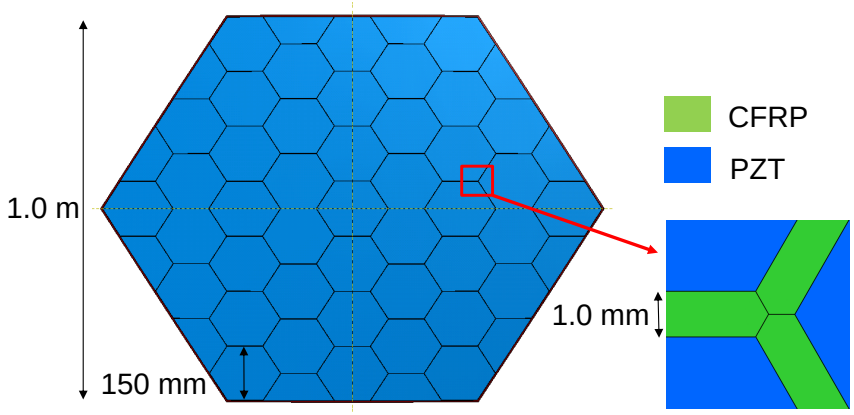

Figure 6.35: Overview of model showing a 1.0 m hexagonal mirror with 150 mm PZT patches arranged in a continuous tesselation.

The preceding analysis were implemented for mirrors of reduced diameter (150 mm) in order to match the geometry implemented for experimental efforts. 4 active plates were used to provide quasi-continuous active layer coverage over the surface of the CFRP substrate. However, larger mirrors are also of interest to this study. At meter-scale diameters, a large number of active plates must be implemented in order to provide the same continuous active layer coverage. Therefore, the above modeling techniques were implemented for a 1.0 m diameter mirror, shown in Figure 6.35. 49 individual hexagonal active layer elements, each 150 mm in diameter, are arranged in a continuous tessellation across the backside of the CFRP substrate. The

substrate geometry was switched from the previous octagonal shape to the hexagon shown here in order to accommodate the tessellation. A 16-ply substrate is implemented for this analysis with a 10.0 m spherical radius of curvature.

To assemble such a structure it would be necessary to deform each initially flat active plate to the surface of the curved CFRP substrate. From Section 6.4.1 it was demonstrated that this resulted in figure errors after the two elements were bonded together. However for this case the radius of curvature, R, is much higher than in the previous studies (R = 10.0 m vs. 2.0 m). With this geometry the bending stresses will primarily dominate over the non-linear mid-plane stresses as shown in Figure 6.10. Also, from the results displayed in Figure 6.15 and Figure 6.18 it is expected that the magnitude of the resulting figure deformation would be in the form of a low-amplitude uniform curvature change. Therefore, for this analysis, the deformation associated with the bonding process is neglected. This mimics the possible situation where each active layer is initially curved, having a matching radius of curvature to that of the CFRP substrate.

The figure deformations produced upon uniform actuation of the active elements is studied in detail here. Specifically, the mid-spatial frequency errors produced due to the discontinuous nature of the active layer as well as the high-spatial frequency deformations caused by the gaps between each active element are considered. Uniform 1.0 mm gaps are implemented for this study as shown in Figure 6.35. The active elements are actuated to a strain level of 200 $\mu\epsilon$ strain as in the previous studies. As shown in Figure 6.36(a), a near uniform curvature change is achieved upon uniform actuation of the active layer. However, if the resulting deformation is filtered and the low-spatial frequency errors are removed, higher-order deformations are observed. This was performed by projecting the shape onto a set of Zernike polynomials [20] and then removing those of lowest order. Zernike polynomials are only valid over a unit circle and therefore they are truncated here in order to conform to the hexagonal shape. Figure 6.36(b) displays the figure deformation after removal of the first 36 Zernike modes. Deformations, local to each active element location are observed across the entire surface of the mirror.

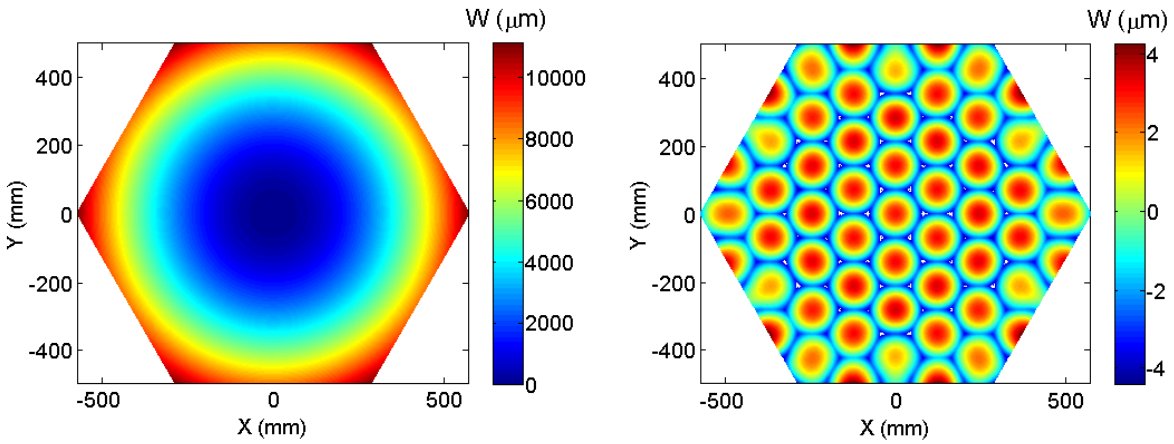

(a) (b)

Figure 6.36: Figure deformation due to uniform actuation (200 $\mu\epsilon$ strain). a) Base curvature change, and b) shape after removal of the first 36 Zernike modes.

Features such as these are also observed in [54] for mirrors of a similar design. It was shown that the magnitude of such deformations is directly proportional to the size of each active element and inversely proportional to the gap width. Therefore, small active elements arranged in a closely packed pattern are predicted to produce the minimal amount of deformation. However, the highly-localized deformations due to the gaps were not studied in [54]. Figure 6.37 displays these local deformations across the central portion of the mirror. The same techniques were used as in Section 6.4.3 in order to unveil these features. Print-through of the hexagonal tessellation is predicted with peak-to-valley magnitudes of ~ 220 nm. With smaller active elements there will be an increased number of gaps and these features will persist across a larger area. Therefore, a trade between figure errors of varying spatial-frequencies must be taken into consideration.

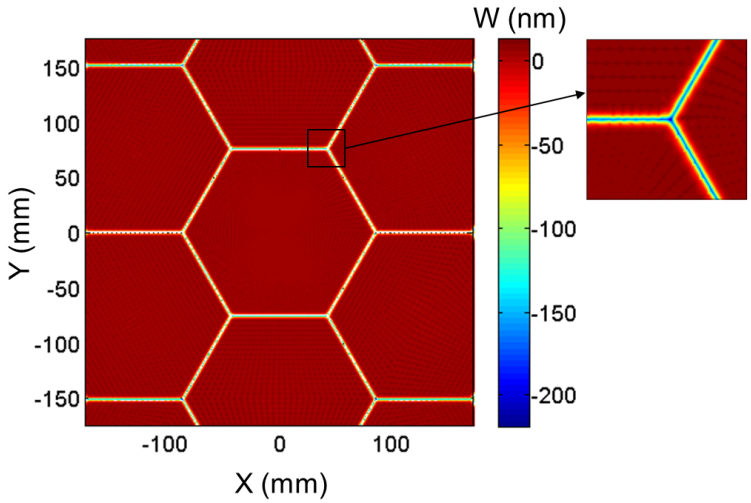

Figure 6.37: Local deformations at gap locations due to uniform actuation (200 $\mu\epsilon$ strain).

6.8 Transverse Shear Effects

The preceding analyses implemented conventional shell elements (S4R) to study the deformation associated with the bonding process and actuation of discrete PZT patches. S4R elements are considered general-use elements in that they can accurately capture the behavior of shells of various thicknesses, material properties, and boundary conditions. They are especially good at capturing the bending behavior of shells. However, their capability to accurately capture transverse shear deformations is limited. The shear stiffness of conventional shell elements is formulated based on the overall shell definition (i.e., laminate orientation and material properties). In doing so, through-thickness changes in the shear modulus of each ply are not considered. With this formulation a substrate with a symmetric laminate definition will have identical shear response along the principal directions in the laminate coordinate system. In addition to this, the deformation of conventional shell elements is defined entirely by the shell reference surface. Therefore, through-thickness variations in deformations due to transverse shear effects will not be captured. This enforces the condition that mid-plane normals remain straight throughout deformation.

For fiber-reinforced composites there is a vast difference in material properties parallel and perpendicular to the fiber direction. The modulus in these direction differs by a factor of 57 as shown in Table 6.3. A difference in transverse shear stiffness in the direction of the fibers (G13) vs. perpendicular to the fibers (G23), is also present. Therefore, it is expected that ply-level shear deformations are likely to occur. This is of great importance when considering edge effects or discontinuities in thickness such as with the local deformation at the gaps between PZT plates. A large body of literature exists pertaining to the shear deformation of composite plates [55, 56, 57, 58, 59]. However, the majority of these studies are concerned with accurate modeling of ply-level stresses due to uniform loading conditions. Local deformations are not as great of concern. The effect of thickness discontinuities has also been studied [60, 61, 62], however the majority of the efforts focus on implementing custom elements in order to capture stress singularities.

The method implemented here is to model the CFRP substrate and PZT plates using continuum shell elements (SC8R). Continuum shell elements are 3D, 8-node elements that model the actual thickness of the shell instead of defining a reference surface. Each node within the element has displacement DOFs only. However, the advantage here is that multiple elements can be implemented through the thickness of the shell. By incorporating an increased number of DOFs through the thickness, initially straight surface normals need not remain straight due to the unique deformations of each element. In the present study, this allows for more accurate modeling of the ply-level shear deformations in the CFRP substrates upon actuation of the PZT plates.

The transverse shear stiffness in the fiber direction, G13, is assumed to be identical to the in-plane shear stiffness, G12, due to the transversely isotropic nature of the material. Assumptions were also made on the transverse shear stiffness perpendicular to the fiber direction, G23. Following that from [63], G23 can be

predicted through the following relation:

$$G23 = \frac{E2}{2(1+\nu_{23})}. \tag{6.16}$$

As ν_{23} was not measured for the present study, assumptions were made on its magnitude and a value of 0.5 was used [64]. This results in a value of 2.0 GPa for G23.

A specific example was used to study the effect of transverse shear on the local deformation at the gaps. The study considered the central portion of a 16-ply CFRP substrate and four PZT plates with a gap width of 0.25 mm. Figure 6.38 provides an overview of the model. Each ply within the CFRP substrate is modeled with a unique continuum shell element. The PZT plates were modeled with 3 through-thickness elements. An in-plane element size of 62.5 μm was used to model the gaps and the surrounding areas. 200 μm wide elements were implemented for the rest of the model. For simplicity, only the deformation after actuation was considered here. This was performed as the deformations due to actuation were approximately two orders of magnitude higher than those obtained from the initial bonding process. In addition, both the CFRP substrate and PZT plates were modeled as initially flat and therefore it is assumed that the initial curvature of the CFRP substrate does not affect the local deformation at the gaps upon actuation.

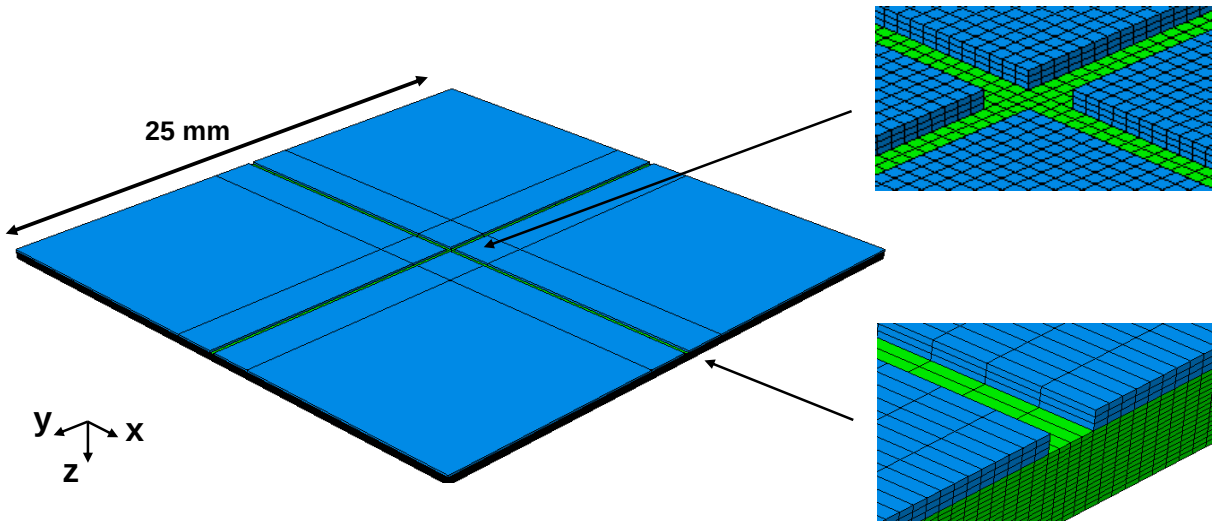

Figure 6.38: Overview of continuum shell model used to capture transverse shear deformations.

6.8.1 In-Plane Deformation

Figure 6.39 displays the deformation in the x and y directions (U and V, respectively) at cross-sections near the gaps (X, Y = 2.5 mm). The interface of the CFRP and PZT materials is set as the z = 0 surface. By comparing the results it is apparent that there is a differing response between the U and V deformations. Highly localized in-plane deformations of the interface ply are observed in the y direction but not in the x

direction. This is a direct consequence of the fiber orientation of the interface ply and the associated variation in stiffness. The y-direction is perpendicular to the fiber direction of the interface ply and therefore both the in-plane and shear stiffness are much lower in this direction. It is therefore evident from this result that initially straight mid-plane normals do not remain straight throughout the actuation process. This effect is not captured using conventional shell elements.

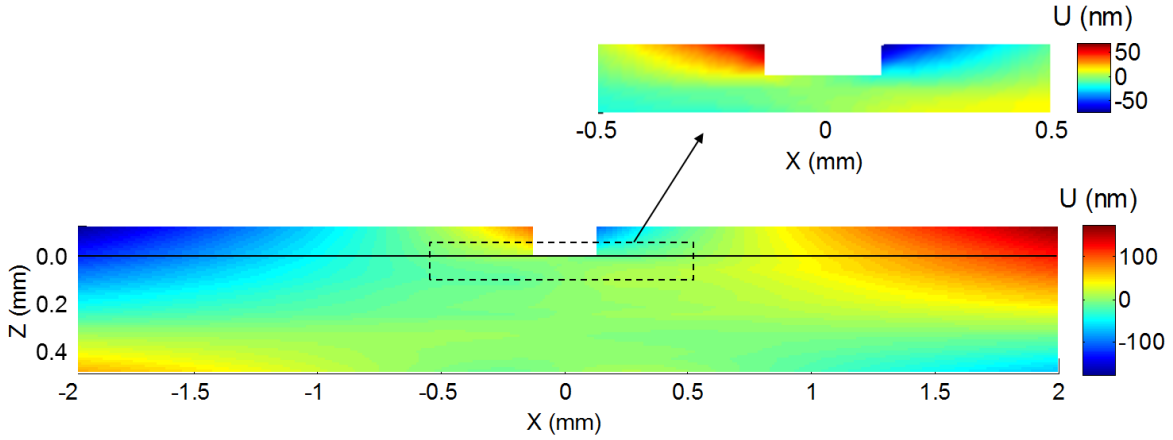

(a)

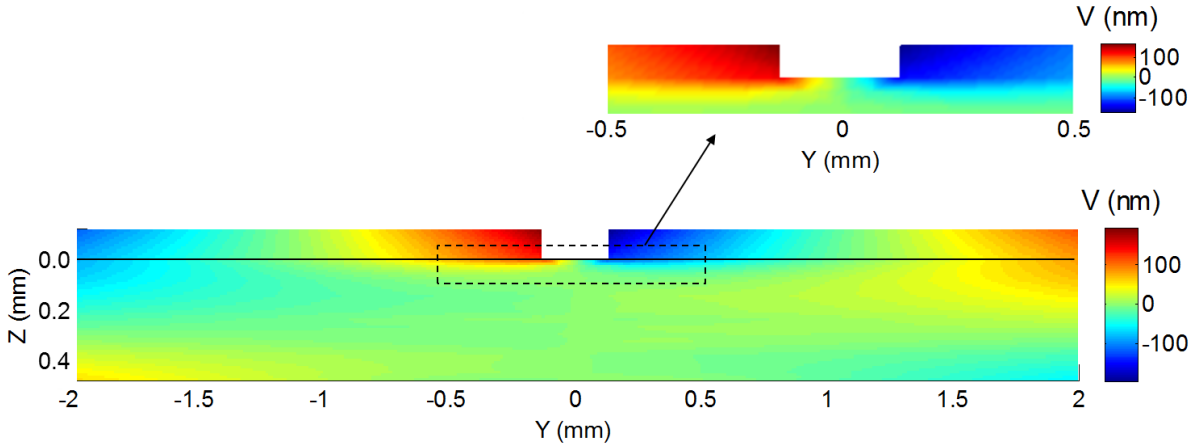

(b)

Figure 6.39: In-plane deformation in a) x-direction and b) y-direction due to actuation.

6.8.2 Out-of-Plane Deformation

Figure 6.40 compares the resulting out-of-plane deformation of the bottom surface of the CFRP substrate at the gap locations implementing conventional and continuum shell elements. The conventional shell element model predicts a symmetric response for the gaps oriented in the x and y directions while the continuum shell model predicts a higher level of deformation in the gap oriented in the y direction, perpendicular to the interface ply direction. The differing amplitude of deformation is a direct result of the local transverse shear

deformation and the decreased stiffness perpendicular to the fiber direction. In this direction the y-component of the actuation strain is transferred to the CFRP substrate as a highly local in-plane deformation in the interface ply. In the x-direction, the actuation strain acts to distort the CFRP substrate through bending. A comparison of the deformation profiles is presented in Figure 6.41.

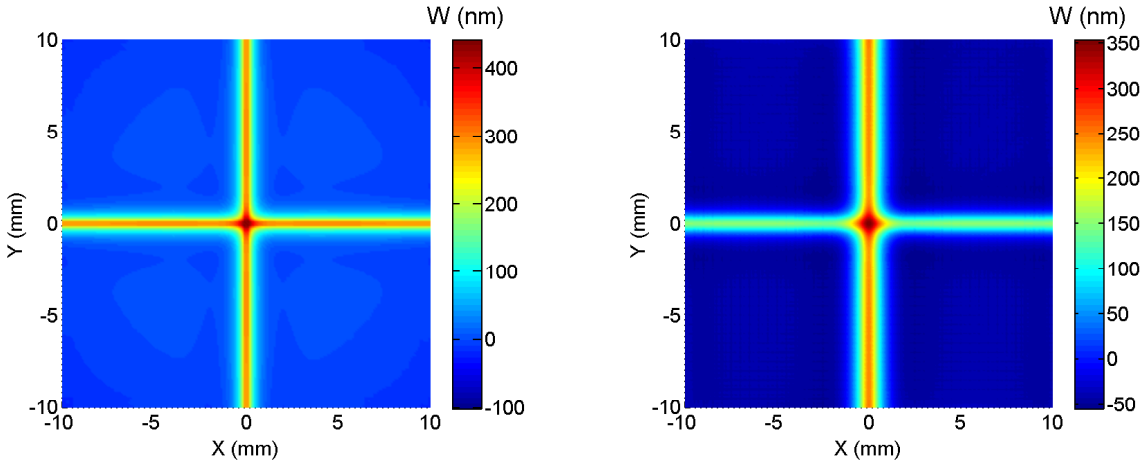

(a) (b)

Figure 6.40: Continuum shell element model displaying out-of-plane deformation due to uniform in-plane actuation of the PZT at 200 $\mu\epsilon$ strain.

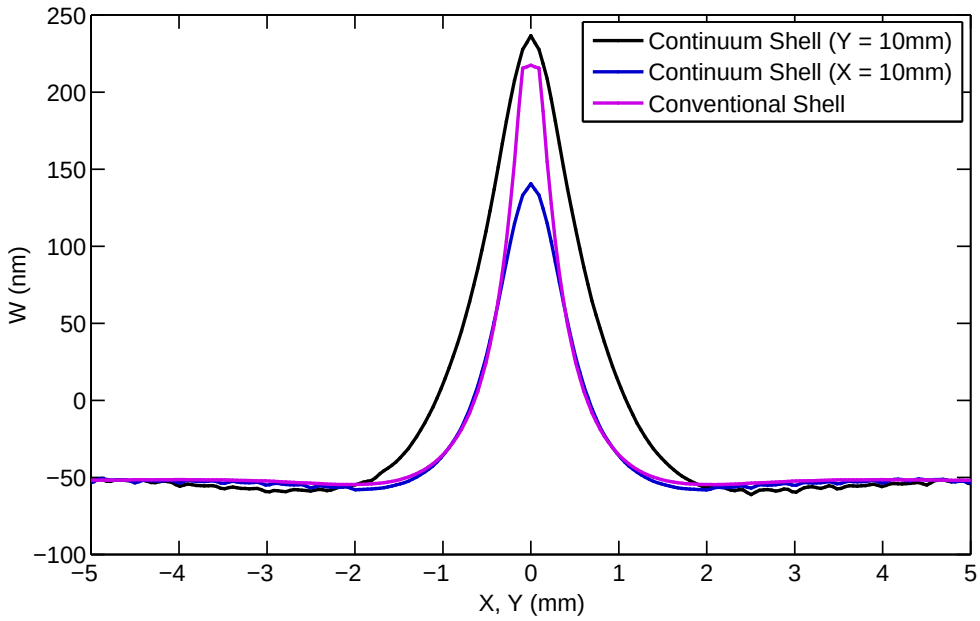

Figure 6.41: Constant x and y deformation profiles due to 0.25 mm gap over central portion of CFRP substrate. Comparison between continuum and conventional shell models.

6.9 Discussion of Results

The results of this study indicate that significant global and local shape deformations occur as a result of bonding multiple flat PZT plates to initially spherical CFRP substrates. Simulations were performed for 8, 16, and 32-ply substrates corresponding to thicknesses of 240, 480, and 960 μm. The PZT plates were fixed at 125 μm thicknesses. Significant variations in the mode and amplitude of global deformation were observed as a result of the simulated bonding process when considering a continuous PZT sheet vs. discrete plates. While lower in amplitude, the deformation imposed by discrete plates takes on a higher-order mode. It was demonstrated that this is a direct consequence of the large mid-plane stresses associated with large Gaussian curvature changes. This mode of deformation was also observed experimentally for an 8-ply CFRP substrate with four PZT plates. Furthermore, relatively low amplitude but high spatial-frequency deformations are predicted at the gap locations between PZT plates. It was observed that the amplitude of this deformation was relatively insensitive to the gap width; however, a significant dependence on the CFRP substrate thickness was observed. Near complete mitigation of the gap deformation was observed for 32-ply substrates.

The deformation induced by uniformly actuating all PZT plates was studied as well. Through the results obtained from the global deformation study it was observed that the discrete patches produced similar deformations in comparison to the continuous sheet. However, the high-spatial frequency errors at the gap locations increased significantly upon actuation. In this analysis, the gap deformations increased by two orders of magnitude from the initial bonding process. A relatively weak dependence on the width of the gap was observed with lower amplitudes predicted for small gap widths. The thickness of the substrate had a significant impact on the amplitude of deformation with peak-to-valley deformations at $\sim$100 nm for the 32-ply substrates. However for the application of active mirrors, this is still a relatively high amplitude error. Therefore, limitations on the magnitude of induced strain in the PZT may be necessary. Design considerations such as filling the gap to aid in the transfer of actuation strain could be considered as well.

A measurement of the local deformation at the location of the PZT gaps was performed using white-light scanning interferometric techniques. A clear cross-pattern was evident in the measurement, indicating that the highly localized deformation due to the gaps is indeed present. The sign of the deformation was opposite to that predicted by the models; however, it is believed this is due to residual strains in the PZT material upon many cycles of actuation.

A brief study was also performed in order to study the effects of tessellating multiple active elements across the backside of a 1.0 m dia. mirror. It was found that under uniform actuation of the plates, deformations local to each active element were produced. These deformations are in agreement with results presented in the literature. In these studies it was demonstrated that the magnitude of these deformations decreased for as the size of each active layer decreased. However, the present study demonstrated that the highly-localized deformations at the gap locations must also be taken into consideration.

Finally, the effect of transverse shear deformations on the gap deformation imposed by actuation was

studied for 16-ply substrates. Continuum shell elements modeling each ply of the CFRP substrate were implemented in place of conventional shell elements with a single reference surface definition. Large magnitude in-plane deformations were observed in the ply located at the interface of CFRP substrate and PZT plate. The out-of-plane deformations at the gap locations were predicted to vary depending on the fiber direction as well. Higher amplitude deformations were predicted for the gap oriented perpendicular to the interface fiber direction as the actuation strain is transferred predominantly through bending in this orientation.

Chapter 7

Actuation Response

This section provides an overview of the actuation process used to correct figure errors. A description of the considered active materials along with a characterization of their actuation capabilities is presented. An analysis used to size the thickness of the active material relative to the CFRP substrate is also outlined. Finally, a description of the shape error correction process as well as simulation predictions on the performance of various active mirror designs is presented.

7.1 Active Materials

Piezoelectric and electrostrictive ceramics were chosen as candidate active materials due to their high stiffness, large actuation capabilities, and availability in thin-film form. These materials have been used extensively for structural sensing and actuating applications [65, 66, 67, 14].

7.1.1 Piezoelectric Ceramics

Piezoelectric materials are a class of materials that exhibit coupling between electric fields and mechanical strains [68]. For the present study piezoelectric ceramics are implemented, specifically Lead-Zirconate-Titanate (PZT). Figure 7.6 displays the tetragonal lattice structure of PZT. Due to the non-centrosymmetric arrangement of the lattice, a charge separation is created by the positively charged zirconium/titanium ions and negatively charged oxygen atoms. Therefore, a net dipole moment is present in the lattice. A collection of lattice structures containing the same sense dipole moments is defined as a piezoelectric domain. In its base state, the domains throughout the piezoceramic will be randomly oriented and thus there will be no net polarity in the bulk materials, as shown in Figure 7.2(a). However, under the application of a strong electric field the piezoelectric domains will orient themselves in the direction of this field, as shown in Figure 7.2(b). Upon removal of the electric field, a remnant polarization is realized (Figure 7.2(c)). With the subsequent application of electric fields at magnitudes lower than the poling field, the material will strain as the central Zr ion is displaced within the lattice, causing it to distort. This is known as the "converse piezoelectric effect" with the "direct piezoelectric effect" defined as the opposite process (electric fields produced as a

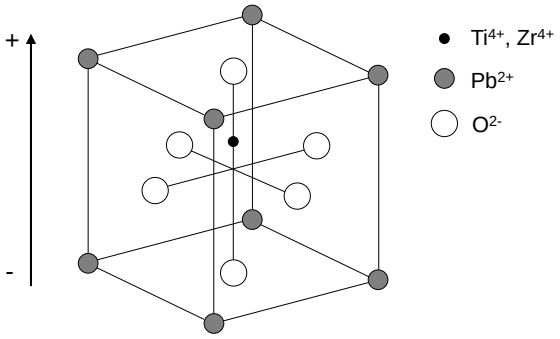

Figure 7.1: Non-centrosymmetric attice structure of PZT displaying dipole direction.

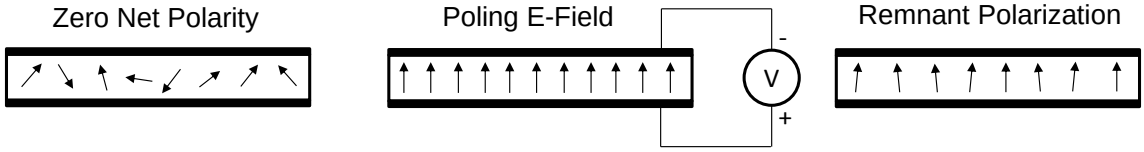

(a) (b) (c)

Figure 7.2: a) Random domain orientation before poling. b) Orientation of domains through poling electric field. c) Remnant polarization after removal of poling field.

function of lattice deformations).

The magnitude of coupling between the directional strains and applied electric field are defined through the piezoelectric constants of the material, **d**. By convention, the d33 component is defined as the strain produced in the polarization direction under the application of an electric field in that same direction. The d31 component describes the relation between strains produced normal to the polarization direction due to an electric field aligned with the polarization direction. Due to symmetry, d32 = d31. For a flat plate and defining the 1 and 2 directions in the plane and 3 through the thickness, the d31 component describes the relation between an applied through-thickness electric field and the resulting in-plane strain (assuming polarization through the thickness).

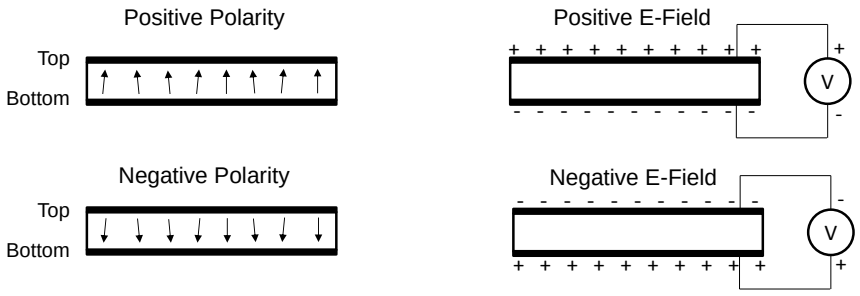

Figure 7.3: Directional convention for domain polarization and electric field.

For convenience it is desired to define a sign convention associated with the polarization direction and applied electric fields. The convention used here is that a positive polarization direction indicates that the domains are oriented pointing to the top-surface of the plate. A negative polarization direction indicates that the domains are pointing down towards the bottom surface. A positive applied electric field is one that has a positive potential at the top surface while a negative field is one with a positive potential at the bottom surface. This convention is shown schematically in Figure 7.3.

The actuation properties of PZT-5A were characterized using Digital Image Correlation (DIC). Specifically, the d31 effect was determined by measuring in-plane strains as a function of applied through-thickness electric fields. The measurements were performed with the sample lying flat on a Teflon film in order to reduce frictional effects. Conductive electrodes on the top and bottom surface of the samples allowed for the through-thickness electric field to be applied via a high-voltage amplifier and waveform generator. A sinusoidal signal with a period of 30 seconds was implemented.

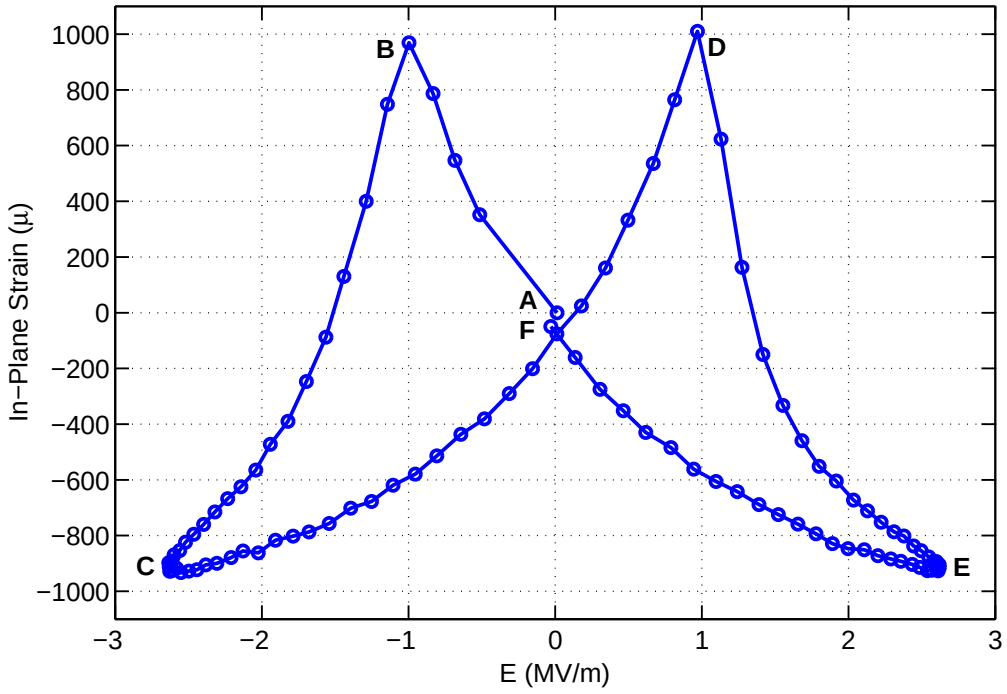

Figure 7.4: Measured in-plane strain of PZT-5A displaying domain switching due to high electric fields.

Figure 7.4 displays the measured in-plane strain of PZT-5A through the application of high electric fields. The measurement was performed on a 190 μm thick substrate and the voltage amplitude was set to $\pm$ 500 V. The response of the material under these conditions is referred as the "full-field" response as the applied electric fields are high enough to capture the piezoelectric behavior of the material in its entirety.

Several points have been identified in Figure 7.4, labeled A-F. The material starts out at point A in its base state with no applied electric field. In this state, the material is poled in the positive direction. Through the application of a negative electric field (i.e., against the polarization direction), the material exhibits a positive value in-plane strain. The magnitude of this strain is directly proportional to that of the applied voltage. Upon further application of this electric field, the material will begin to approach point B. At this point, the electric field is high enough to cause a complete reversal of the piezoelectric domains within the material. At the microscale, a snap-through instability occurs where the central ions of each lattice structure suddenly shifts into its new equilibrium state at 180° from the original location. Macroscopically this occurs nearly all at once, reversing the domains across the entire substrate. This is evident by the sharp change in strain at point B. Upon further application of voltage from this point, the strain begins to decrease due to the reversal of the domain direction. Now the material will exhibit a negative-valued strain as a function of a negatively applied electric fields. Approaching point C, the actuation begins to saturate and a lower magnitude of induced strain is realized for increased levels of applied electric field. Upon reversal of the electric field, the material returns to a near-zero strain state; however, due to the domain switching, it

possesses a reversed sense polarity. The full-field response of the material is symmetric as evident by the similar behavior displayed at points D, E, and F but in the opposite direction. Due to its characteristic shape, Figure 7.4 is known as the "Butterfly Curve" of the material.

Figure 7.4 displays the fact that care must be taken when actuating the material as a reversal in actuation behavior can occur if the magnitude of electric field applied against the polarization direction is too great. Therefore, operating limits on the applied electric field must be set. For the present study this was set at 80% of the domain-reversing electric field. For PZT-5A this corresponds to an electric field range of ± 0.8 MV/m.

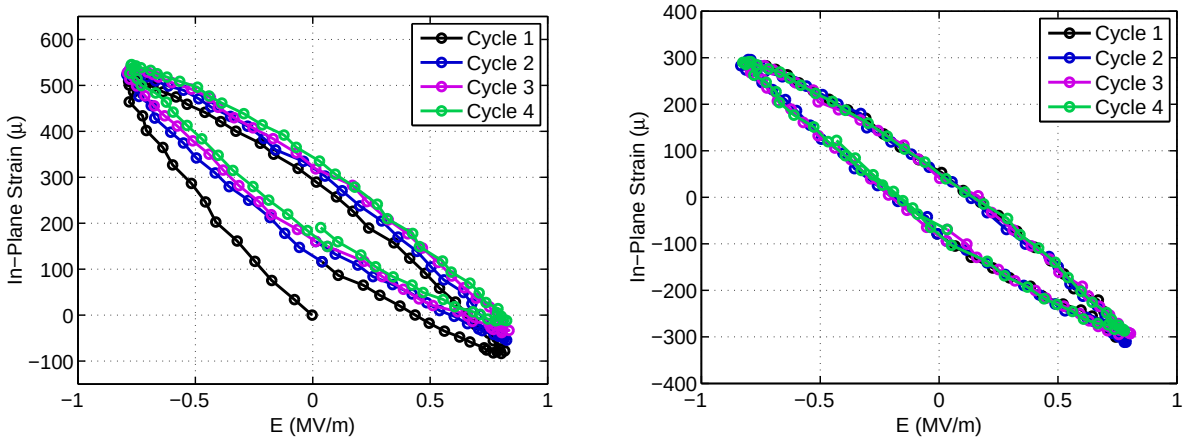

(a) (b)

Figure 7.5: Measured in-plane strain of PZT-5A over operating electric field range (± 0.8 MV/m). a) Response of material directly after poling showing accumulation of strain and b) centered data after multiple cycles showing a repeatable but hysteretic response.

The response of the PZT-5A material over the operating electric field range is plotted in Figure 7.5. Two conditions are presented here. The first, presented in Figure 7.5(a), presents the actuation strain associated with the first four cycles directly after poling the material. It is apparent through the upward drift in the strain values that a remnant amount of strain accumulates in the material upon cycling. This is primarily due to gradual domain reorientation, where a small number of domains will switch polarity until they reach their final equilibrium state [68]. After four cycles, a remnant strain of approximately 200 μ is observed. It should be noted that this effect is also observed if the material is held at a constant electric field for a period of time or subjected to mechanical stresses.

If the material is actuated for a larger number of cycles, the accumulation of strain begins to disappear, as shown in Figure 7.5(b). It is also apparent that the free-strain actuation profile is repeatable over multiple cycles. However, a large amount of hysteresis is present in the material as demonstrated through the loading/unloading electric field paths. A difference of 150 μ is observed at the zero electric field location

after only one half cycle is complete. However, the material is observed to return to its initial state repeatedly if a full cycle is performed. Therefore, if it is desired to have the material return to the same strain/electric field state a "refresh" cycle should be performed where the electric field is applied to its full extent before returning to the desired value.

As the actuation response is non-linear, characterization of the d31 coefficient becomes a matter of preference. Here it is taken as the full-scale strain range divided by the full-scale electric field. With this formulation the measured d31 component is -375 pC/N. It should be noted that this is approximately 1.75 times the reported value from the manufacturer.

7.1.2 Electrostrictive Ceramics

Electrostrictive materials are another class of materials that undergo deformations as a function of applied electric fields. However, the mechanism by which this is performed is different than that for piezoelectric materials. Electrostrictive materials contain centrosymmetric lattice structures (Figure 7.6) and therefore display no remnant polarization in their base state. However, with the application of an electric field, domains orient themselves in the direction of the applied field (Figure 7.7). This produces an elongation of the lattice structure in the direction of the field and a contraction perpendicular to the field. Unlike piezoelectrics, a reversal in the direction of applied electric field does not reverse the sign of the strain, and therefore the material can only exhibit one direction of actuation. Also, unlike piezoelectric materials, imposed mechanical strains do not produce electric fields.

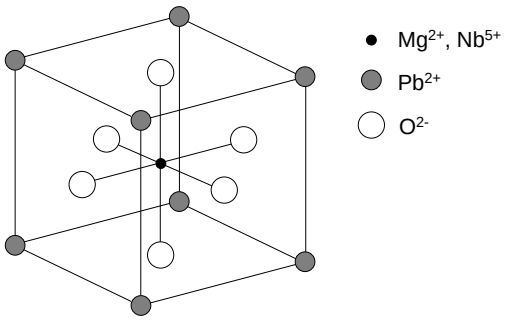

Figure 7.6: Centrosymmetric lattice structure of PMN-PT.

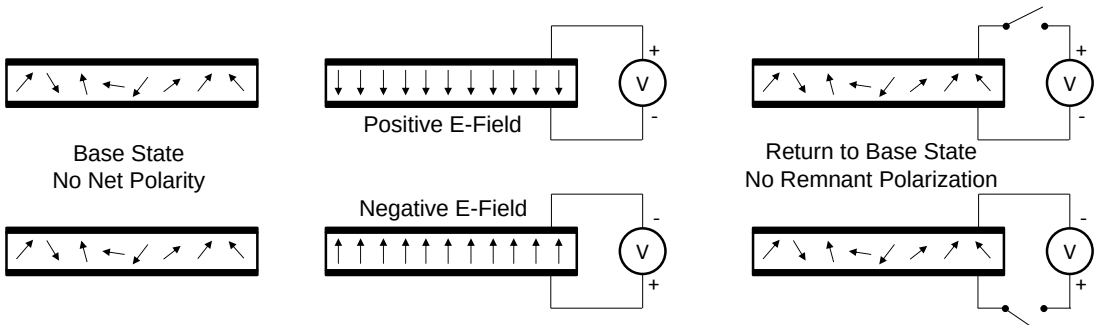

Figure 7.7: Schematic of electrostrictive domain orientation. a) Random domain orientation in base state. b) Spontaneous orientation due to applied electric field. c) Return to base state and random domain orientation upon removal of electric field.

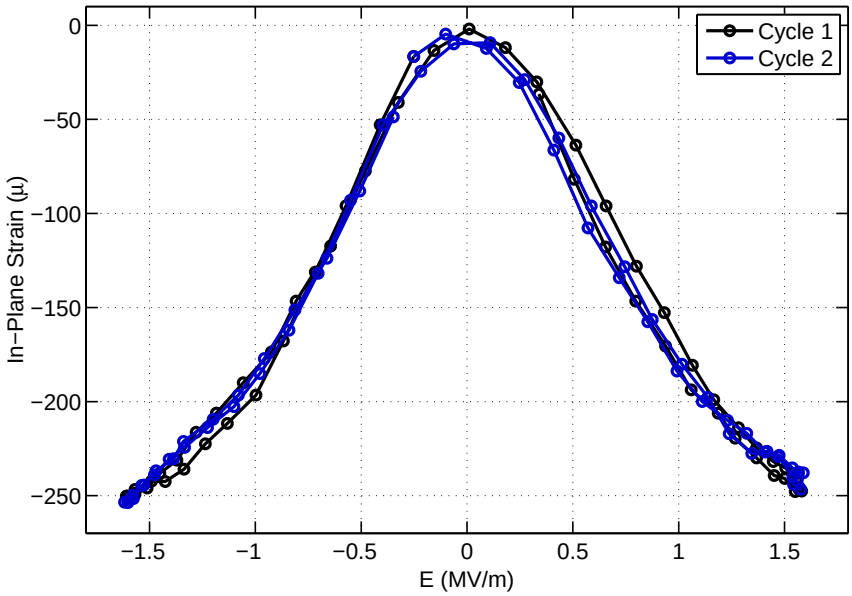

Figure 7.8: Measured in-plane strain of PMN-PT over operating electric field range.

Figure 7.8 displays the actuation characteristics of the PMN-PT material. The test was performed on a 125 μm thick flat plate of PMN-PT in the same manner as that for the PZT-5A material. The voltage was applied in a sinusoidal fashion with an amplitude of $\pm$ 200 V and a 30s period. It is apparent from the results that the response is greatly different than that of PZT. Firstly, the sign of the in-plane strain is observed to be irrespective of the direction of applied electric field, as negative strains are measured across the entire voltage range. Second, the actuation strain is observed to vary non-linearly with respect to electric field for low field values ($<$ 0.25 MV/m). The response then transitions into an approximately linear regime for

mid-range fields (0.25 - 1.0 MV/m) and finally another non-linear region is predicted at high fields (> 1.0 MV/m) as saturation begins to occur. The measured d31 coupling coefficient, defined here as the response of the material in the linear regime (between 0.25 and 0.8 MV/m), is approximately -220 pC/N. A maximum strain value of -250 μ is achievable through high electric fields. This is a factor of $\sim$ 3.5 less than the full-scale actuation range associated with PZT-5A.

The most noteworthy distinction of PMN-PT in comparison to PZT is the lack of hysteresis in the material. Both the loading and unloading paths are near identical in the free-state. Therefore, actuation can be considered a unique-valued problem. This is highly advantageous for precision actuation applications.

PZT-5A was used almost extensively in the design of the active mirror concept and therefore the following studies will incorporate it exclusively. While PZT exhibits significant non-linear and hysteretic behavior, the large actuation capabilities and bidirectional response are advantageous over PMN-PT.

7.2 Surface Parallel Actuation Scheme

In order to minimize the overall thickness of the mirror, a surface-parallel actuation scheme is implemented. In this scheme, depicted schematically in Figure 7.9, a layer of active material is integrated onto the back surface of the mirror. Using the d31 actuation mechanism mentioned above, the active material will strain within the plane under the application of a through-thickness electric field. As the active material is bonded to the CFRP substrate this ultimately produces an out-of-plane curvature change in the entire structure.

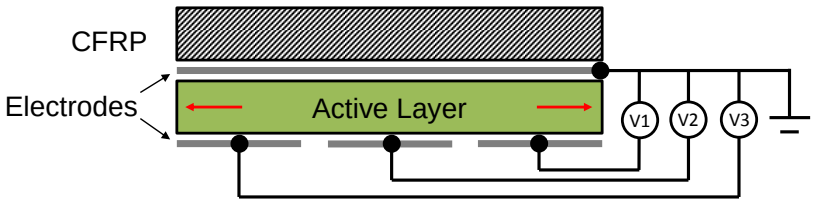

Figure 7.9: Schematic of surface-parallel actuation scheme.

7.2.1 Sizing of Active Layer

As the mirrors are extremely thin the thickness of the active layer is of particular importance as small changes in this value can have a large impact on the actuation capabilities. If the active layer is too thick it will begin to dominate the flexural stiffness of the mirror, while if it is too thin sufficient actuation authority will not be realized. To determine the optimal thickness of the active layer a linear analysis based on Classical Lamination Theory (CLT) was performed. Using CLT the resulting curvatures produced by uniformly actuating the entire active layer can be determined. These actuation curvatures, $\boldsymbol{\kappa}$, can be determined using

$$\begin{bmatrix} \boldsymbol{\epsilon} \\ \boldsymbol{\kappa} \end{bmatrix} = \begin{bmatrix} \mathbf{A} & \mathbf{B} \\ \mathbf{B} & \mathbf{D} \end{bmatrix}^{-1} \begin{bmatrix} \mathbf{N_{piezo}} \\ \mathbf{M_{piezo}} \end{bmatrix} \tag{7.1}$$

where

$$\mathbf{N_{piezo}} = \int_{z_{act,bot}}^{z_{act,top}} \mathbf{Q_{act}} \mathbf{d_{act}} E dz \tag{7.2}$$

$$\mathbf{M_{piezo}} = \int_{z_{act,bot}}^{z_{act,top}} \mathbf{Q_{act}} \mathbf{d_{act}} E z dz. \tag{7.3}$$

ABD is the overall stiffness matrix of the mirror laminate, $\mathbf{Q_{act}}$ is the orthotropic stiffness matrix of the active material, $\mathbf{d_{act}}$ is an array of the piezoelectric coupling coefficients for the active material, $z_{act,top}$ and $z_{act,bot}$ are the top and bottom coordinates of the active material with respect to the mid-plane of the overall laminate, and E is the applied through-thickness electric field. With this formulation the maximum out-of-plane curvature change can be determined as a function of the thickness ratio between the active layer and substrate layer defined as

$$t^* = \frac{t_{active}}{t_{CFRP}}. \tag{7.4}$$

The three laminate orientations defined in Chapter 4 with 8, 16, and 32-plies corresponding to thicknesses of 240, 480, and 960 μm were considered for this study. The active layer is assumed to be PZT-5A. The results of the study are shown in Figure 7.10.

The active layer thickness has a significant effect on the maximum attainable curvature change. For small active layer thicknesses ($t^* < 0.1$) there is an approximately linear increase in actuation capabilities as a function of active layer thickness. However, as the active layer becomes thicker, the incremental change in curvature begins to decrease. At specific t^* values for each laminate, a decrease in actuation performance is observed as the flexural stiffness of the active layer begins to dominate. This occurs at t^* values of 0.52, 0.6,6 and 0.70 for the 8, 16, and 32-ply substrates, respectively. Therefore, if the objective is to maximize actuation capabilities the mirrors should incorporate these thickness ratios. However considerations related to mass should be kept in mind, as PZT is an extremely dense material (ρ = 7800 kg/m^3). Thick active layers will significantly increase the areal density of the mirror. Therefore, for the current effort 125 μm thick PZT was used for all designs. At this thickness, optimal actuation properties are predicted for the 8-ply design. The 16-ply design is predicted to operate at 90% of the optimal value and the 32-ply design at 43%.

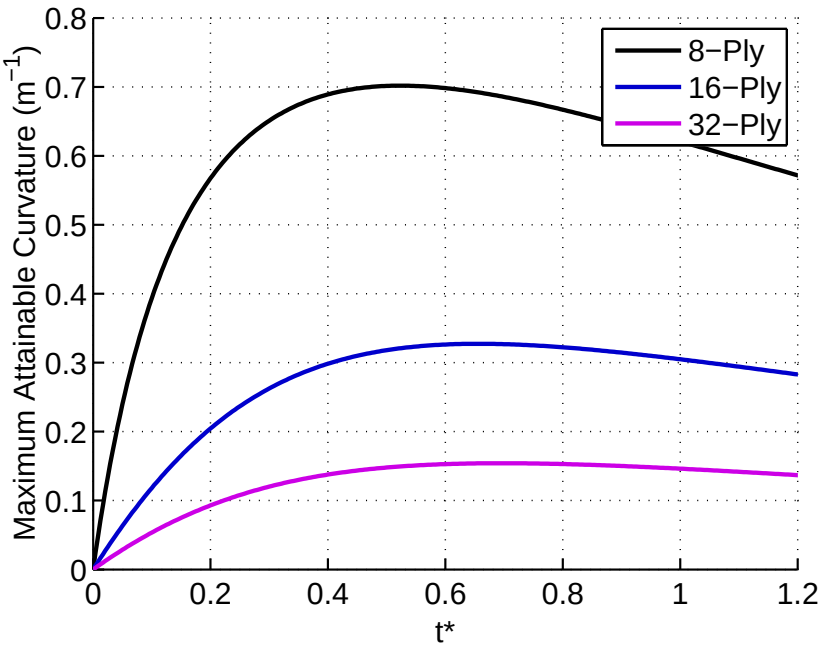

Figure 7.10: Active layer thickness ratio, t*, on maximum actuation curvature change.

7.3 Patterned Electrodes

By discretizing the electrodes on one surface of the active material, varying levels of through-thickness electric field can be prescribed across the surface. This allows for spatial control in the level of induced strain. Figure 7.11 displays this phenomenon where the electrodes on a free-standing triangular patch of PZT-5A have been patterned into four smaller triangular regions. The corresponding in-plane strain of the entire patch is measured using DIC after applying an electric field of -0.8 MV/m to each region independently. From Figure 7.11(b) it is apparent that discrete regions of strain are achieved at the four electrode locations. Very little interaction is observed between each region as evident by the sharp boundaries in the measured strain values.

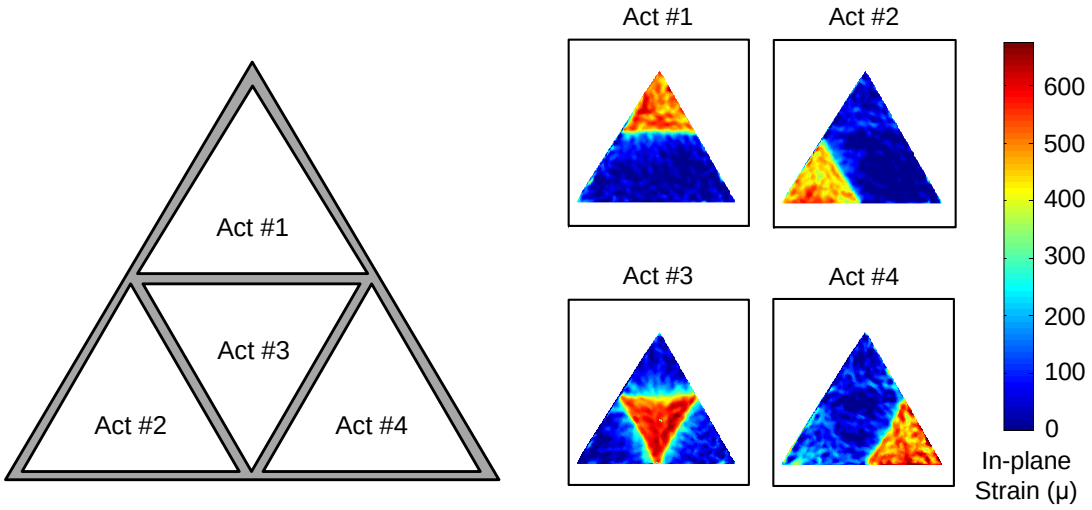

(a) (b)

Figure 7.11: Actuation of discrete regions using patterned electrodes.

7.3.1 Optimal Electrode Pattern

For a given mirror construction the shape correction performance is dictated by the actuation electrode pattern. By changing the number of discrete electrodes as well as their geometry, changes in actuation properties can be realized. An extensive amount of work has been performed in a separate effort in order to optimize the electrode pattern design [28, 17]. Figure 7.12 displays a pattern optimized to correct for astigmatism based errors while keeping the overall number of electrodes to a minimum. The pattern has been modified in order to conform to the octagonal shape of the mirror for the present study. It was chosen due to the fact that astigmatism is observed to be the most prevalent mode of shape error inherent to the CFRP substrates. The thin electrodes at the edge of the mirror are especially good at producing the non-axisymmetric modes of deformation required for astigmatic corrections. A comparison of this pattern to more traditional patterns is presented in [17].

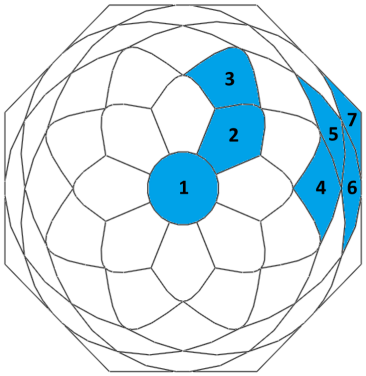

Figure 7.12: Optimized electrode pattern displaying unique electrode positions.

7.4 Shape Error Correction

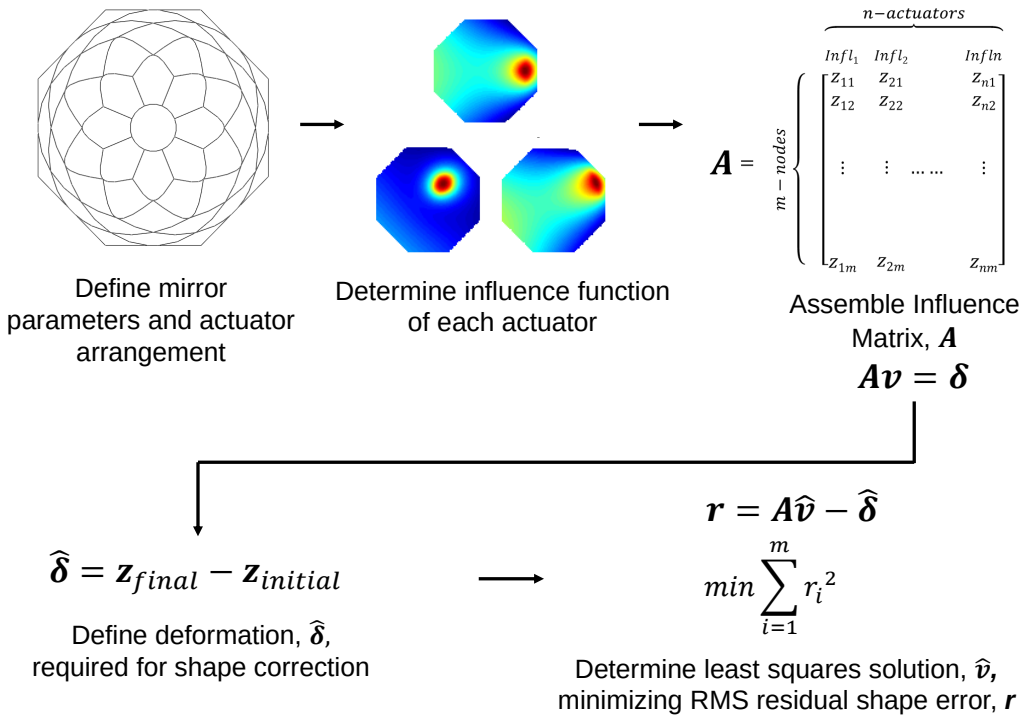

Figure 7.13: Schematic of shape correction process.

The shape correction procedure, depicted schematically in Figure 7.13, is as follows: the initial shape of a mirror is parametrized by its out-of-plane coordinate, $\mathbf{z_{initial}}$, over m equally spaced grid points. Assuming the mirror has n independent active regions (electrodes), the change in out-of-plane coordinate at these grid points due to a unit input (i.e., application of 1V) can be determined for each actuator. This is defined as the influence function of the actuator, $\mathbf{Infl_j}$, for $j = 1, 2, ..., n$. The n influence functions can then be assembled into an m x n influence matrix, **A**, containing the entire actuation capabilities of the mirror. The

influence matrix is a linear map between the applied through-thickness voltage and the corresponding shape deformation, $\boldsymbol{\delta}$:

$$\mathbf{A}\mathbf{v} = \boldsymbol{\delta}, \tag{7.5}$$

$$\boldsymbol{\delta} = \mathbf{z_{final}} - \mathbf{z_{intial}}, \tag{7.6}$$

assuming material and geometric linearity and neglecting coupling between piezoelectric properties and stress state. However for many applications the inverse problem is of interest where the voltage map required to impose a certain deformation, $\hat{\boldsymbol{\delta}}$, is desired. In general, this is an over-constrained (under actuated) problem and therefore the least squares solution to Equation 7.5 is desired. This solution will produce the required voltage map, $\hat{\mathbf{v}}$, that minimizes the L2 norm, or equivalently the RMS value of the residuals defined as

$$\mathbf{r} = \mathbf{A}\hat{\mathbf{v}} - \hat{\boldsymbol{\delta}}. \tag{7.7}$$

The above process imposes zero limitations on the magnitude of applied voltages. However, for active materials such as PZT there are strict limits on these values. Therefore, a constrained least-squares algorithm must be implemented in order to handle these conditions. Many existing tools are available in order to perform this function. For the present study, the built-in function *lsqlin* in MATLAB was used to constrain the applied voltages to their operating range (corresponding to a max/min electric field of $\pm$0.8 MV/m ($\pm$100 V) for PZT-5A).

7.4.1 Numerical Model

The actuation capabilities of the mirrors were modeled using Abaqus CAE/Standard 6.12 using conventional elastic shell elements with reduced integration (S4R). In the model a thermal expansion analog was used where the linear coefficient of thermal expansion and a subsequent temperature change was used to mimic the linear piezoelectric response and applied electric field. Through a custom Python script, the influence function of each actuator was determined by defining a non-zero expansion value for the actuator of interest. The expansion value was scaled such that a unit temperature change corresponded to the application of 1 V.

Figure 7.14 compares the central influence function for the 8, 16, and 32-ply designs. The results are presented for a 150 mm diameter mirror with a 125 μm thick active layer. The amplitude each influence function has been scaled to its full-scale value corresponding to an applied electric field of 0.8 MV/m (100V). From the results, the magnitude of induced deformation is observed to decrease as the substrate thickness increases. This is as expected due to the higher bending stiffness for the thicker CFRP substrates. In addition, the response of the 8-ply design is observed to differ from the that of the 16 and 32-ply even

though the electrode pattern is common between all designs. This difference is due to the lack of isotropy in bending stiffness for the 8-ply laminate. Therefore, the shape of the influence function for this design displays a lower degree of rotational symmetry in comparison to the 16 and 32-ply designs. Figure 7.15 displays the influence functions associated with the unique electrode positions of the optimized pattern for the 16-ply design. Peak-to-valley deformations on the order of 6 - 20 μm are predicted for this design.

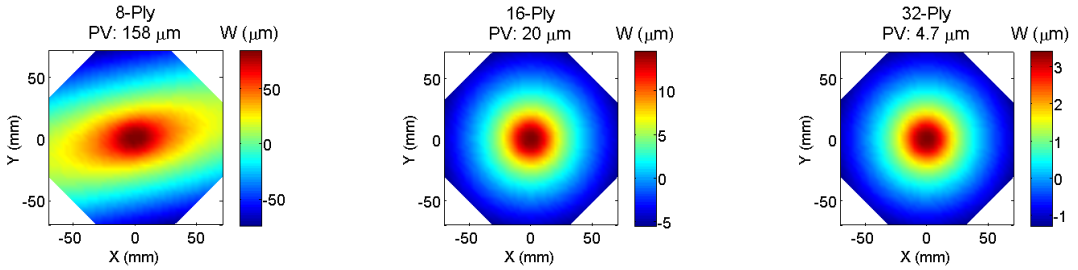

(a) (b) (c)

Figure 7.14: Comparison of central influence function for a) 8-ply, b) 16-ply, and c) 32-ply designs.

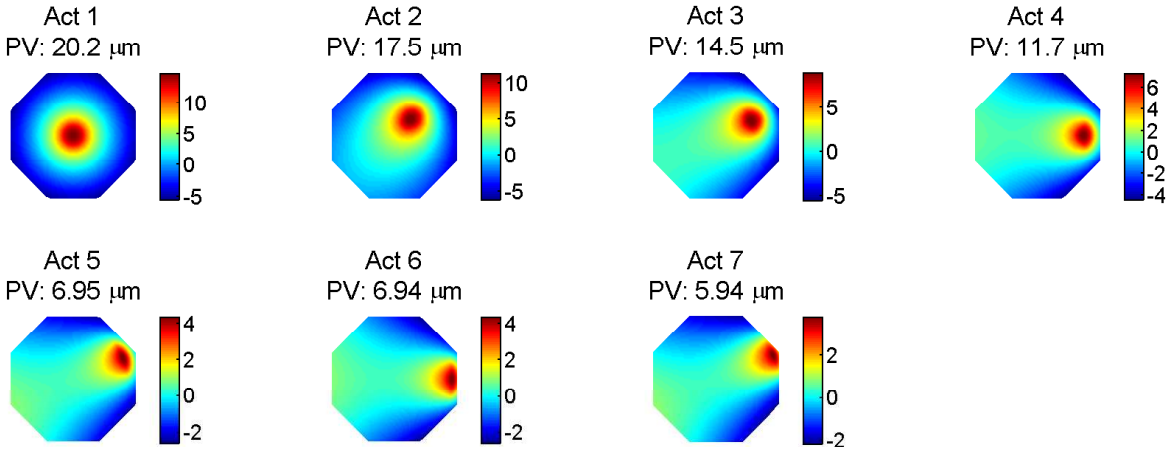

Figure 7.15: Predicted influence functions for a 16-ply active mirror with 125 μm thick PZT.

7.4.2 Predicted Performance

Using the influence functions above, performance simulations can be conducted. Figure 7.16 displays the results of one such case where the active elements are used to correct initial astigmatic errors. This is of particular interest to the present study as astigmatism is the dominant mode of figure error for CFRP substrates. At 5.0 μm RMS of initial astigmatic error 55 nm RMS of residual error is present after correction (considering 95% of the overall aperture). The voltage map required for shape correction is shown in Figure 7.16(c). At this level of initial error 12 of the 49 actuators have begun to saturate at their maximum

voltage values (± 100V), while others are operating at much lower values. The saturated actuators are those located around the perimeter of the mirror, as these have the greatest influence over astigmatism corrections. This also coincides with the location of maximum residual errors.

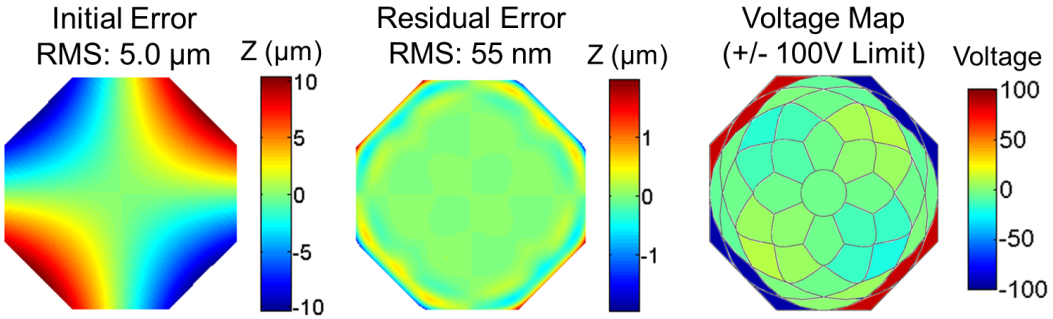

(a) (b) (c)

Figure 7.16: Shape correction results for a 16-ply mirror showing: a) 5 μm RMS of initial astigmatic error, b) the residual error of 55 nm RMS after correction (considering 95% of the overall aperture), and c) the corresponding actuator voltages required for correction showing a large degree of saturation.

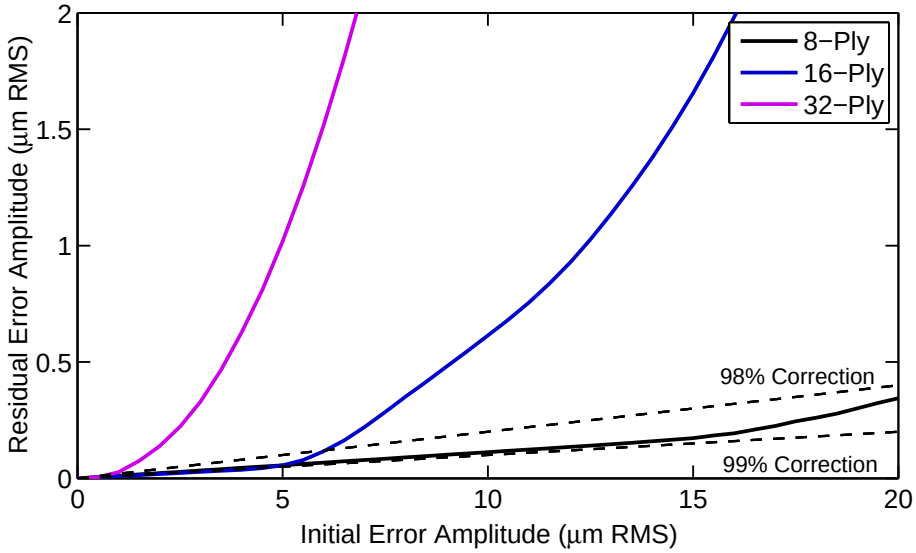

Figure 7.17: Comparison of astigmatism correction for 8, 16, and 32-ply mirror designs.

Figure 7.17 is a more comprehensive study of astigmatic correction detailing the performance of 8, 16, and 32-ply active mirror designs by plotting the residual error amplitude as a function of initial astigmatic error. Several observations can be made from this figure. The first is that for small initial errors ($<$ 1 μm RMS), all three designs have correction factors of approximately 99%. In this regime all actuators are operating under the ± 100V limit. However, as the magnitude of initial error increases, actuator saturation

begins to occur. For the 32-ply design this occurs almost immediately as the under-sized 125 μm active layer does not contain enough actuation authority in order to deform the stiff mirror substrate. The onset of saturation is delayed for the 8 and 16-ply mirror designs. The 16-ply design begins to saturate at 5 μm RMS while the 8-ply design can accommodate 15 μm RMS of initial astigmatic error before saturation. Actuator saturation drastically decreases the correction capabilities of the mirror, as is evident by the large increase in slope for each curve. Therefore, it is desired to stay well below this range by reducing the magnitude of initial error if possible.

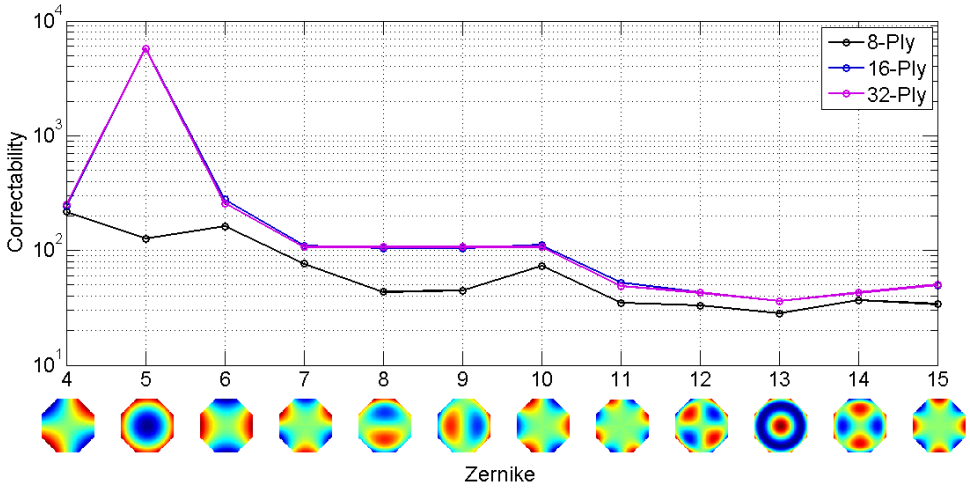

Figure 7.18: Correctability of Zernike modes for 8, 16 and 32-ply mirror designs.

Figure 7.18 displays the correctability of the three mirror designs over various Zernike modes. Correctability is defined as the ratio of residual error to initial error for each specific mode before actuator saturation occurs:

$$Correctability_k = \frac{(Z_k^{zern})_{rms}}{(r_k^{zern})_{rms}} \tag{7.8}$$

where Z_k^{zern} is the kth Zernike mode and r_k^{zern} is the residual shape error after correction of that mode. It should be noted that Zernike modes are only valid over a circular domain. To accommodate the octagonal shape of the mirror designs, a circular domain encompassing the entire mirror substrate was defined and then truncated to the octagonal form-factor.

Several observations can be made from Figure 7.18. First, the performance of the 16 and 32-ply designs is near identical over all Zernike modes. This is due to the similar laminate orientation producing near isotropic substrates. As previously stated, the 8-ply laminate is not isotropic in bending and therefore will not have the same behavior as the other two designs. A decrease in correctability is observed over all modes for this laminate. Second, for the 16 and 32-ply laminates the correctability is highest for the change in bulk curvature, often denoted as defocus (mode 5). This mode is achieved by uniformly actuating the entire active layer at near equal voltages, as demonstrated in the previous chapter. Therefore, shape errors due

to differing voltage levels at neighboring actuators do not arise. However, for the 8-ply design the vast difference in bending stiffness in orthogonal directions does not allow for equal curvature changes upon uniform actuation. Therefore, the correctability in defocus is significantly reduced. It is also observed that all mirror designs possess relatively high levels of correctability over the two astigmatic modes (mode 4 and 6). This is due to the chosen electrode pattern as it was optimized for astigmatism-based deformations. Finally, correctability is observed to decrease for increasing Zernike modes as the finite size of each electrode limits the ability to correct for higher spatial-frequency errors

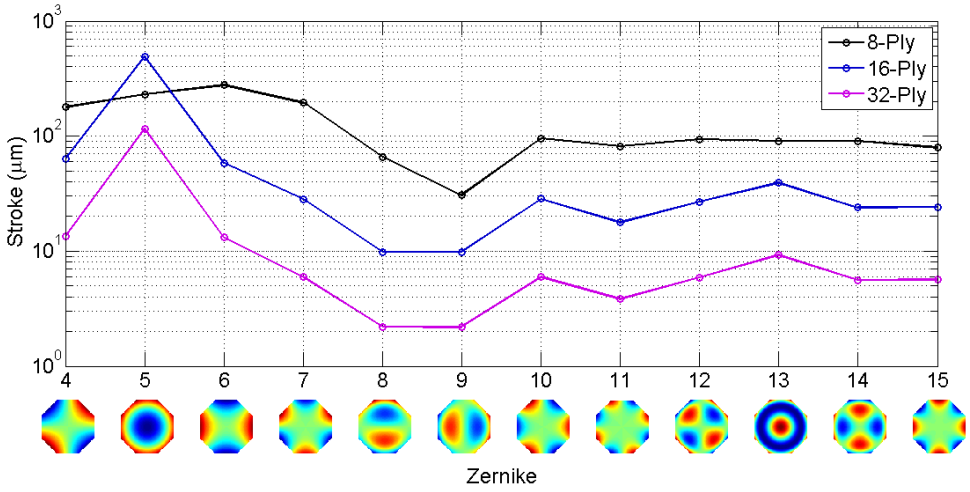

Figure 7.19: Zernike stroke for 8, 16 and 32-ply mirror designs.

The stroke of the mirror for each Zernike mode is presented in Figure 7.19. Stroke is defined as the maximum achievable RMS Zernike amplitude before saturation of the first actuator:

$$\begin{aligned} Stroke_k &= (Z_k^{zern})_{rms} \\ s.t.\ |V_i|_{max} &= 100V. \end{aligned} \tag{7.9}$$

For all modes other than defocus, stroke decreases as the substrate ply-count increases due to the increased bending stiffness. The defocus mode for the 8-ply substrate is decreased due to its non-isotropic properties.

7.4.3 Orthotropic Actuation

The preceding actuation scheme utilized the d31 component of the active material. In this method, an in-plane isotropic actuation strain is produced in the material upon the application of voltage. Therefore, the resulting curvature changes produced through actuation are coupled. This is a relatively poor method of actuation as certain modal deformations may require curvature changes in one direction only. A method to increase the figure correction performance is to implement an orthotropic actuation scheme, providing more independent control over orthogonal curvatures. In this method it is assumed that the material is able to

exhibit independent strain values in orthogonal directions at each electrode location.

A method to practically achieve such a scheme would be to implement interdigitated electrodes, depicted schematically in Figure 7.20. With this method, in-plane electric fields are produced, thus activating the d33 actuation mechanism which produces strain in the direction of the field. The direction of applied electric field can be defined by properly orienting the interdigitated electrodes and thus providing control over the direction of actuation. Two (or more) layers of active material are necessary for this scheme, with the electrode directions oriented in perpendicular directions.

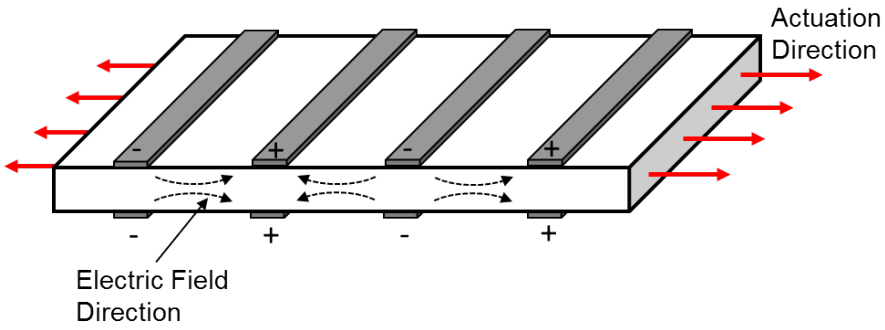

Figure 7.20: Schematic of interdigitated electrodes producing in-plane actuation strains in the direction of applied electric field.

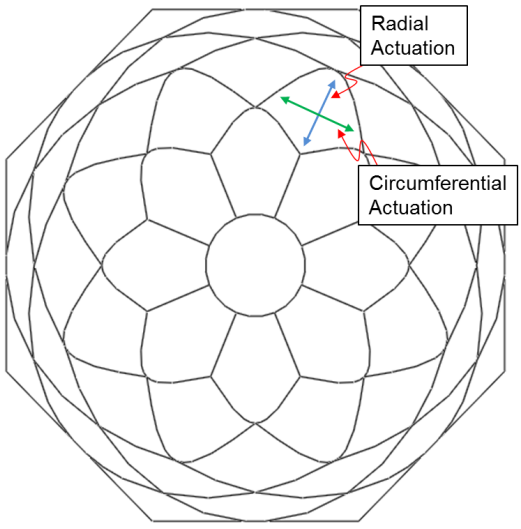

Figure 7.21: Schematic of orthotropic actuation concept.

To study the increase in figure correction performance, the numerical model was modified to accommodate the orthotropic actuation scheme. For simplicity, a single layer of active material was used and the figure deformations due to radial and circumferential actuation strains were determined at each electrode location (Figure 7.21). This was performed by defining a polar coordinate system with the origin at the center of the mirror as well as orthotropic expansion values for the active material. The size of the influence matrix

is now doubled, as there are now two influence functions for each electrode location.

The radial and circumferential influence functions at a single electrode location are shown in Figure 7.22. Differing figure deformations are predicted depending on the actuation direction. The radial influence function produces curvature changes predominantly in the radial direction while the circumferential influence function produces higher levels of curvature changes in the circumferential direction. Therefore, a higher level of actuation authority is obtained through this process.

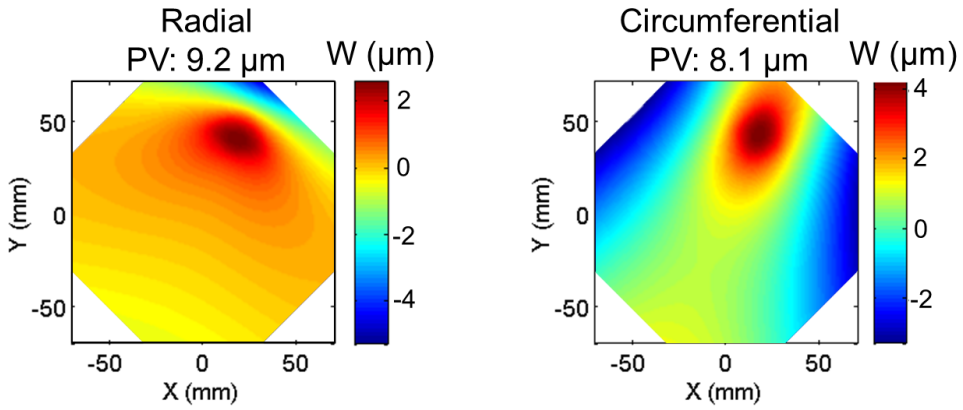

Figure 7.22: Radial and circumferential influence functions from the orthotropic actuation scheme (Results shown for 16-ply design).

A comparison of the correctability obtained through isotropic and orthotropic actuation schemes is presented in Figure 7.23 for a 16-ply design. It is apparent that the orthotropic scheme outperforms the isotropic method for all modes of deformation. Most notably, a 3.5 increase in astigmatism-based deformations is observed. Significantly higher levels of correctability are also predicted for higher-order modes, thus demonstrating the utility of the orthotropic actuation principle.

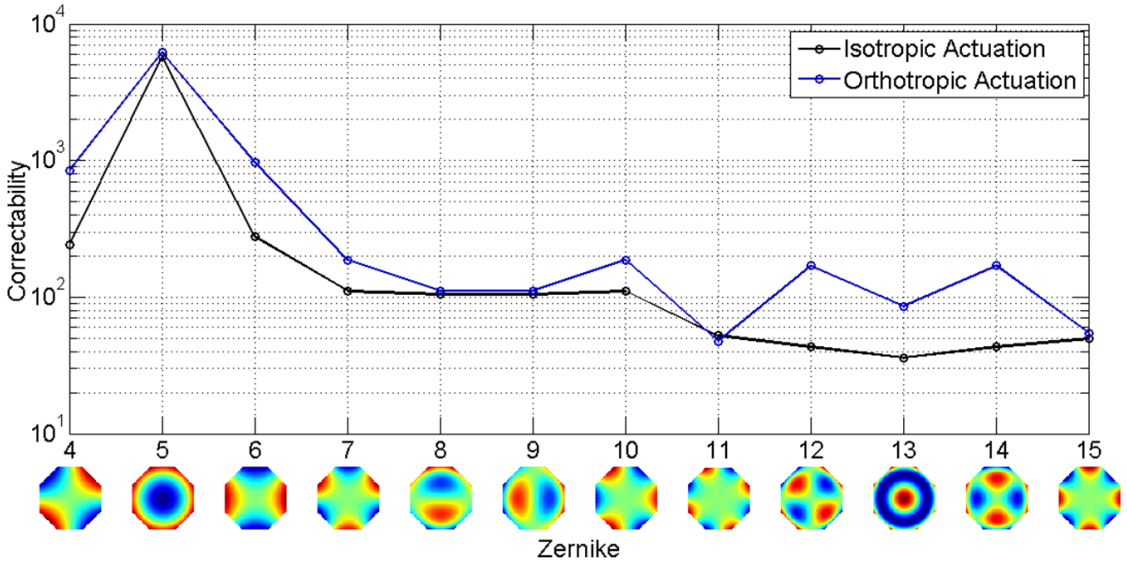

Figure 7.23: Comparison of correctability for isotropic and orthotropic actuation schemes (Results shown for 16-ply design).

Chapter 8

Mirror Experiments

8.1 Wavefront Characterization

Several methods exist in order to characterize the wavefront of an optical system. The methods considered here are based on direct slope measurements. The most common is the Shack-Hartmann test depicted schematically in Figure 8.1. The wavefront under test (i.e., the wavefront propagated from the surface of a mirror) is passed through a regularly spaced array of microlenses known as lenslets. Each lenslet samples the incoming wavefront, producing a spot on a CCD sensor. If the wavefront is perfectly planar, a regular grid of spots will be produced, as shown in Figure 8.1(a). However, if the incoming wavefront is distorted, the spots will be shifted from their nominal positions. The magnitude of shift for each spot is directly proportional to the local slope of the distorted wavefront at the location of each lenslet. Therefore, a Shack-Hartmann sensor can be considered as a linear mapping of wavefront slopes to focal-plane spot displacements. From the law of reflection, the slope of the mirror surface can be deduced as exactly one half of the measured wavefront slope. With this knowledge, the mirror figure can be determined through simple integration.

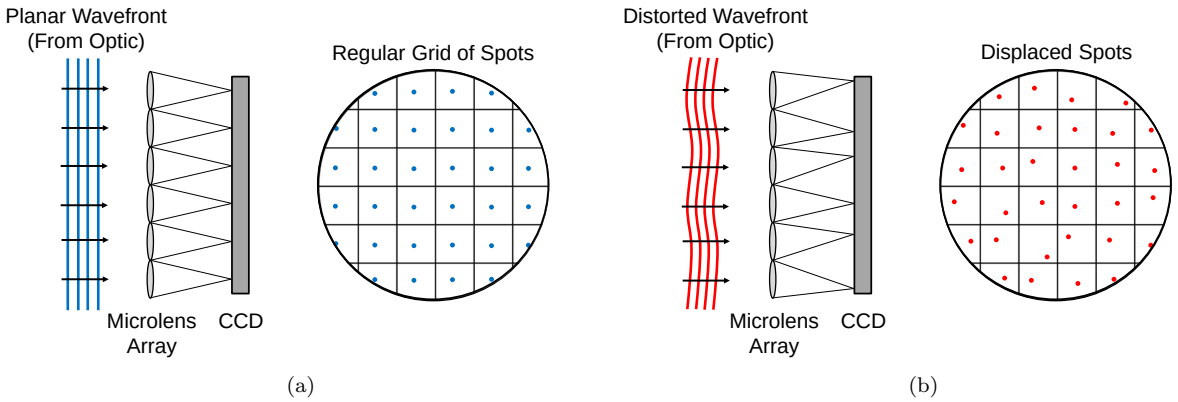

Figure 8.1: Schematic depiction of a Shack-Hartmann wavefront sensor displaying spot displacements from a distorted wavefront.

There are several limitations when implementing a Shack-Hartmann Wavefront Sensor (SHWFS) for

characterization of large optics. The first is related to limitations on the aperture size of the sensor. This is nominally defined by the size of commercially-available focal plane detectors (CCDs, CMOS). These sensors typically have a maximum in-plane dimension of $\sim$ 20 mm, and therefore SHWFSs often have apertures below this value. In order to measure the entire mirror surface, a significant reduction in the size of the wavefront must be performed. For optics of high-quality, this is often achieved without great difficulty. However for optics containing significant levels of figure error, challenges arise as it becomes difficult to obtain the necessary collimated beam required for wavefront characterization. Simply passing all of the light through the aperture of the SHWFS proves challenging.

Second, conventional SHWFSs use a windowing technique where the spot produced from a specific lenslet is assigned to a specific area on the focal plane. The displacement of each spot is then defined relative to the centroid of these windows. However, if the spot produced from a lenslet enters into the window of its neighbor, the displacement determination process will fail and the measurement will not be made at that location. Such a situation will arise if the wavefront slopes are too large in amplitude. Therefore, this imposes limitations on the range of measurements that can be performed.

The final consideration is related to high spatial frequency errors in the wavefront. In order for each lenslet to produce the desired spot on the detector, the local wavefront across the diameter of the lenslet must vary only in an approximately linear fashion. This is true for low and mid-spatial frequency errors where the characteristic length scale of the wavefront error spans many lenslet diameters. However if the wavefront slope contains high spatial frequency variations then the wavefront sampled by each lenslet will not be linear. Ultimately, this will result in aberrations in the shape of the spot produced on the focal plane. If these aberrations are large, the spot detection algorithm used to determine spot displacements will fail along with the corresponding wavefront measurement.

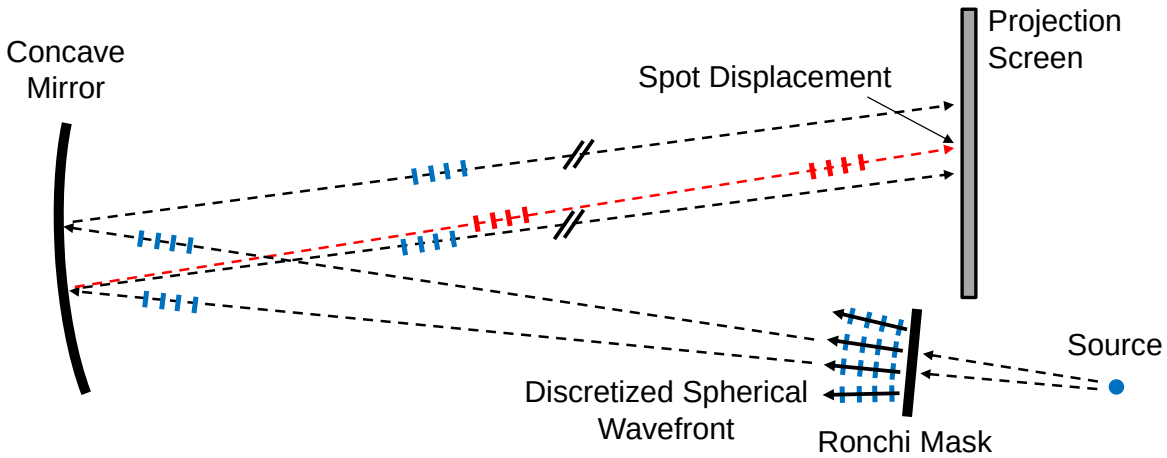

Figure 8.2: Schematic of Projected Hartmann test showing nominal beamlet reflection from a perfectly spherical mirror (blue) and one with local slope errors (red).

An alternative to the Shack-Hartmann test is a "Projected-Hartmann" test, depicted in Figure 8.2. An

explanation of the system using a nominally spherical mirror is presented. A diverging beam of light is used to illuminate the mirror to be characterized. The mirror is positioned such that its focus matches that of the beam. Under these conditions a collimated beam of light will be produced from the mirror. In order to measure surface slopes, the diverging beam is masked by a series of small apertures producing discrete "beamlets". Each beamlet is reflected off of the mirror and onto a flat projection screen. The mirror is tilted slightly off axis in order to accommodate the physical size of the screen. If the mirror is perfectly spherical, a regular grid of spots will be produced on the screen. However, if slope errors exist, the spots will be displaced from their nominal positions as with the Shack-Hartmann test. The advantage to this test is that an image of the surface need not be formed in order to produce the spot pattern. The spots from the beamlets are produced under collimated conditions and the projection screen is the same physical size as the mirror. A simple external camera can be used to capture the spot pattern on the screen, allowing for the characterization of extremely large wavefront slope errors. This proved to be essential for the current effort due to the relatively large amplitude of initial figure error as well as the extremely large actuation capabilities produced upon actuation.

8.2 Description of Metrology Setup

Figure 8.3 displays the metrology apparatus used for mirror characterization. A ray-trace diagram of the system is also found in Figure 8.4. The setup is a dual-stage system accommodating both the Projected Hartmann and Shack Hartmann tests. For the first stage, the Projected Hartmann test is implemented. Using a fiber laser, re-imaging lenses (L1 and L2), and a beam splitter (BS) a diverging beam is produced directed towards the mirror under test. Directly after the focal plane of the beam a "Ronchi mask" is placed producing the required beamlets. A Ronchi mask is simply a glass plate with a series of open and closed apertures fabricated onto one surface. The beamlets are then propagated off of the surface of the mirror under test and onto the downstream projection screen. The spot pattern produced by the beamlets is then imaged using the external camera and compared to a regular grid in order to determine the local slope errors associated with the test mirror. Figure 8.5 displays a grid-displacement measurement of a highly-aberrated mirror using the Projected Hartmann setup. The dominating astigmatic error is evident in the pattern of the spot displacements relative to the nominal grid.

The second stage of the apparatus implements the Shack-Hartmann test. In this stage, the Ronchi mask is removed and therefore the mirror is illuminated entirely by the diverging beam. The projection screen is also removed, revealing a flat mirror in its place. The flat mirror sends the collimated light back to the test mirror, producing a focused beam returning back into the system. This beam is collimated by L2 and passed through the BS and onto a fold mirror, where L3 and L4 relay the pupil and reduce the diameter of the beam to fit within the aperture of the SHWFS. This system is a "double-pass" test, as two reflections off of the test mirror are required. Therefore, the measured wavefront errors are doubled in comparison to

the Projected-Hartmann test.

Theoretically, both of the stages within the system can be used to obtain initial knowledge of the mirror figure. They can also be used to characterize the influence functions of the mirror. However, due to the relatively low dynamic range of the SHWFS, the double-pass system, and the magnitude of initial figure error for the mirrors implemented in this study, it was not possible to obtain initial knowledge of the figure error with the SHWFS test. Therefore, the first stage implementing the Projected Hartmann test was used to characterize the mirror figure as well as the actuation capabilities. It was intended that an initial "coarse-correction" was to be performed with this system, reducing the figure error sufficiently to pass into the SHWFS; however, difficulties arose with this process as well.

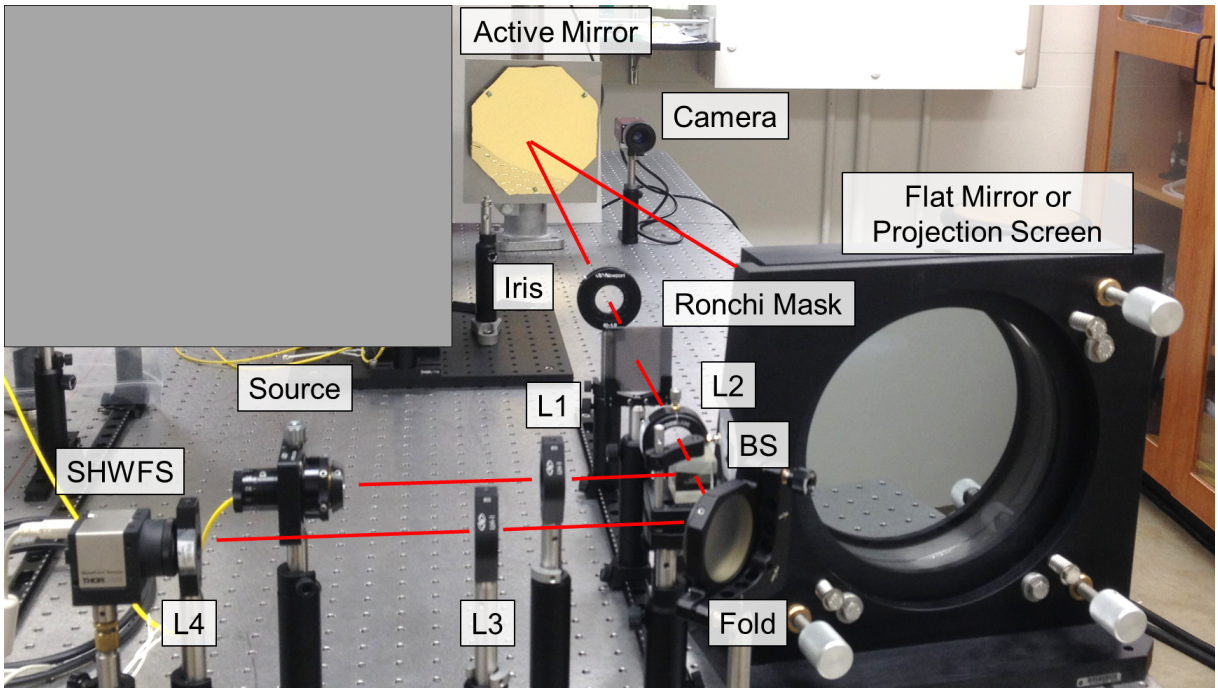

Figure 8.3: Picture of custom metrology apparatus used for mirror experiments.

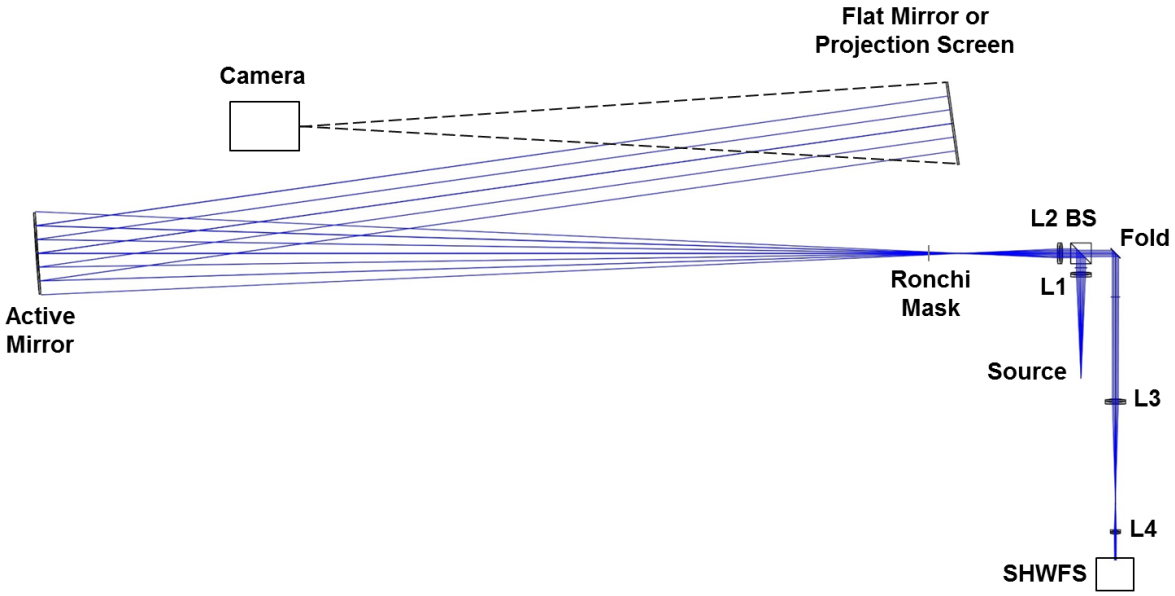

Figure 8.4: Ray-trace diagram of custom metrology apparatus demonstrating the two optical paths.

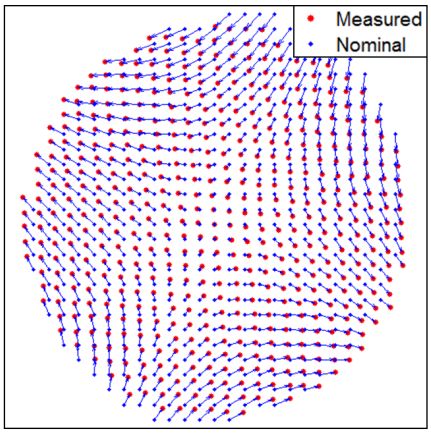

Figure 8.5: Spot pattern produced using the Projected Hartmann apparatus showing deviations from a regular grid.

8.3 Verification of Projected Hartmann Setup

In order to verify the figure reconstruction of the Projected Hartmann apparatus, two verification tests were performed. The first compared measurements obtained using speckle photogrammetry to the Projected Hartmann test. The mirror under test was a bare CFRP substrate that was cured on a glass mandrel. By curing on polished glass the replication process was able to produce a relatively smooth front surface on the mirror. Adequate reflection of laser light was achieved from this surface allowing the Projected Hartmann test to be performed. Prior to doing so, the substrate was measured using speckle photogrammetry by spraying

a fine pattern of white paint onto the surface. It was discovered that the applied speckle pattern had only a minimal effect on the reflection properties of the mirror, and therefore the Projected Hartmann measurement could be performed even with the speckle pattern applied. This allowed for a seamless transition from the photogrammetry test to the Projected Hartmann apparatus. Both of these tests were performed with the mirror mounted in a vertical orientation and thus under the same gravity loading conditions.

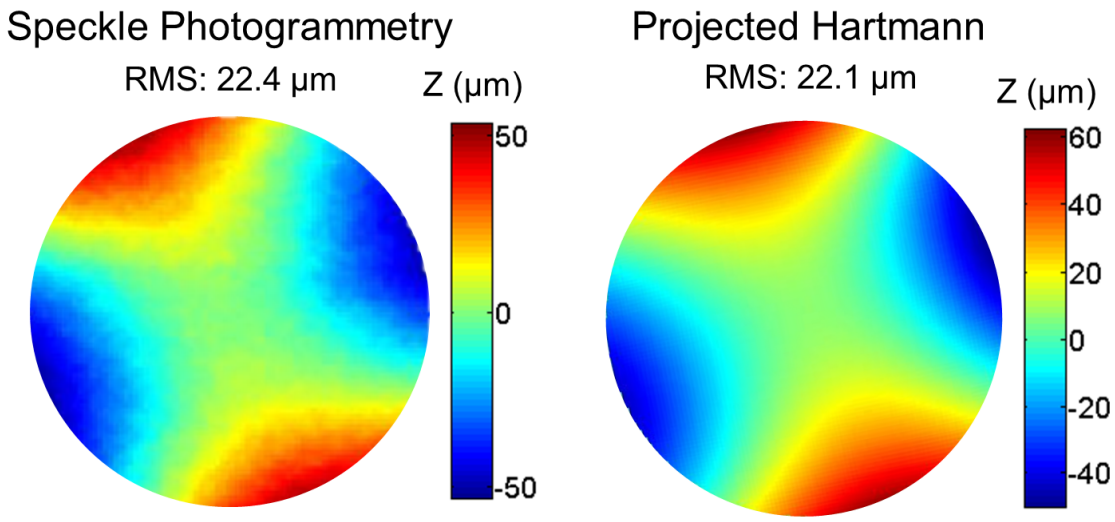

Figure 8.6: Comparison of Projected Hartmann measurement and speckle photogrammetry measurement displaying good agreement over high-amplitude astigmatic modes.

Figure 8.6 compares the measurements made using the photogrammetry and Projected Hartmann systems. It is evident from both measurements that the dominant mode of shape error is astigmatic in nature. Good agreement is observed between the two systems with RMS figure errors of 22.1 μm and 22.4 μm measured for the Projected Hartmann and photogrammetry measurements, respectively. At this magnitude of figure error, significant difficulties would be encountered if more traditional optical measurement techniques were attempted. Therefore, not only does this measurement verify the accuracy of the Projected Hartmann over low-order modes, but it also demonstrates the utility of the system due to its accommodation of large-amplitude figure errors.

An additional measurement was performed with a mirror displaying higher-order modes of figure error but of lower amplitude. The measurements were performed on a CFRP mirror with a reflective nanolaminate facesheet but with no actuation capabilities (without the integrated active layer). This mirror was constructed using the fully-refined techniques for CFRP substrate construction as well as the low-stress nanolamiante bonding process outlined in Chapters 4 and 5, respectively, and is therefore of higher quality. A commercial high-dynamic range SHWFS (HASO3-76) was used to measure the figure error in an external setup not depicted here. Care was taken in order to ensure the measurements were performed over the same aperture diameter (100 mm).

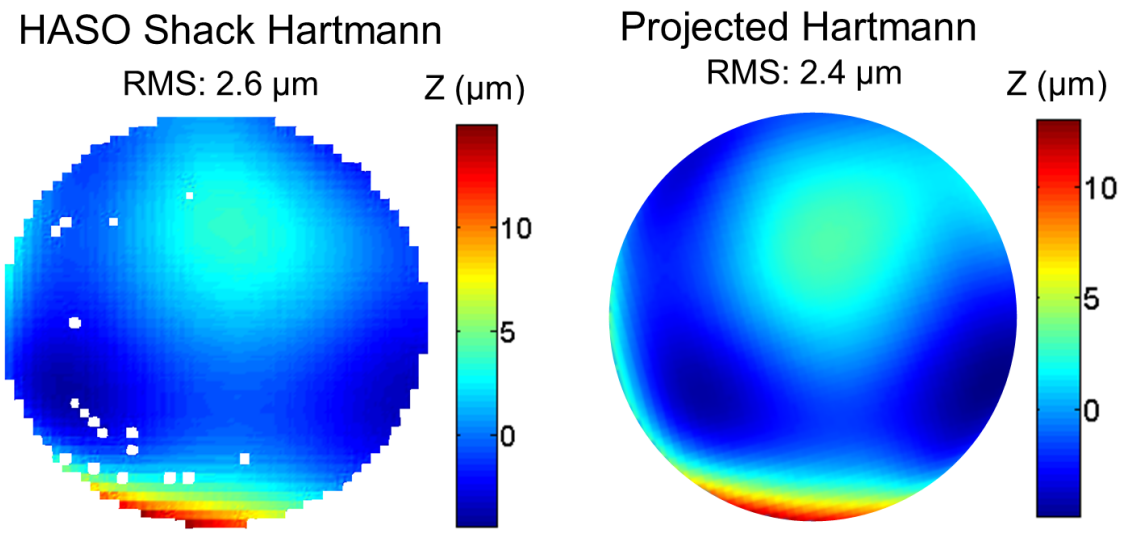

Figure 8.7: Comparison of Projected Hartmann measurement and Shack-Hartmann measurement (HASO3-76) displaying good agreement over low-amplitude mid-spatial frequency modes.

Figure 8.7 displays the measurements performed with both systems. It is apparent that the magnitude of figure error is much lower in comparison to the test performed with speckle photogrammetry. The mode of deformation is also no longer dominated by large astigmatic errors. Therefore, this comparison is a good indicator as to whether the Projected Hartmann setup can adequately capture mid-spatial frequency errors. By comparing the results, good agreement is observed between the two surface reconstructions. There is also good agreement in the magnitude of measured surface error with 2.4 μm RMS measured using the Projected Hartmann test and 2.6 μm RMS using the HASO SHWFS. It should be noted that this initial figure error of $\sim$ 2.5 μm RMS is the lowest measured to date for the current effort. From the results of these two tests, confidence was gained in the ability of the Projected Hartmann setup to capture a wide range of figure errors.

8.4 Shape Correction Experiments

8.4.1 Active Mirror Prototype

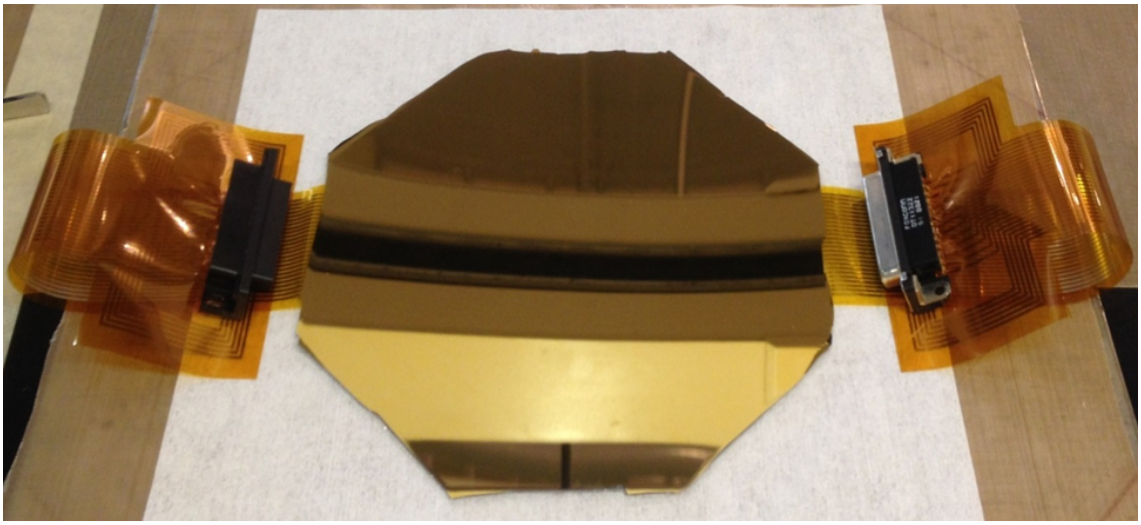

Figure 8.8: Front surface of fully-integrated Carbon Shell Mirror (CSM) prototype.

Figure 8.8 displays the Carbon Shell Mirror (CSM) prototype used for shape correction experiments. The prototype contains a 16-ply CFRP substrate, 50μm thick reflective nanolaminate facesheet, 125 μm thick active piezoelectric layer, and 25 μm thick flexible electrode wiring. Surface-mount D-connectors are implemented on flex cables in order to connect the 41 actuation channels to the supporting control electronics. The mirror is octagonal, 150 mm in diameter (flat-to-flat), 750 μm thick with a measured areal density of 2.7 kg/m^2/ including electrode wiring. The prototype shown here represents a significant experimental effort that directly applies the concepts presented in previous chapters.

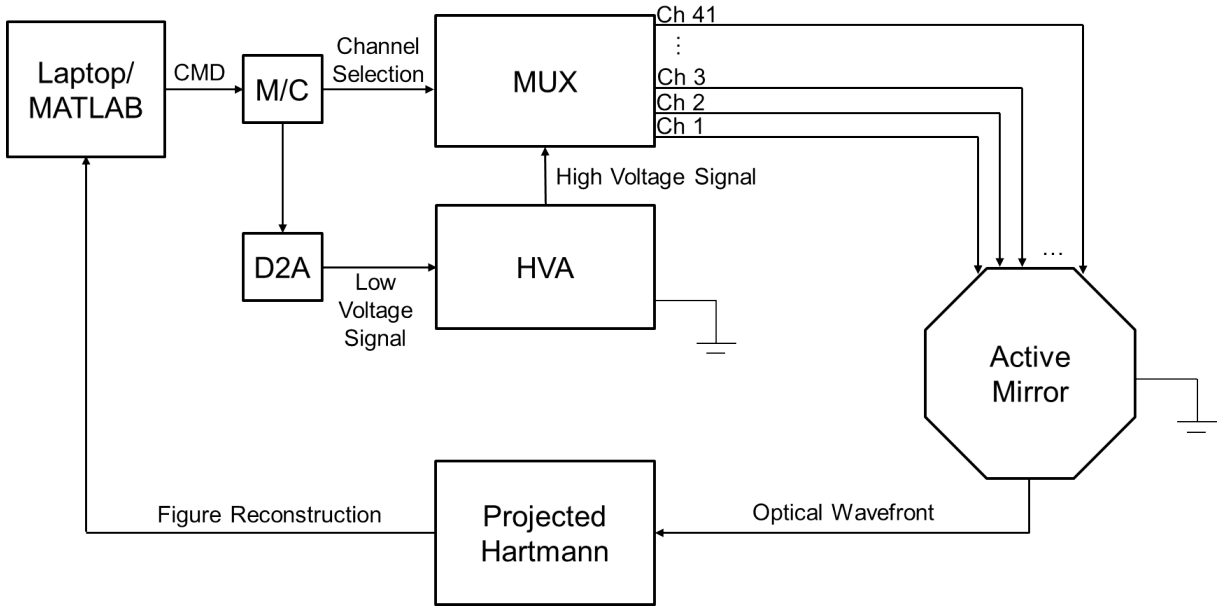

Figure 8.9: Schematic of control system used for closed-loop figure control.

A schematic of the control system used for closed-loop figure correction is shown in Figure 8.9. The control electronics were implemented from a previous effort [17] and are only discussed in brief here. First, the initial figure of the mirror is measured using the Projected Hartmann system. The voltage map required to minimize the RMS figure error is then computed via MATLAB. This voltage map is then sent to a microcontroller that in turn sends a digital signal to the D2A, producing a low-voltage analog signal that is subsequently amplified via the high-voltage amplifier (Trek 10/10B). The high-voltage signal is then sent to a custom multiplexer unit (details of the multiplexer design can be found in [17]). The multiplexer has 42 solid-state switches that open/close on command via the micro-controller. By simultaneously controlling the amplitude of the high-voltage signal and the state of each switch, the 41 actuation channels on the mirror can be controlled independently with a refresh rate of $\sim$ 1 Hz. After sending these control voltages to the mirror the wavefront from the CSM is again measured using the Projected Hartmann. The new figure error is determined and the updated voltage map required make further reductions to the figure error is computed.

8.4.2 Measured Influence Functions

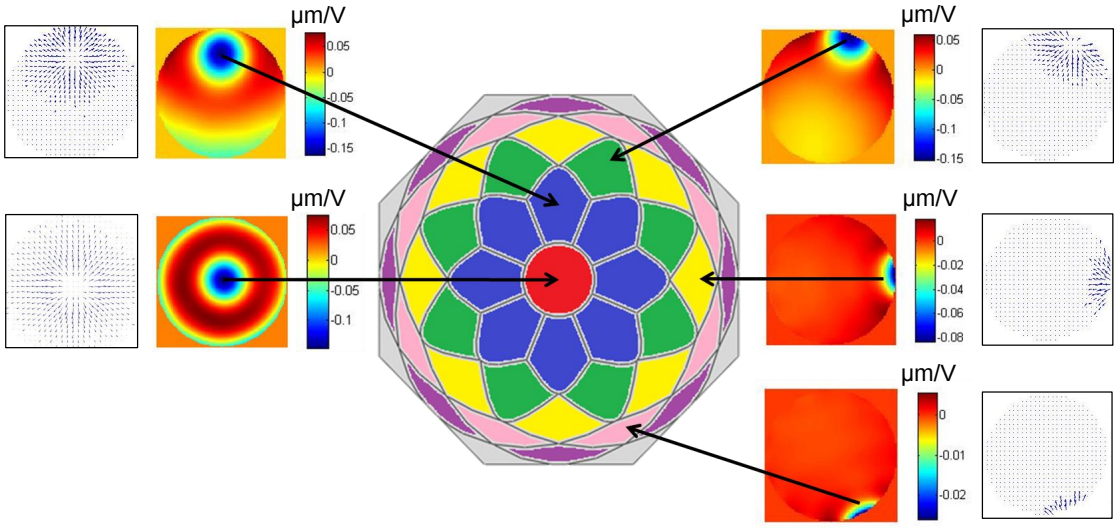

Figure 8.10: Measured influence functions using the Projected Hartmann setup.

Figure 8.10 displays the measured influence functions from the Projected Hartmann setup. The spot-displacements along with the figure reconstruction at each location are presented. Due to edge effects and errors in the reconstruction process, it was difficult to measure the influence functions of the outermost actuators. Therefore, they were omitted from the shape correction procedure. The influence function measurements were performed by taking a measurement of the mirror figure in the base state (0 V applied), and then another after the application of 50 V (half of the full-scale actuation range). A delay of 10 seconds was implemented between the application of voltage and acquisition of spot-displacements in order to mitigate the effect of piezoelectric creep. A 0 V base measurement was also required between the measurement of each influence function as residual strain in the piezoelectric material resulted in figure changes that persisted throughout the test. The peak-to-valley deformations of each actuator range from 5 - 20 μm and are therefore in good agreement with the numerical predictions in Chapter 7.

8.4.3 Figure Correction

Using the measured influence functions, a closed-loop figure correction was performed. As the Projected Hartmann system measures spot-displacements directly, the shape of the mirror as well as the actuator influence functions were defined as spot-displacements instead of figure reconstructions. This eliminated errors due to numerical integration and provided more accurate control of the mirror. However, minimization of the reconstructed RMS figure error was still used as the objective function for the controller.

The initial spot pattern produced from the mirror in its base state was measured at the start of the loop

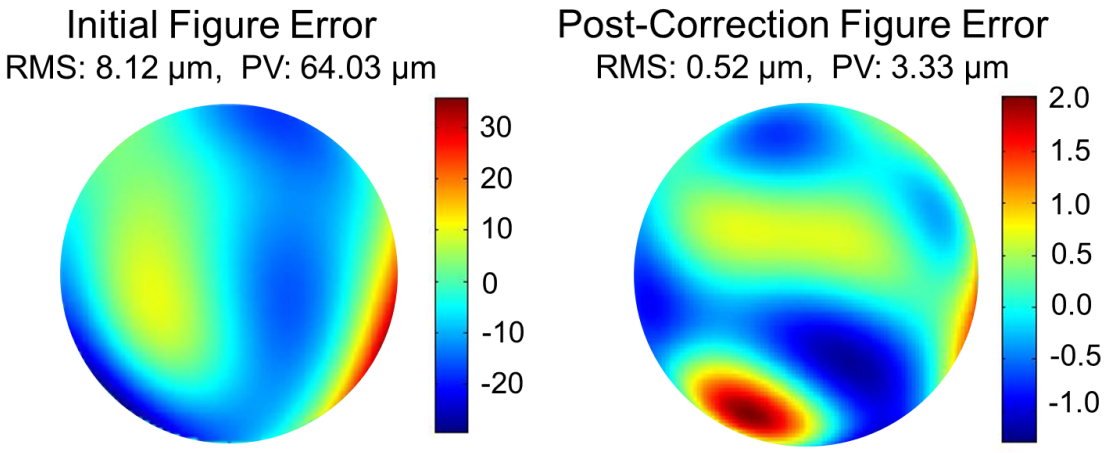

Figure 8.11: Figure error before and after closed-loop correction displaying 0.52 μm of residual error.

with all actuators set to 0 V. To correct the figure error, it is desired to command these spots to a regularly spaced grid. The spacing of this grid was allowed to vary arbitrarily throughout the correction loop. In doing so, the overall spherical curvature of the mirror was allowed to vary, thus defining error as the deviation of the mirror figure from a best-fit sphere. The optimal voltage map required to perform this function was determined using a constrained least-squares algorithm (lsqlin in MATLAB) imposing voltage limitations of $\pm$ 100 V. A gain of 0.2 was implemented in an attempt to reduce the non-linear effects of the piezoelectric material and 50 iterations of shape correction were performed.

Figure 8.11 displays the mirror figure error before and after the correction procedure considering 80 % of the mirror diameter (120 mm). A 94 % correction factor is achieved, reducing the figure error from 8.12 μm RMS to 0.52 μm RMS. It should be noted that one of the actuators experienced an electrical short prior to the test and therefore was inactive throughout the shape correction procedure. The location of the actuator corresponds to the location of high figure error in Figure 8.11. Therefore, a further reduction in figure error would be achievable if this was not the case.

8.4.4 Stage 2 Attempt

Several attempts were made in order to implement the second stage of the metrology system with the SHWFS (ThorLabs WFS150-7AR). To do so, the Projected Hartmann setup was used to correct the mirror figure error down to $<$ 1 μm RMS. The actuator voltage values were then held constant upon switching to the second stage. The Ronchi mask was removed from the optical system along with the projection screen. Adjustments were made to the orientation of the flat mirror in order to pass the beam into the SHWFS aperture. Figure 8.12 displays the measured spot displacements on the focal plane of the SHWFS. Several features are observed in this data. First, the spots along the axes of the aperture are displaced large distances and highly aberrated. It is believed that this is due to the local deformations caused by the the gaps between the four PZT plates bonded to the backside of the mirror (see Chapter 6). As these are high-spatial frequency

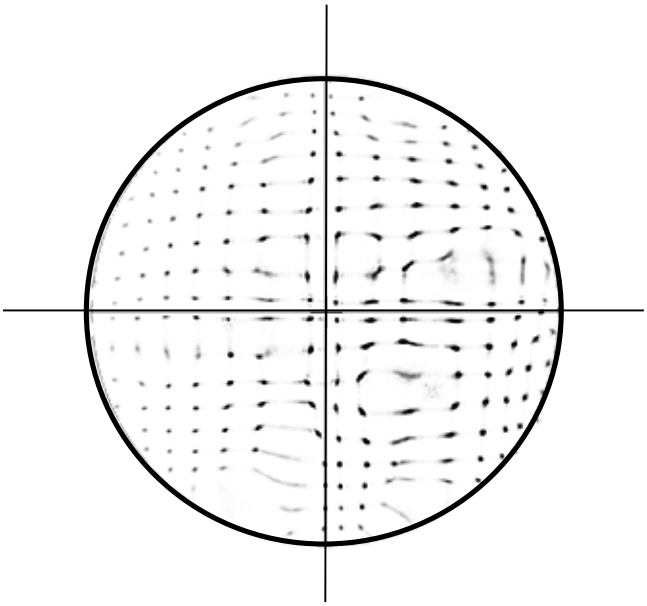

Figure 8.12: Evidence of high spatial frequency errors at the center of the mirror due to the discrete PZT plates bonded on the backside of the mirror.

features, the reflected wavefront slope error at these locations will be extremely high as well. The lenslet array is unable to adequately sample these wavefront slope errors, and thus spot aberrations are produced. Away from the central axes, the spots are more regularly spaced and less aberrated. However, due to the features produced at the center of the mirror, an accurate figure reconstruction was not produced.

Chapter 9

Conclusions

This thesis has presented a novel active mirror concept based on carbon fiber composites and replication techniques. Additional functional layers are implemented into the structure in order to provide the reflective layer, actuation capabilities and electrode routing. The mirror is thin, lightweight and exhibits large integrated actuation capabilities. The goals of this research, parallel to the development of this technology, were as follows: 1) understand the shape errors associated with thin, free-standing composite shell structures, 2) identify methods of incorporating the various other functional layers into the design, 3) study the actuation response introduced via active materials, and 4) characterize the ability to correct for manufacturing-induced errors in an experimental setting. Studies were performed motivated by mechanics intuition and experimental observations in order to obtain highly-accurate shell substrates suitable for mirror applications.

A summary and discussion of the specific findings of each study is presented below. Unique contributions as well as identified areas for further studies are then presented.

9.1 Summary of Results

The imperfections associated with ultra-thin CFRP laminates were characterized in an experimental setting and their effect on shape error analyzed. Two classes of imperfections were identified: those that were constant within the plane of the laminate and those that varied spatially. Those that were constant included misalignments in the orientation of each ply, uniform variations in the mean thickness of each ply, and through-thickness thermal gradients during cure. All three of these imperfections were shown to produce global curvature changes upon cooling from the cure temperature. Variations in the mean ply thickness were shown to be the dominant factor. Spatially-varying fiber orientations and variations in ply thickness were shown to result in higher order shape errors. Errors such as these may be of greater concern when considering applications requiring highly accurate surfaces as they would be difficult to mitigate using mechanical constraints or actuation mechanisms. However, it was shown through simulation that increasing the nominal ply thickness, reducing the cure temperature, and altering the laminate orientation had the potential to reduce the magnitude of such errors.

The behavior of thicker laminates containing higher ply counts was characterized by analyzing the in-plane and bending stiffness of each laminate. The benefit of using thin-ply materials was demonstrated as near complete isotropy was demonstrated in a laminate of only 480 μm total thicknesses. Such properties would not be achievable at that thickness using conventional composites and is therefore an enabling feature of the material. The astigmatic post-cure shape errors of these laminates were also characterized, displaying a strong dependence on total laminate thickness. Two methods were presented in order to reduce the magnitude of these effects: 1) a long-duration low-temperature cure cycle, reducing the overall temperature change and thus thermal stresses developed in the laminate, and 2) a deformable mandrel apparatus, allowing for the correction of systematic errors. With the implementation of these two process alterations a three-fold reduction in RMS shape error was realized, reducing the error from $\sim$ 50 μm RMS to 16 μm RMS over 150 mm dia. substrates (considering 16-ply laminates).

A successful method of obtaining an optically-smooth imaging surface was identified through the incorporation of a nanolaminate facesheet. Preliminary figure measurements were performed for a free-standing nanolaminate showing good agreement to that of the deposition mandrel. A low-stress bonding process was developed in order to integrate the nanolaminate onto the front surface of the CFRP substrate. The process was empirically derived over multiple trials and refined using experimental observations. Successful bonds were performed demonstrating complete mitigation of fiber print-through, reducing surface roughness from 49.5 nm to 2.2 nm RMS. A post-bond figure accuracy of 2.4 μm RMS was also achieved using the refined manufacturing techniques.

Geometry limitations associated with thin active materials necessitate the use of active elements that are 1) initially flat, and 2) undersized in comparison to the CFRP substrate. Therefore, numerical studies were performed in order to understand the mechanics behind bonding multiple flat plates to a curved substrate. The stress distribution produced in the plates from the large spherical deformations was first determined. Significant, spatially-varying mid-plane stresses were predicted as a result in the change in Gaussian curvature. Models were then developed in order to simulate the bonding process. It was shown that the mid-plane stresses significantly altered the mode of deformation produced after bonding as lobed structures were produced on the CFRP substrate local to the domain of each plate. Deformations such as these are highly undesirable as they are difficult to correct using actuation techniques. From the analysis it was determined that a reduction in substrate curvature, and thus mismatch geometry, will reduce the effect of these errors. The models also demonstrated that local deformations at the gaps between successive plates were produced after the bonding process and upon subsequent actuation. While relatively low in amplitude ($<$ 2 μm PV), the errors are highly localized, producing extreme curvature changes in the substrate. The size of the gap between each plate was shown to reduce the overall affected area; however, the amplitude remained relatively constant. A significant reduction was observed for thicker laminates due to the increased bending stiffness. Local shear deformations were also observed at the interface between the PZT and CFRP substrate perpendicular to the fiber direction of the terminal ply.

The actuation properties of two ceramic active materials were characterized experimentally. PZT, a piezoelectric ceramic, was shown to possess large actuation properties; however, issues related to piezoelectric creep, hysteresis, and depoling were identified. PMN-PT, an electrostrictive material, was shown to demonstrate much more predictable actuation characteristics with very little hysteresis. However, this material displayed a decreased range of actuation and the response was limited to in-plane compressive strains due to the mechanism of deformation. Therefore, the material would need to be biased to an offset level of strain and operated in a relative sense in order to achieve both directions of actuation. Due to simplicity, PZT was implemented exclusively for experimental efforts. A sizing argument was presented displaying optimal thickness ratios of 0.5 - 0.7 between the active layer and CFRP substrate. The actuation performance of various designs implementing 8, 16, and 32-ply CFRP substrates was compared. Astigmatic correctability factors on the order of 200 - 300 were predicted using an optimized electrode pattern. The 16 and 32-ply designs displayed near identical performance due to their similar laminate orientations. The 8-ply design displayed decreased correctability, especially with respect to axisymmetric modes, due to its non-isotropic bending stiffness. A potential method of increasing the correctability for all designs was presented using an orthotropic actuation scheme.

Finally, a fully-integrated active mirror prototype was characterized in an experimental setting using a Projected Hartmann test. The figure reconstruction of the Projected Hartmann measurement was verified against two external measurements: speckle photogrammetry and a commercial Shack Hartmann Wavefront Sensor. The system was shown to accurately reconstruct low-order modes as well as mid-spatial frequency errors, thus demonstrating its utility for the characterization of highly deformable optics. Using this system, the influence functions of the active mirror prototype were characterized and shown to have similar amplitude to the model predictions. A closed-loop figure correction was performed, reducing the magnitude of manufacturing errors by 94% from 8.12 μm to 0.52 μm.

9.2 Unique Contributions

Unique contributions specific to the field of lightweight composite shell structures have been made. A quantitative assessment of laminate and ply-level imperfections was performed for thin-ply materials produced using tow-spreading techniques. Specifically, variations in ply thickness, fiber alignment and curing conditions were characterized. By understanding these errors, limitations on surface accuracy have been identified. These limitations are useful if such laminates are to be implemented in thin structures requiring highly accurate shapes.

Significant modeling efforts were performed in order to study the bonding mechanics behind thin, multilayer, flexible structures of dissimilar initial geometry. The modeling techniques developed here are general and can be extended to various materials, additional layers, and arbitrarily unique geometries. These techniques allow for accurate modeling of the stress state in each layer after manufacturing. The models also

allow for subsequent analysis steps to be performed such as actuation or changes in temperature and can therefore be implemented for a wide variety of applications.

Using the above techniques, specific achievements have also been made in the area of lightweight active mirrors. The active mirror technology presented in this thesis represents a significant change in design compared to traditional optics. Structural redundancy in the form of added material or support structures is replaced by thin, lightweight substrates and large actuation capabilities. While it is desired to keep the overall level of manufacturing error to a minimum, initial optical-quality precision is not required with this concept. This relaxes requirements associated with fabrication and thus, simpler processes can be implemented. Non-traditional materials can also now be used as a result of this design change. Finally, the large actuation range of the mirror has the potential to correct for errors subsequent to manufacture such as thermal deformations or material creep. Therefore, in-situ corrections to the mirror figure can be made with this new concept. Mirror prototypes have been developed at areal densities of 2.7 kg/m^2 ($1/10^{th}$ JWST), $<$ 1.0 mm total thickness ($1/300^{th}$ HST), and with an optical-quality surface finish of 2.2 nm Ra. A post-corrected figure accuracy of 520 nm RMS has also been achieved, demonstrating a path-forward to diffraction-limited optics at visible wavelengths. These features, along with the associated simplistic manufacturing processes, are potentially enabling for the realization of next generation space-based telescopes.

9.3 Improvement of Figure Accuracy

While the achievement of 520 nm RMS figure accuracy is noteworthy for such a thin design, a factor of 5 reduction in figure error magnitude is necessary to meet optical-quality requirements. Through the studies conducted in this thesis, several areas of improvement have been identified. They are as follows:

- Improved CFRP materials: The thin-ply materials implemented for this study are essential in order to produce very thin mirror substrates. However, as shown in Chapter 3, significant imperfections associated with the tow-spreading process are present. Improvements in figure accuracy are expected if a higher degree of ply thickness uniformity can be realized. Further improvements are expected if even lower cure temperature resins are implemented, as this would lead to a reduction in the thermal stresses developed during cure. These two alterations would result in lower levels of astigmatic errors observed in the bare CFRP substrates.

- Curved active elements: From Chapter 6 it was demonstrated that significant figure errors are produced when flat active plates are bonded to the backside of a curved CFRP substrate. Therefore, active elements having a matching radius of curvature to that of the CFRP substrate should be implemented. At the time of writing, curved active elements made from PMN-PT have been obtained. It is expected that significant improvements to post-manufacturing figure errors will be achieved as a result of this switch. However, it was also shown in Chapter 6 that high spatial frequency deformations at the gap

locations will persist even with initially curved active elements. Therefore, studies related to filling the gaps to aid in the transfer of actuation strain should be performed.

- Improved actuation capabilities: Chapter 7 demonstrated that the actuation response of PZT is non-linear, dependent on initial conditions, and hysteretic in nature. Therefore, it is recommended that a switch be made to active materials with a more predictable response, such as PMN-PT. This carries with it added complexity due to the unidirectional response of the material. However, methods of biasing the material can be implemented. In addition, it is believed that the orthotropic actuation concept presented in Chapter 7 holds significant promise in order to increase the corrective capability of the active mirror concept. In making this switch, the design of the electrode pattern should be revisited since it was optimized for isotropic actuation schemes. The combination of these factors is expected to increase figure correction capabilities immensely.

9.4 Follow-On Work

- Thermal design and characterization: The mirror concept presented in this thesis was developed for room-temperature applications. Therefore, it is of interest to study the thermal distortions produced due to CTE mismatches between layers. Changes in laminate orientation, fiber selection, and nanolaminate thickness/composition should be considered.

- Larger apertures: It is of interest to create meter-scale mirrors. All processes developed within this thesis have kept scalability in mind, however challenges are expected to arise with an increase in scale.

- Reduced thickness designs: It is intended to ultimately produce mirrors that are thin enough such that they can be packaged into a tight initial configuration, deployed to their imagining mode once in orbit, and then use the large actuation capabilities to correct for any remaining figure errors. This concept could potentially enable increased aperture sizes for telescopes based on small satellite platforms (i.e., CubeSats).

Appendix A

Spatial Filtering of Surface Shapes

The shape of a surface can be parametrized in the spatial domain by its three-dimensional coordinates such that

$$z(x, y) = h_o(x, y), \tag{A.1}$$

where h_o(x, y) is a function describing the out-of-plane shape of the surface. For the purposes of this analysis it is assumed that the surface contains dominating high amplitude, low spatial frequency features as well as those with high spatial frequencies but comparatively low amplitudes. The later features are of interest for further study and therefore it is necessary to apply a high-pass filter to the out-of-plane coordinate data. One method to perform this is through a convolution in the spatial domain such that

$$h_{filt}(x, y) = h_o(x, y) * g_{HP}(x, y), \tag{A.2}$$

where $*$ represents the convolution operation, and g_HP(x, y) is a function defining the high-pass filter in the spatial domain. However, it is often more convenient to work in the frequency domain as this one can define bounds on the frequencies of interest. This can be performed through the use of a Fourier Transform. Therefore, the filtered data can be defined as

$$\begin{aligned} H_{filt}(u, v) &= F[h_o(x, y) * g_{HP}(x, y)] \\ &= H_o(u, v) G_{HP}(u, v), \end{aligned} \tag{A.3}$$

where F[ ] represents the Fourier Transform, and u and v are the spatial frequencies in the x and y directions, respectively. This is also convenient as the convolution operation in the spatial domain results in multiplication in the frequency domain.

As it is desired to eliminate the dominating low spatial frequency features, a convenient form of G_o(u, v) implements a Gaussian function in the following manner:

$$G_{HP}(u, v) = 1 - e^{\frac{-(u^2+v^2)}{2\sigma^2}}, \tag{A.4}$$

where σ is "floor frequency" defining the width of the Gaussian function and therefore the range of frequencies to be filtered. $G_{HP}(u, v)$ is of the form such that the central region of a centered spectra, corresponding to low-spatial frequency features, is eliminated while leaving the majority of the mid-high spatial features unaltered. In order to study the shape of the filtered surface in the spatial domain, an inverse Fourier Transform is used such that

$$h_{filt}(x, y) = F^{-1}[H_{filt}(u, v)]. \tag{A.5}$$

Figure A.1 displays an example of this process using a Fast-Fourier-Transform to switch from the spatial domain to the frequency domain. The unfiltered data, shown in Figure A.1(a), is a surface measurement of a substrate containing high-amplitude, low spatial frequency curvature terms as well as lower amplitude mid-spatial frequency terms. The power spectra, obtained by applying the FFT, is shown in Figure A.1(b) where the dominant central peak corresponds to the low spatial frequency terms. To eliminate this peak from the spectra, a high-pass Gaussian filter, displayed in Figure A.1(c), is defined and multiplied with the spectra. Finally, by performing an inverse FFT the mid-spatial frequency features are revealed, as shown in Figure A.1(d).

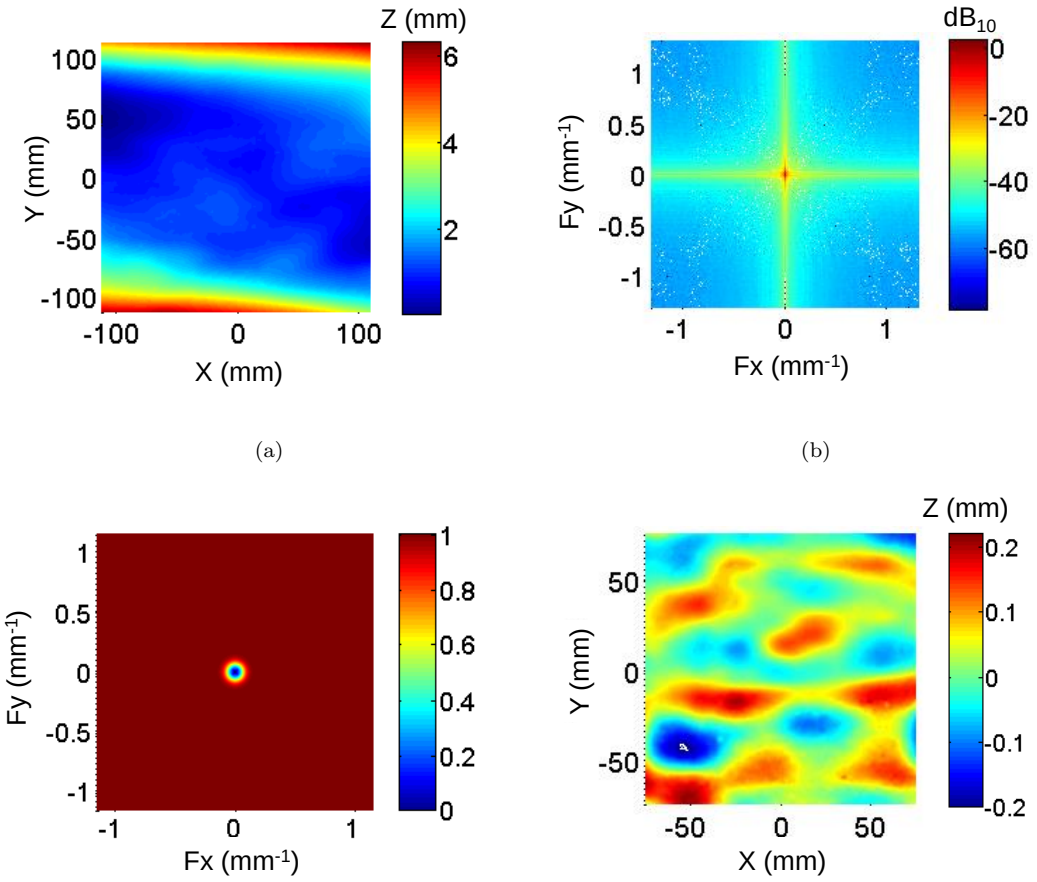

Figure A.1: a) Unfiltered surface measurement displaying dominating low-spatial frequency curvature terms. b) Power spectral density (PSD) of surface shape after implementation of FFT. c) High-pass Gaussian spatial filter. d) Filtered surface measurement after implementation of high-pass filter and iFFT revealing mid-spatial frequency features.

Appendix B

ABD Matrices of Considered Laminate Orientations

Laminate 1: 8-ply $[0°/+45°/\text{-}45°/90°]_s$

$$ABD_1 = \begin{bmatrix} 31838 & 10277 & 0 & 0 & 0 & 0 \\ 10277 & 31838 & 0 & 0 & 0 & 0 \\ 0 & 0 & 10780 & 0 & 0 & 0 \\ 0 & 0 & 0 & 270 & 41 & 18 \\ 0 & 0 & 0 & 41 & 53 & 18 \\ 0 & 0 & 0 & 18 & 18 & 43 \end{bmatrix}. \tag{B.1}$$

Laminate 2a: 16-ply $[0°/+45°/\text{-}45°/90°]_{2s}$

$$ABD_{2a} = \begin{bmatrix} 63675 & 20555 & 0 & 0 & 0 & 0 \\ 20555 & 63675 & 0 & 0 & 0 & 0 \\ 0 & 0 & 21560 & 0 & 0 & 0 \\ 0 & 0 & 0 & 1457 & 377 & 36 \\ 0 & 0 & 0 & 377 & 1023 & 36 \\ 0 & 0 & 0 & 36 & 36 & 396 \end{bmatrix}. \tag{B.2}$$

Laminate 2b: 16-ply $[0°/+45°/\text{-}45°/90°]_s$ + $[90°/\text{-}45°/+45°/0°]_s$

$$ABD_{2b} = \begin{bmatrix} 63675 & 20555 & 0 & 0 & 0 & 0 \\ 20555 & 63675 & 0 & 0 & 0 & 0 \\ 0 & 0 & 21560 & 0 & 0 & 0 \\ 0 & 0 & 0 & 1242 & 377 & 0 \\ 0 & 0 & 0 & 377 & 1242 & 0 \\ 0 & 0 & 0 & 0 & 0 & 396 \end{bmatrix}. \tag{B.3}$$

Laminate 3a: 32-ply $[0°/+45°/\text{-}45°/90°]_{4s}$

$$ABD_{3a} = \begin{bmatrix} 127350 & 41110 & 0 & 0 & 0 & 0 \\ 41110 & 127350 & 0 & 0 & 0 & 0 \\ 0 & 0 & 43120 & 0 & 0 & 0 \\ 0 & 0 & 0 & 10250 & 3122 & 72 \\ 0 & 0 & 0 & 3122 & 9382 & 72 \\ 0 & 0 & 0 & 72 & 72 & 3277 \end{bmatrix}. \tag{B.4}$$

Laminate 3b: 32-ply $\left[[0°/+45°/\text{-}45°/90°]_s + [90°/\text{-}45°/+45°/0°]_s\right]_2$

$$ABD_{3b} = \begin{bmatrix} 127350 & 41110 & 0 & 0 & 0 & 0 \\ 41110 & 127350 & 0 & 0 & 0 & 0 \\ 0 & 0 & 43120 & 0 & 0 & 0 \\ 0 & 0 & 0 & 9816 & 3122 & 0 \\ 0 & 0 & 0 & 3122 & 9816 & 0 \\ 0 & 0 & 0 & 0 & 0 & 3277 \end{bmatrix}. \tag{B.5}$$

Appendix C

Active Layer Bonding Convergence Study

As it was necessary to capture very fine features in the analysis of active layer bonding, a convergence study was performed in order to determine the proper mesh size at the discontinuities between each active plate. The study was performed for the lowest gap size considered, 0.25 mm. The element width of the CFRP substrate and PZT plates were refined at the same levels. Figure C.1 displays the results of this study for element sizes of 200, 100 and 50 μm, respectively. Convergence in the peak-to-valley magnitude as well as width of deformation is observed at element sizes of 100 μm with only slight deviations between the results implementing 50 μm elements. Therefore, 100 μm elements were used at the gap locations for the remainder of this study.

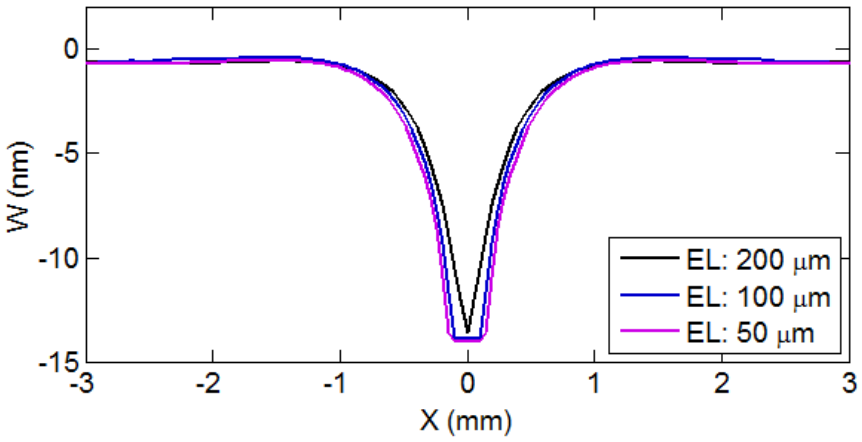

Figure C.1: Results of convergence study for PZT bonding process.

Bibliography

[1] M. Postman, T. Brown, K. Sembach, M. Giavalisco, W. Traub, K. Stapelfeldt, D. Calzetti, W. Oegerle, R. M. Rich, H. P. Stahl, *et al.*, "Advanced technology large-aperture space telescope: science drivers and technology developments," *Optical Engineering*, vol. 51, no. 1, pp. 011007–1, 2012.

[2] H. P. Stahl, "Design study of 8 meter monolithic mirror uv/optical space telescope," in *SPIE Astronomical Telescopes+ Instrumentation*, pp. 701022–701022, International Society for Optics and Photonics, 2008.

[3] J. P. Gardner, J. C. Mather, M. Clampin, R. Doyon, M. A. Greenhouse, H. B. Hammel, J. B. Hutchings, P. Jakobsen, S. J. Lilly, K. S. Long, *et al.*, "The james webb space telescope," *Space Science Reviews*, vol. 123, no. 4, pp. 485–606, 2006.

[4] K. Patterson and S. Pellegrino, "Ultralightweight deformable mirrors," *Applied optics*, vol. 52, no. 22, pp. 5327–5341, 2013.

[5] K. Patterson, S. Pellegrino, and J. Breckinridge, "Shape correction of thin mirrors in a recongurable modular space telescope," in *SPIE Astronomical Telescopes+ Instrumentation*, pp. 773121–773121, International Society for Optics and Photonics, 2010.

[6] "Composite mirror applications." http://www.compositemirrors.com/, 2015.

[7] J. Massarello, B. deBlonk, and A. Maji, "Rapid fabrication of mirrors with nanolaminate facesheets and composite structures," in *International Congress and Exposition on Experimental and Applied Mechanics*, Society for Experimental Mechanics, 2004.

[8] P. C. Chen, T. T. Saha, A. M. Smith, and R. Romeo, "Progress in very lightweight optics using graphite fiber composite materials," *Optical Engineering*, vol. 37, no. 2, pp. 666–676, 1998.

[9] P. C. Chen, C. W. Bowers, M. Marzouk, and R. C. Romeo, "Advances in very lightweight composite mirror technology," *Optical Engineering*, vol. 39, no. 9, pp. 2320–2329, 2000.

[10] J. D. Hochhalter, *Replicated mirrors using carbon fiber reinforced polymers.* PhD thesis, University of New Mexico, 2005.

[11] S. Kendrew, P. Doel, D. Brooks, C. Dorn, C. Yates, R. M. Dwan, I. Richardson, and G. Evans, "Development of a carbon fiber composite active mirror: design and testing," *Optical Engineering*, vol. 45, no. 3, pp. 033401–033401, 2006.

[12] J. J. Massarello, J. S. Welsh, J. D. Hochhalter, A. K. Maji, and P. A. Fuierer, "Fiber print-through mitigation technique for composite mirror replication," *Optical Engineering*, vol. 45, no. 12, pp. 123401–123401, 2006.

[13] S. Thompson, D. Brooks, and A. Doel, "A nickel-carbon-fibre composite for large adaptive mirrors: fabrication methods and properties," *Optics express*, vol. 16, no. 2, pp. 1321–1330, 2008.

[14] G. Hickey, T. Barbee, M. Ealey, and D. Redding, "Actuated hybrid mirrors for space telescopes," in *SPIE Astronomical Telescopes+ Instrumentation*, pp. 773120–773120, International Society for Optics and Photonics, 2010.

[15] "Northrup grumman, aoa xinetics.." http://www.northropgrumman.com/BusinessVentures/AOAXinetics, 2014.

[16] "Cilas." http://www.cilas.com/, 2015.

[17] K. D. Patterson, "Lightweight deformable mirrors for future space telescopes." 2014.

[18] C. Underwood and S. Pellegrino, "Autonomous assembly of a reconfigurable space telescope (aarest) for astronomy and earth observation," in *8th IAA Symposium on Small Satellites for Earth Observation, Berlin*, pp. 4–8, 2011.

[19] C. Underwood, S. Pellegrino, V. Lappas, C. Bridges, B. Taylor, S. Chhaniyara, T. Theodorou, P. Shaw, M. Arya, J. Breckinridge, *et al.*, "Autonomous assembly of a reconfiguarble space telescope (aarest)–a cubesat/microsatellite based technology demonstrator," 2013.

[20] M. Born and E. Wolf, *Principles of optics: electromagnetic theory of propagation, interference and diffraction of light*. Cambridge university press, 1999.

[21] J. W. Strutt, "Xxxi. investigations in optics, with special reference to the spectroscope," *The London, Edinburgh, and Dublin Philosophical Magazine and Journal of Science*, vol. 8, no. 49, pp. 261–274, 1879.

[22] H. Davies, "The reflection of electromagnetic waves from a rough surface," *Proceedings of the IEE-Part IV: Institution Monographs*, vol. 101, no. 7, pp. 209–214, 1954.

[23] H. Bennett and J. Porteus, "Relation between surface roughness and specular reflectance at normal incidence," *JOSA*, vol. 51, no. 2, pp. 123–129, 1961.

[24] P. C. Chen and D. Rabin, "Carbon nanotube optical mirrors," *Journal of Astronomical Telescopes, Instruments, and Systems*, vol. 1, no. 1, pp. 014005–014005, 2015.

[25] T. Barbee, "Nanolaminate thin-shell mirror structures," in *Society of Photo-Optical Instrumentation Engineers (SPIE) Conference Series*, vol. 5166, 2003.

[26] G. S. Hickey, S.-S. Lih, and T. W. Barbee Jr, "Development of nanolaminate thin-shell mirrors," in *Astronomical Telescopes and Instrumentation*, pp. 63–76, International Society for Optics and Photonics, 2002.

[27] R. Bastaits, G. Rodrigues, P. Jetteur, P. Hagedorn, and A. Preumont, "Multi-layer adaptive thin shells for future space telescopes," *Smart materials and structures*, vol. 21, no. 6, p. 064004, 2012.

[28] M. Laslandes, S. Pellegrino, J. Steeves, and K. Patterson, "Optimization of electrode configuration in surface-parallel actuated deformable mirrors," in *SPIE Astronomical Telescopes+ Instrumentation*, pp. 914843–914843, International Society for Optics and Photonics, 2014.

[29] S. W. Tsai, S. Sihn, and R. Y. Kim, "Thin ply composites," *JEC-composites*, vol. 18, pp. 31–33, 2005.

[30] "North thin ply technologies." http://www.thinplytechnology.com/, 2014.

[31] S. Sihn, R. Y. Kim, K. Kawabe, and S. W. Tsai, "Experimental studies of thin-ply laminated composites," *Composites Science and Technology*, vol. 67, no. 6, pp. 996–1008, 2007.

[32] R. Amacher, J. Cugnoni, J. Botsis, L. Sorensen, W. Smith, and C. Dransfeld, "Thin ply composites: Experimental characterization and modeling of size-effects," *Composites Science and Technology*, vol. 101, pp. 121–132, 2014.

[33] K. K. Kratmann, M. Sutcliffe, L. Lilleheden, R. Pyrz, and O. T. Thomsen, "A novel image analysis procedure for measuring fibre misalignment in unidirectional fibre composites," *Composites Science and Technology*, vol. 69, no. 2, pp. 228–238, 2009.

[34] S. Yurgartis, "Measurement of small angle fiber misalignments in continuous fiber composites," *Composites Science and Technology*, vol. 30, no. 4, pp. 279–293, 1987.

[35] S. Kyriakides, R. Arseculeratne, E. Perry, and K. Liechti, "On the compressive failure of fiber reinforced composites," *International Journal of Solids and Structures*, vol. 32, no. 6, pp. 689–738, 1995.

[36] R. Knibbs and J. Morris, "The effects of fibre orientation on the physical properties of composites," *Composites*, vol. 5, no. 5, pp. 209–218, 1974.

[37] J. Berthelot, "Effect of fibre misalignment on the elastic properties of oriented discontinuous fibre composites," *Fibre Science and Technology*, vol. 17, no. 1, pp. 25–39, 1982.

[38] J. Jortner, "A model for predicting thermal and elastic constants of wrinkled regions in composite materials," *Effects of Defects in Composite Materials*, pp. 217–236, 1984.

[39] G. Karami and M. Garnich, "Micromechanical study of thermoelastic behavior of composites with periodic fiber waviness," *Composites Part B: Engineering*, vol. 36, no. 3, pp. 241–248, 2005.

[40] Y. Arao, J. Koyanagi, S. Utsunomiya, and H. Kawada, "Time-dependent out-of-plane deformation of ud-cfrp in humid environment," *Composites Science and Technology*, vol. 69, no. 11, pp. 1720–1725, 2009.

[41] M. Hinckley, "Statistical evaluation of the variation in laminated composite properties resulting from ply misalignment," 1990.

[42] Y. Arao, J. Koyanagi, S. Utsunomiya, and H. Kawada, "Effect of ply angle misalignment on out-of-plane deformation of symmetrical cross-ply cfrp laminates: Accuracy of the ply angle alignment," *Composite Structures*, vol. 93, no. 4, pp. 1225–1230, 2011.

[43] T. A. Bogetti and J. W. Gillespie, "Process-induced stress and deformation in thick-section thermoset composite laminates," *Journal of Composite Materials*, vol. 26, no. 5, pp. 626–660, 1992.

[44] V. Antonucci, M. Giordano, K.-T. Hsiao, and S. G. Advani, "A methodology to reduce thermal gradients due to the exothermic reactions in composites processing," *International journal of heat and mass transfer*, vol. 45, no. 8, pp. 1675–1684, 2002.

[45] R. M. Jones, *Mechanics of composite materials*. CRC Press, 1998.

[46] P. V. Hough, "Method and means for recognizing complex patterns," Dec. 18 1962. US Patent 3,069,654.

[47] "Abaqus cae/standard 6.12." Simulia Inc., Providence, RI, 2012.

[48] "Correlated solutions." http://www.correlatedsolutions.com/, 2014.

[49] J. B. Enns and J. K. Gillham, "Time–temperature–transformation (ttt) cure diagram: Modeling the cure behavior of thermosets," *Journal of Applied Polymer Science*, vol. 28, no. 8, pp. 2567–2591, 1983.

[50] G. G. Stoney, "The tension of metallic films deposited by electrolysis," *Proceedings of the Royal Society of London. Series A, Containing Papers of a Mathematical and Physical Character*, vol. 82, no. 553, pp. 172–175, 1909.

[51] E. Ventsel and T. Krauthammer, *Thin plates and shells: theory: analysis, and applications*. CRC press, 2001.

[52] R. H. Wilke, R. L. Johnson-Wilke, V. Cotroneo, W. N. Davis, P. B. Reid, D. A. Schwartz, and S. Trolier-McKinstry, "Sputter deposition of pzt piezoelectric films on thin glass substrates for adjustable x-ray optics," *Applied optics*, vol. 52, no. 14, pp. 3412–3419, 2013.

[53] N. Lee, S. Pellegrino, and Y.-H. Wu, "Design algorithm for the placement of identical segments in a large spherical mirror," *Journal of Astronomical Telescopes, Instruments, and Systems*, vol. 1, no. 2, pp. 024002–024002, 2015.

[54] R. Bastaits, D. Alaluf, M. Horodinca, I. Romanescu, I. Burda, G. Martic, G. Rodrigues, and A. Preumont, "Segmented bimorph mirrors for adaptive optics: segment design and experiment," *Applied optics*, vol. 53, no. 29, pp. 6635–6642, 2014.

[55] A. K. Noor and W. S. Burton, "Assessment of shear deformation theories for multilayered composite plates," *Applied Mechanics Reviews*, vol. 42, no. 1, pp. 1–13, 1989.

[56] N. Phan and J. Reddy, "Analysis of laminated composite plates using a higher-order shear deformation theory," *International Journal for Numerical Methods in Engineering*, vol. 21, no. 12, pp. 2201–2219, 1985.

[57] J. Reddy and C. Liu, "A higher-order shear deformation theory of laminated elastic shells," *International Journal of Engineering Science*, vol. 23, no. 3, pp. 319–330, 1985.

[58] F. Matthews, G. Davies, D. Hitchings, and C. Soutis, *Finite Element Modelling of Composite Materials and Structures*. Woodhead Publishing LTD., 2000.

[59] J. Reddy, *An Introduction to Nonlinear Finite Element Analysis*. Oxford University Press, 2004.

[60] P. LAGACE, J. BREWER, and C. Kassapoglou, "The effect of thickness on interlamina stresses and delamination in straight-edged laminates," *Journal of composites technology & research*, vol. 9, no. 3, pp. 81–87, 1987.

[61] B. Varughese and A. Mukherjee, "A ply drop-off element for analysis of tapered laminated composites," *Composite structures*, vol. 39, no. 1, pp. 123–144, 1997.

[62] S.-C. Her, "Stress analysis of ply drop-off in composite structures," *Composite structures*, vol. 57, no. 1, pp. 235–244, 2002.

[63] I. Daniel, J. Whitney, and R. Pipes, "Experimental mechanics of fiber reinforced composite materials," *Experimental Techniques*, vol. 7, no. 3, pp. 25–25, 1983.

[64] R. Kriz and W. Stinchcomb, "Elastic moduli of transversely isotropic graphite fibers and their composites," *Experimental Mechanics*, vol. 19, no. 2, pp. 41–49, 1979.

[65] H. Tzou and C. Tseng, "Distributed piezoelectric sensor/actuator design for dynamic measurement/control of distributed parameter systems: a piezoelectric finite element approach," *Journal of sound and vibration*, vol. 138, no. 1, pp. 17–34, 1990.

[66] J.-B. Ihn and F.-K. Chang, "Detection and monitoring of hidden fatigue crack growth using a built-in piezoelectric sensor/actuator network: I. diagnostics," *Smart Materials and Structures*, vol. 13, no. 3, p. 609, 2004.

[67] S. C. Bradford, G. S. Agnes, V. M. Bach, and W. K. Wilkie, "An active composite reflector system for correcting thermal deformations," in *Proc. 52nd AIAA/ASME/ASCE/AHS/ASC Structures, Structural Dynamics and Materials Conference, AIAA*, vol. 1826, pp. 1–8, 2011.

[68] I. Chopra and J. Sirohi, *Smart Structures Theory*. Cambridge University Press, 2013.